Exploring the potential of serial magnetron co-sputtering

Von der Fakultät für Mathematik, Informatik und Naturwissenschaften der RWTH Aachen University zur Erlangung des akademischen Grades eines Doktors der Naturwissenschaften genehmigte Dissertation

vorgelegt von
Diplom-Physiker
Rüdiger Matti Schmidt

aus Münster

Berichter: Prof. Dr. Matthias Wuttig

Prof. Dr. Peter Kelly

Tag der mündlichen Prüfung: 14. Oktober 2014

Diese Dissertation ist auf den Internetseiten der Hochschulbibliothek online verfügbar.

Abstract

Functional thin films are commonly implemented in many products of our daily life. They can be transparent and conducting at the same time and show improved mechanical, chemical as well as optical properties. Consequently, they are important constituents of several state-of-the art technologies like touch screens, solar cells and architectural glazing. The broad field of applications necessitates a versatile and scalable production process capable of processing a high number of units within a short time. Among the possibilities for deposition, magnetron sputtering fulfills these demands, offering versatility, scalability and a high process throughput, and has therefore become the method of choice for the large area coating industry.

Carbon and titanium dioxide (TiO_2) are widely utilized in various thin film applications, due to their unique mechanical and optical properties. Carbon based thin films are employed as low-friction and wear-resistant coatings to increase the life time of e.g. cutting tools, whereas TiO_2 is the material of choice in anti-reflective layers of low-emissivity coatings as well as the mainly used active material in self-cleaning surfaces. Doping with different elements allows the improvement of the properties of carbon and TiO_2 and to increase the otherwise very low deposition rates of these materials. However, systematic studies on the influence of dopants on sputter processes and material properties have so far been complicated, as the production of compound targets is inflexible and expensive.

In this work, a custom-made serial co-sputtering setup, capable of controlling the dopant content in situ, has been utilized to investigate the influence of different dopants on the sputter processes and film properties of carbon and TiO₂, with respect to deposition rate, refractive index and phase formation.

To overcome the low sputter yield of carbon, sputter yield amplification by doping with heavy elements can be employed. In this work, carbon has been doped by two heavier elements to increase the deposition rate. Both elements result in a tremendous rate increase.

The results are compared to computer simulations, which are in an excellent agreement to the experimental data.

Describing the underlying processes upon sputter yield amplification in reactive sputtering is more complex. In this work, TiO_2 has been doped with several heavy elements to increase the deposition rate. The findings presented reveal that thermodynamics play a major role in determining the strength of the rate enhancement, a result not considered by established models so far. Utilizing HiPIMS, the sputter yield amplification effect can be further enhanced. Experiments, which link the additional enhancement to the ionization of the dopant, are presented. Additionally, the influence of heavy dopants on the refractive index is analyzed, revealing a clear concept for high rate, high index TiO_2 thin films.

Moreover, various dopants have been analyzed with respect to their capability to modify the crystallization behavior of TiO_2 . The results show that the phase transformation of amorphous TiO_2 can be controlled by use of the right elements. The transformation behavior is linked to the valence and ionic radius of the dopant as well as to the incorporation of argon in the growing film. The results presented allow for a deposition of thermally stable amorphous TiO_2 thin films as well as films which crystallize into either anatase or rutile.

Finally, a novel sputter technique, using a carbon print target sputtered in reactive atmosphere to deposit multi-component thin films with high stoichiometry precision, is presented.

This work exploits the potential of serial magnetron co-sputtering to tailor the process conditions and film properties of carbon and TiO_2 . The results presented add to the understanding of the sputter yield amplification effect and the crystallization and transformation behavior of doped TiO_2 thin films, allowing for a tailoring of their properties with respect to the desired field of application. The results presented can be readily used for deposition of doped TiO_2 and carbon based thin films in industrial applications.

Kurzfassung

Übersetzung des englischen Originaltitels:

Erforschung des Potenzials seriellen Magnetron-Co-Sputterns

Funktionelle Dünnschichten sind ein wichtiger Bestandteil vieler moderner Technologien aus unserem täglichen Leben. Sie bestechen durch die Verknüpfung von Transparenz und gleichzeitiger elektrischer Leitfähigkeit und haben besondere mechanische, chemische oder optische Eigenschaften. Durch ihren Einsatz werden z.B. Flachbildschirme, Solarzellen und funktionelle Architekturverglasung erst ermöglicht. Die vielseitige Einsetzbarkeit stellt hohe Anforderungen an den Herstellungsprozess, welcher skalierbar sein muss und gleichzeitig eine hohe Durchsatzmenge ermöglichen sollte. Von den verschiedenen verfügbaren Depositionsprozessen hat sich das Magnetronsputtern in der Großflächenbeschichtung durchgesetzt, da es diese Anforderungen in allen Punkten erfüllt.

Kohlenstoff und Titandioxid (TiO₂) sind zwei Materialien, welche auf Grund ihrer besonderen mechanischen und optischen Eigenschaften in einer Vielzahl von Anwendungen Verwendung finden. Kohlenstoffbasierte Dünnschichten werden als verschleißmindernde und reibungsarme Beschichtungen verwendet, welche unter anderem die Haltbarkeit von Werkzeugen verbessern, wohingegen TiO₂ als Antireflexschicht in Wärmedämmgläsern und als aktives Material in selbstreinigenden Oberflächen verwendet wird. Die herausragenden Eigenschaften dieser beiden Materialien können durch Dotierung weiter verbessert werden. Zudem kann durch Dotierung die sonst sehr geringe Depositionsrate gesteigert werden. Die systematische Untersuchung des Einflusses von Dotanden auf Prozess- und Materialeigenschaften war bisher jedoch nur eingeschränkt möglich, da die Herstellung von Sputtertargets mit fester Dotierungskonzentration aufwendig und kostenintensiv ist.

Im Rahmen dieser Arbeit ist ein maßgefertigtes Co-Sputtersystem verwendet worden, welches in der Lage ist, die Dotierungskonzentration des Targets in situ einzustellen. Es wird gezeigt, wie sich Dotanden auf die Prozess- und Filmeigenschaften von Kohlenstoff und TiO₂

in Sputterprozessen auswirken, wobei der Fokus der Untersuchung auf der Depositionsrate, dem Brechungsindex und der Phasenbildung liegt.

Die niedrige Depositionsrate von Kohlenstoff kann durch Dotierung mit schweren Atomen, mit Hilfe der sogenannten Sputterratenverstärkung (sputter yield amplification), gesteigert werden. Im Rahmen dieser Arbeit ist Kohlenstoff mit zwei schwereren Elementen dotiert worden, welche beide eine deutliche Verstärkung der Sputterrate, im Einklang mit Computersimulationen, zeigen.

Die Physik der Ratenverstärkung bei reaktivem Sputtern ist deutlich komplexer. Im Rahmen dieser Arbeit ist TiO₂ mit verschiedenen Elementen dotiert worden um den Einfluss auf die Depositionsrate zu untersuchen. Eine thermodynamische Betrachtung erlaubt die Erklärung der Ergebnisse, welche mit bisherigen Modellen nicht zu interpretieren sind. Unter Zuhilfenahme eines HiPIMS-Prozesses kann die Ratenverstärkung weiter gesteigert werden, was auf die Ionisation der Dotierungsatome zurückgeführt werden kann. Desweiteren wird gezeigt, dass der Brechungsindex sowohl durch Dotierung als auch durch geeignete Prozessparameter kontrolliert werden kann, wodurch ein klares Konzept zur industriellen Herstellung hochbrechender Schichten bei gleichzeitig hoher Depositionsrate zur Verfügung gestellt wird.

Neben der Ratenverstärkung können Dotanden auch dazu eingesetzt werden die Kristallisationseigenschaften von ${\rm TiO_2}$ zu beeinflussen. Im Rahmen dieser Arbeit wird gezeigt, dass die Kristallisation mit der Valenz und dem Ionenradius des Dotanden, als auch mit dem Einbau von Argon in die aufwachsende Schicht verknüpft ist. Die präsentierten Ergebnisse ermöglichen, bei geeigneter Wahl des Dotanden, die Kristallisationseigenschaften von ${\rm TiO_2}$ individuell auf die Anwendung anzupassen.

Abschließend wird ein neues Sputterkonzept, basierend auf einem Kohlenstofftarget, welches in reaktiver Atmosphäre gesputtert wird, vorgestellt. Dieses Konzept ermöglicht die Herstellung komplexer Oxide mit sehr guter Stöchiometriekontrolle.

Die vorliegende Arbeit nutzt das Potenzial seriellen Magnetron-Co-Sputterns um die Prozess- und Filmeigenschaften von Kohlenstoff und ${\rm TiO_2}$ zu verbessern. Die präsentierten Resultate ermöglichen ein tiefgehendes Verständnis der Ratenverstärkung und der Kristallisationseigenschaften von ${\rm TiO_2}$ und können dazu genutzt werden industrielle Dünnschichtanwendungen zu verbessern.

Contents

l	Ba	ckground	1
1	Intro	oduction	3
	1.1	Structure of this work	4
2	Mat	erials	7
	2.1	Carbon	7
		2.1.1 Carbon based thin films	8
	2.2	Titanium dioxide (TiO2)	9
		2.2.1 TiO_2 thin films	11
		2.2.2 The anatase to rutile phase transformation (ART)	12
3	Thir	n film deposition	17
	3.1	Multi-component thin films	17
		3.1.1 COSMOS	19
	3.2	The upgraded Berg-Model	20
		3.2.1 Poisoning mechanisms	21
		3.2.2 Preferential sputtering	21
		3.2.3 Equilibrium	22
		3.2.4 Deposition	23
	3.3	Sputter yield amplification	24
	3.4	High power impulse magnetron sputtering (HiPIMS)	25
4	Ana	lytical equipment	27
	4.1	X-ray analysis	27
		4.1.1 X-ray reflectivity (XRR)	28
		4.1.2 X-ray diffraction (XRD)	29

Contents

	4.2	Optical analysis	30
		4.2.1 Ellipsometry	
		4.2.2 Ultraviolet-visible spectroscopy (UV-VIS spectroscopy)	31
		4.2.3 Modeling	31
	4.3	Composition	32
		4.3.1 Rutherford Backscattering Spectrometry (RBS)	34
		4.3.2 Energy-dispersive X-ray spectroscopy (EDX)	36
		4.3.3 X-ray photoelectron spectroscopy (XPS)	36
	4.4	Optical emission spectroscopy (OES)	37
	4.5	Annealing	40
П	Re	esults	43
5	Spu	utter yield amplification of carbon	45
	5.1	Deposition rates	45
	5.2	Composition	47
	5.3	Simulation	49
	5.4	Comparing experiment and simulation	49
6	Spu	utter yield amplification of TiO ₂	53
	6.1	Quantification	54
	6.2	Dopant comparison	
		6.2.1 Target hysteresis	
		Refractive index evolution upon doping	
	6.4	Sputter yield amplification using HiPIMS	
		6.4.1 Implantation efficiency	70
7	Influ	uence of dopants on structure and phase transformation of TiO ₂	75
	7.1	Dopants	75
	7.2	Structural properties of as-deposited samples	77
	7.3	Phase transformation upon annealing	81
		7.3.1 Anatase to rutile transformation-inhibiting dopants	81
		7.3.2 Anatase to rutile transformation-promoting dopants	89
8	Car	bon print target	99
	8.1	Concept	
	8.2	Sputtering carbon in reactive atmosphere	101
	8.3	TiO ₂ via carbon print target	102

III Conclusion & Outlook	105
Conclusion	107
Outlook	109
IV Appendix	I
A List of acronyms and abbreviations	III
B Dopant deposition rates	VI
C Optical emission lines	IX
Bibliography	X
List of Figures	XXX
List of Tables	XXXIII
Acknowledgements	XXXV
Curriculum Vitae	XXXVI

Part I Background

Chapter 1

Introduction

The world we live in gets more and more dominated by smart technologies. We use smart-phones, watch movies on smart TVs and expect even our windows in the living room to act smart by blocking UV light or changing transparency and color. Functional thin films play a major role in the development of smart technologies, altering and improving the properties of several products. They can be transparent and conducting at the same time [Gra93] and show improved mechanical [VVv+99] as well as optical properties [TPS+94]. Furthermore they can be utilized to produce self-cleaning surfaces [PH97]. The field of products they are employed in is wide-ranging from smartphones and flat-screen monitors over car windshields and solar cells to architectural glazing.

The mentioned fields of applications necessitate a versatile and scalable production process as the size of the products varies strongly. Additionally, a high number of units has to be processed within a short time to satisfy the growing demand of modern technologies. One process which fulfills these demands, offering versatility, scalability and a high process throughput, is sputter deposition which is therefore favored by the large area coating industry [KA00, BSVB10].

Two materials which are commonly implemented as functional thin films are carbon and titanium dioxide (TiO_2). These materials are of great interest to researchers and industry due to their unique properties, giving rise to various applications. Often, these films are doped by different elements to alter and improve their properties [Don98, FHY+05], but systematic studies on the influence of dopants on sputter processes and material properties have so far been complicated, as the production of compound targets is inflexible and expensive. Serial co-sputtering offers an unrivaled flexibility and control of the dopant content, separated

atmospheres for all targets as well as a homogeneous deposition [Bel93, CBBK93, SPSU10]. Consequently, serial co-sputtering has been utilized in this work to investigate the influence of different dopants on the sputter processes and film properties of carbon and TiO₂, systematically.

Carbon and TiO_2 both suffer from a comparatively low deposition rate when deposited by magnetron sputtering [BE07]. To overcome this disadvantage, sputter yield amplification can enhance the deposition rate by heavy element doping as has been shown by Austgen et al. for Al_2O_3 and TiO_2 experimentally [AKZ⁺11] and by use of TRIDYN simulations for Al_2O_3 by Kubart et al. [KSA⁺12]. In this work, their observations and conclusions are extended by additional dopants and experiments, which give a detailed understanding of the underlying physics, revealing the best dopant for industrial depositions.

The production of many products requires high temperatures during the fabrication process. In the production process of security glasses for example, the glass needs to be annealed to enhance the mechanical properties [SL13]. Functional TiO_2 thin films need to be deposited on such kind of glasses after the annealing process to avoid cracks due to phase transformations, which give the glass a milky appearance. The crystallization behavior of TiO_2 can be altered by doping [HS11] and hence more stable materials can be produced. However, investigations of the phase transformation of TiO_2 have mainly been performed using powders [SP65, GM01, HS11, Mac75] and their validity for thin films is unknown. In this work, the influence of dopants on the phase formation and transformation of TiO_2 thin films is therefore investigated by use of serial co-sputtering. The results presented add to the understanding of the crystallization and transformation behavior of doped TiO_2 thin films allowing for a tailoring of their properties with respect to the field of application.

1.1 Structure of this work

In the first part of this work, an overview about the materials investigated, sputter technology and the utilized analytical equipment is given. The second part outlines the experiments performed as well as the corresponding results and discussions followed by the third part containing a final conclusion.

In the first chapter of Part I: Background, the two materials investigated, namely carbon and titanium dioxide (TiO_2), are described, giving an overview of their properties and use in industrial, especially thin film applications. In the second chapter, different concepts and techniques for sputtering multi-component thin films as well as a theoretical model describing the sputtering process are summarized. The analytical tools utilized within this work as well as their functional principles are subject of the last chapter of this part.

Part II: Results contains all experiments performed. In the first chapter, sputter yield amplification of carbon upon doping with heavy elements is investigated and the results are compared to computer simulations, whereas the second chapter deals with the sputter yield amplification of TiO₂. Different dopants and discharges are compared and their influence on the refractive index is analyzed. The third chapter focuses on doping of TiO₂ with respect to structure formation and structure transformation upon annealing. A novel sputter technique, using a carbon print target to deposit multi-component thin films with high stoichiometry precision is introduced in the last chapter of this part.

A summary of the results part as well as an outlook is given in Part III: Conclusion & Outlook

Materials

Carbon and titanium dioxide (TiO_2) are two materials with very unique properties which make them scientifically fascinating and essential for various industrial applications. In many cases they are deposited by magnetron sputtering due to its well-known benefits of versatility and up-scaling [KA00, BSVB10]. In this work, they have been doped with different elements to increase their sputter rate and in case of TiO_2 to influence its crystallization behavior, too. This chapter gives an overview of the properties and applications of these two materials.

2.1 Carbon

Carbon is the sixth element in the periodic table with the element symbol C. It is the fourth most abundant element in the Milky Way [Cro95] and the chemical basis of organic life, being the second most abundant element in the human body [Fri72]. Carbon is one of the most important constituent elements of modern chemicals, drugs and life-style products.

Pure carbon can be stabilized in various molecular configurations called allotropes, from which diamond, graphite, amorphous carbon and the recently discovered graphene [Nov04] are the best known. Besides, carbon can exist as fullerenes, which are carbon nanomaterials in the form of cylinders, spheres and many other shapes. These different molecular configurations are possible due to different hybridizations of the carbon $2s^2p^2$ -orbitals [IL09] leading to significantly differing properties of the allotropes. Diamond for example is transparent, nearly isolating and the hardest material occurring in nature, whereas graphite shows a dark gray color, a high conductivity and is one of the softest materials known.

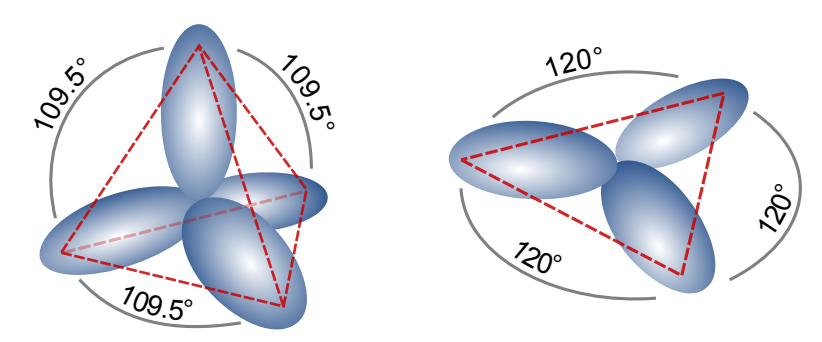


Figure 2.1 | Schematic sketch of the sp^3 - and sp^2 -hybridization of carbon. Upon hybridization the $2s^2p^2$ -orbitals of carbon form four sp^3 -orbitals (left) or three sp^2 -orbitals with the same energy (right). Modified with permission [Wik06].

Diamond consists of sp³-hybridized carbon atoms, each tetrahedrally bound to four neighbors, resulting in binding angles of 109.5° between the bonds [IL09] as can be seen in Fig. 2.1. The strong bonds and the tetrahedral structure are the origin of the high density (3.51 g/cm³) and outstanding hardness of diamond [Ant95]. Nevertheless, diamond is only a meta stable phase of carbon, built under high pressure, which irreversibly transforms to graphite at high temperatures [BBW+96]. Graphite on the other hand is the stable phase of carbon with a density of 2.09 g/cm³ to 2.23 g/cm³ [Ant95]. It is built up in two dimensional planes of sp²-hybridized carbon atoms in a hexagonal crystal structure, resulting in binding angles of 120° (see Fig. 2.1). The bonds within the planes are stronger than those of diamond, but in between the planes only van der Waals forces occur, which give graphite its cleaving properties - each plane can easily slip past one other [IL09]. If pentagons or heptagons are incorporated into a graphite structure the planes will bend building spheres and tubes, called fullerenes, named after Richard Buckminister Fuller [DDE96]. Most famous fullerenes are C₆₀ balls, called buckyballs, and carbon nanotubes [Aja99]. Without a crystalline structure, carbon exists in its amorphous phase, which transforms to graphite at normal pressure. A recently discovered allotrope of carbon is graphene, which is basically a single-layer sample of graphite. Graphene shows very unique properties like high stability, great conductivity, etc. [ATK10].

2.1.1 Carbon based thin films

The expression carbon based thin films describes a set of very thin layers of carbon rich materials, which are widely used in numerous industrial applications. Carbon is used in many hard coatings like diamond-like carbon (DLC) [Rob91], carbon nitride, transition metal carbides and boron carbide. These materials are mechanically very stable and resistant to scratching and are traditionally used as low-friction and wear-resistant coatings [EASL11,

ED06] to increase the life time of e.g. cutting tools [VVv⁺99]. Those films are often doped by different elements to improve their properties, e.g. their tribological behavior [Don98]. Additionally, it has recently been reported that highly ionized plasma processes are capable of producing high amounts of sp³-hybridization in carbon coatings [ASL⁺12, SBZ⁺12] improving the mechanical properties further. Not only their mechanical, but also their electrical properties are remarkable, as they offer the possibility to replace silver as an electrode material in electrical contacts [NTL⁺11, JLR⁺11] with the advantage of chemical inertness and wear resistance.

Sputter deposition techniques are often utilized for the deposition of carbon based thin films due to their well-known benefits of versatility and up-scaling [KA00, BSVB10]. Sputtering of carbon is, however, hampered by a very low deposition rate due to the low sputter yield of carbon [BE07], which is addressed in Chap. 5 by heavy element doping using the so called sputter yield amplification effect [BBG+92, SRP+14].

2.2 Titanium dioxide (TiO₂)

Titanium dioxide (TiO₂), also known as titania, is the most stable oxide of titanium. It is a semiconductor, transparent in the visible range, non-toxic and shows a bright white color in powder form due to its high refractive index, which results in high reflectivity from the surfaces [HS11]. Due to these properties, TiO₂ is heavily used in our daily life, being an important constituent in nearly all white colors, toothpaste and even food [FE00]. Additionally, TiO₂ shows a pronounced photocatalytic activity, which enables the presence of radicals at the TiO₂ surface due to reaction of adsorped molecules (e.g. O₂ or H₂O) with photo-generated charge carriers [LLY95]. This photocatalytic effect allows TiO₂ to be used in several applications like air and water purification [MD01, Mat87, PBC97], self-cleaning and self-sterilizing coatings [PH97, MHL05, MWC06, CTP⁺07] and the electrolysis of water to generate hydrogen [FH72, Wol93].

TiO₂ mainly occurs in three different phases, namely anatase, rutile and brookite [LRS12], from which anatase and brookite are metastable and rutile is stable. Additionally, TiO₂ can exist in five high pressure phases [Pis76, Ren00, DDA⁺01, MSH02]. However, these high pressure phases as well as brookite are only of minor interest for research and applications [LLY95]. Consequently, only anatase and rutile are discussed here.

The anatase and rutile crystal structures consist of Ti^{4+} ions, each coordinated to six O^{2-} ions, configured in octahedral chains. In both phases the TiO_6 octahedra are slightly distorted, two Ti–O bonds are slightly larger than the other four, with anatase having the greater distortion [MC95]. The reason for the distortion is the so called Jahn-Teller effect which occurs for

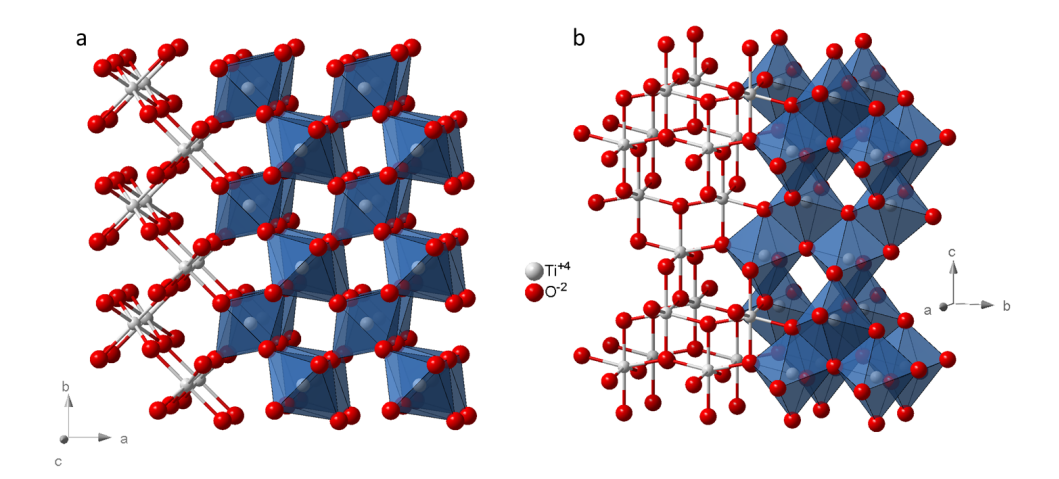


Figure 2.2 | **Crystal structure of rutile and anatase TiO₂.** The anatase and rutile crystal structure consist of Ti^{4+} ions, each coordinated to six O^{2-} ions, configured in octahedral chains. In both phases the TiO_6 octahedra are slightly distorted, two Ti-O bonds are slightly larger than the other four. In the rutile structure (a), space group $P4_2/mnm$, the TiO_6 octahedra are tilted by 90° between different chains, with two edges being shared. In the anatase structure (b), space group $I4_1/amd$, all TiO_6 octahedra are orientated in the same direction with four edges being shared [Ant95]. Both schematics were made using the database of the Diamond 3.2 software [BBB96].

crystals consisting of transition metal compounds, having partially filled d-shells. It states that orbital degenerated non-linear molecules are not stable [JT37]. In a non-distorted TiO₂ crystal the binding electron states would be degenerated due to the symmetrical configuration of the lattice. Hence, according to Jahn and Teller, this leads to a geometrical distortion, lowering the symmetry and by that removing the degeneracy, which results in a lowering of the total energy. As a consequence, the conduction band of TiO₂ splits into four σ -bonded e_g -like and six π -bonded t_{2g} -like subbands [MNK+00, FFL+07], while the top of the filled valence band is constituted by oxygen 2p orbitals [GSC00].

In anatase, space group I4₁/amd, four edges of the TiO₆ octahedra are shared, whereas rutile, space group P4₂/mnm, shares only two edges [Ant95]. In anatase all TiO₆ octahedra are orientated in the same direction, whereas in rutile the TiO₆ octahedra are tilted by 90° between different chains, as can be seen in Fig. 2.2. Due to this tilt, the rutile structure has a shorter c-axis and a by about 8 % smaller volume, leading to an increased density [SP65] of 4.250 g/cm³ compared to 3.894 g/cm³ of anatase [LLY95], which also results in a higher refractive index of n_0 = 2.61 and n_e = 2.90 for rutile compared to n_0 = 2.49 and n_e = 2.56 for anatase [Lid97], where n_0 and n_e denote the refractive indexes for the ordinary and extraordinary ray, respectively.

Both crystal structures, anatase and rutile, are n-type semiconductors. The Fermi energy

Table 2.1 | Overview of the main properties of anatase and rutile TiO₂.

Property	Anatase	Rutile	Reference
Semiconductor	n-type	n-type	[TPS ⁺ 94]
Crystal structure	Tetragonal	Tetragonal	[FE00]
Atoms per unit cell	12	6	[MC95]
Molecules per unit cell	4	2	[MC95]
Space group	I4 ₁ /amd	P4 ₂ /mnm	[Ant95]
a-axis (Å)	3.785	4.594	[BHM ⁺ 87]
c-axis (Å)	9.514	2.959	[BHM ⁺ 87]
Lattice plane distance (Å)	3.52	3.25	[Ant95]
Band gap (eV)	3.3	3.1	[LLY95]
Density (g/cm³)	3.894	4.250	[LLY95]
Refractive index ($\lambda = 589 \text{nm}$)	2.49-2.56	2.61-2.90	[Lid97]
Hardness (Mohs)	5.5-6	6-6.5	[Ant95]
Bulk modulus (GPa)	183	206	[WL06]
Surface energy (J/m²)	1.34	1.93	[ZB98]
Heat of formation (kJ/mol)	938.7	944.0	[Cha98, CWM84]

 $E_{\rm F}$ is located near the bottom edge of the conduction band [HDZ76] shifted due to oxygen vacancies and titanium interstitials [CHA⁺06]. These defects play a major role in photocatalytic effects as well as for the transformation from anatase to rutile. A discussion of the formation energies of these defects has been performed by Na-Phattalung et al. [NPSK⁺06]. The Fermi level in anatase is about 0.1 eV higher than in rutile [Wol93] suggesting a higher defect density. However, Zywitzki et al. reported a significantly higher defect density in the rutile phase [ZMS⁺04]. In contrast, the situation at the surface is reversed. Here, anatase is reported to have 7% oxygen vacancies, whereas rutile has only 4% [TFM⁺07], which is in line with the higher photocatalytic activity of anatase reported in literature [HMCB95].

An overview about the main properties of anatase and rutile is given in Tab. 2.1. A detailed discussion of these properties as well as a more detailed discussion of the electric and photocatalytic properties can be found in the literature [LLY95, HS11, Yat11].

2.2.1 TiO₂ thin films

Due to its high refractive index and its photocatalytic activity TiO_2 has become the material of choice in anti-reflective layers of low-emissivity coatings as well as the mainly used active material in self-cleaning surfaces. These coatings can be deposited using various deposition techniques including evaporation [MBE⁺00], chemical vapor deposition (CVD) [BGPM94],

sol-gel processes [Ahn03], ion beam assisted deposition [LZZ⁺00] and sputter deposition [ZT02, MHŠ06]. Of these techniques, the latter is favored by the architectural glass industry due to its well-known benefits of versatility and up-scaling [KA00, AKW10, BSVB10].

As the rutile phase exhibits a higher refractive index and the anatase phase shows a greater photocatalytic activity, the structure control upon deposition is crucial to ensure the desired properties for the respective application [AKW10]. Additionally, doping of TiO₂ can extend the usability for applications even further. TiO₂:Nb and TiO₂:Ta have been reported to be transparent conductive oxides (TCO) [FHY+05, HFU+05, GvD+07, HYH+08, YHK+09] and doping of TiO₂ can increase the photocatalytic activity. For example, Farahani et al. showed that the photocatalytic activity of TiO₂:W is extended to the visible range [FKW+11].

In industrial applications TiO₂ thin films are mostly sputtered using DC discharges [LHM94]. Depending on the deposition parameters, these films are X-ray amorphous (they do not show any distinct peaks in X-ray diffraction measurements, see Sect. 4.1.2), anatase, a mixture of amorphous/antase or a mixture of anatase/rutile. Pure rutile films, which are thermally stable, can not be sputtered using DC sputter processes [AKW10]. This can only be achieved using highly ionized plasma deposition processes [ASMW06, SQW⁺08], in which the energy transferred into the growing film is much higher (see Sect. 3.4).

Reactive sputtering of TiO_2 is, however, hampered by a very low deposition rate, which is addressed in Chap. 6 by heavy element doping using the so called sputter yield amplification effect [BBG⁺92].

2.2.2 The anatase to rutile phase transformation (ART)

The anatase phase is metastable and transforms irreversibly into rutile. Nevertheless, TiO_2 crystallizes into anatase first as anatase has the lower surface energy of $1.34\,J/m^2$ compared to rutile with a surface energy of $1.93\,J/m^2$. Thermodynamic studies of Zhang et al. suggest that anatase is more stable than rutile below a critical nucleus size of $14\,nm$ [ZB98], which is another explanation why the anatase structure crystallizes first. However, experimental studies show stable rutile nanoparticles of sizes below this value [PCKK99]. At room temperature the transformation from anatase to rutile is too slow to be noticed and practically does not proceed [CHR04]. Depending on raw material, dopants, method of synthesis and crystal size anatase begins to transform to rutile at measurable speeds in air at temperatures ranging from $400\,^{\circ}\text{C}$ to $1200\,^{\circ}\text{C}$ [SP65, GM01, HNO+03, LLBGW05].

The fabrication of many products requires high temperatures during the production process, whereas other devices exhibit high temperatures during usage, for example gas sensors [RLS $^+$ 03]. If a phase transformation of TiO₂ occurs during the production process or

during usage, this will alter the properties or may even destroy the device. In the production process of security glasses for example, the glass needs to be annealed to about $630\,^{\circ}$ C to enhance the mechanical properties [SL13]. If a security glass is planned to be improved by a functional layer containing TiO_2 , the deposition of this layer needs to be performed after the annealing process to avoid a phase transformation of TiO_2 . Otherwise, the annealing would result in cracks, which give the glass a milky appearance and make it unusable. Hence, understanding and tailoring the crystallization of TiO_2 is of great interest for several applications.

The crystallization behavior of TiO_2 can be altered by doping [HS11] and hence more stable materials can be produced. Nevertheless, adding a dopant will also change the properties of the resulting compound. This includes changes of the band gap and consequently the refractive index [Ser06]. These changes have to be kept in mind when altering the crystallization behavior by use of dopants with respect to the desired application.

Due to their industrial relevance, the phase transformation of anatase to rutile has been mainly studied for powders [SP65, GM01, HS11, Mac75]. Hanaor and Sorrell reviewed the anatase to rutile transformation giving an overview about all important mechanisms including cationic dopants, anionic dopants, valance changes and a prediction for non evaluated elements [HS11]. In the following their most important statements, with respect to this work, will be summarized.

Defects in the oxygen sub-lattice (TiO_{2-x}) are one of the two most important factors affecting the phase transformation [RKD07]. The transformation from anatase to rutile involves the breaking and reforming of bonds (reconstructive) [BMD06], therefore oxygen vacancies, which allow an easier rearrangement by lessening the structural rigidity of the oxygen sub-lattice [SP65], promote the transformation. The number of oxygen vacancies can be altered by substituting Ti with dopants of valences different to that of Ti ($n \neq 4$). If a Ti atom in the lattice is substituted by a dopant atom with valence n < 4 this will increase the number of oxygen vacancies and Ti interstitials in the lattice:

$$Ti^{4+}2O^{2-} + X^{n+} \longrightarrow X^{n+} \frac{n}{2}O^{2-} + \left(2 - \frac{n}{2}\right) \Box + \left(1 - \frac{n}{4}\right)O_2 + Ti_{interstitial}^{n+},$$
 (2.1)

where \Box denotes an oxygen vacancy and $\mathrm{Ti}_{\mathrm{interstitial}}$ is a Ti interstitial. On the other hand, if a Ti atom in the lattice is substituted by a dopant atom with valence n > 4 this will, consequently, reduce the number of oxygen vacancies and Ti interstitials.

A dopant will only be able to enter the lattice if its radius is within 15% of that of the host lattice, according to the Hume-Rothery rule [HRC88]. Therefore, the second of the two most important factors altering the phase transformation is the ionic radius of the dopant. The

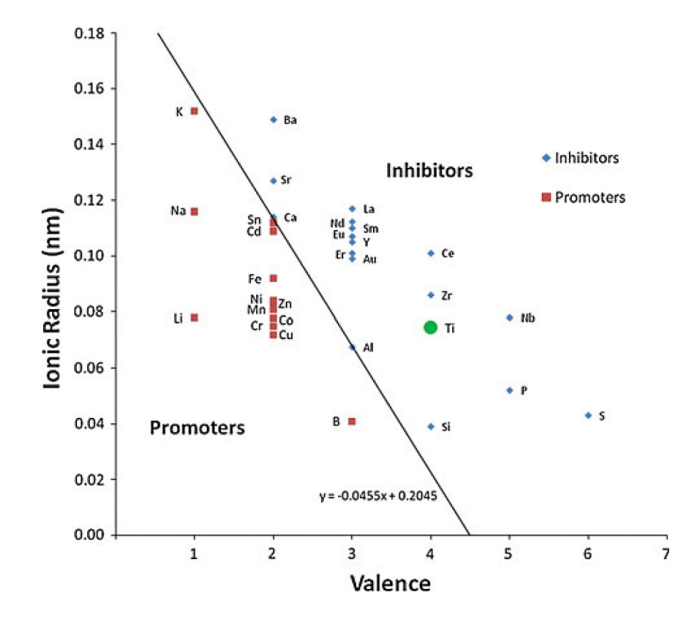


Figure 2.3 | Dopants of TiO₂ plotted as a function of valence and ionic radius. A valence of n < 4 and a small ionic radius is necessary for the promotion of the anatase to rutile transformation. All dopants of valence $n \ge 4$ inhibit the phase transformation as well as dopants with large radii. All dopants can be split into dopants inhibiting and dopants promoting the phase transformation by a boundary line. Taken from [HS11].

larger the dopant radius, the more the ${\rm TiO_2}$ lattice is constrained and phase transformation is suppressed. With this argument Ti interstitials formed upon substitution also constrain the lattice and stabilize it. Hence, the formation of oxygen vacancies and Ti interstitials upon substitution can be considered as competing phenomena.

Hanaor and Sorrell plotted dopants which have been investigated in literature with respect to their inhibiting or promoting effect on the anatase to rutile transformation [HS11] as a function of their Shannon-Prewitt ionic radii in sixfold coordination [Sha76] and most common valences. For Mn, Fe and Co a valence of 2 was assumed as these species are likely to be reduced upon heating [HW72, WYMZ97, GP98]. If contradictory effects have been reported in literature, the most common finding was used. In the resulting graph, which can be seen in Fig. 2.3, the dopants are divided by a boundary line defined by the equation

$$r = (-0.0455n + 0.2045) \text{ nm},$$
 (2.2)

where r is the ionic radius and n is the valence of the dopant, into two areas. In the bottom left area of Fig. 2.3 only promoters of the anatase to rutile transformation are found, whereas in the top right area only inhibitors are found. It can be seen that only dopants with a valence of n < 4 are able to promote the rutile phase, but a small radius is necessary as well so that the lattice is not constrained. As the lattice will also be constrained by Ti interstitials upon

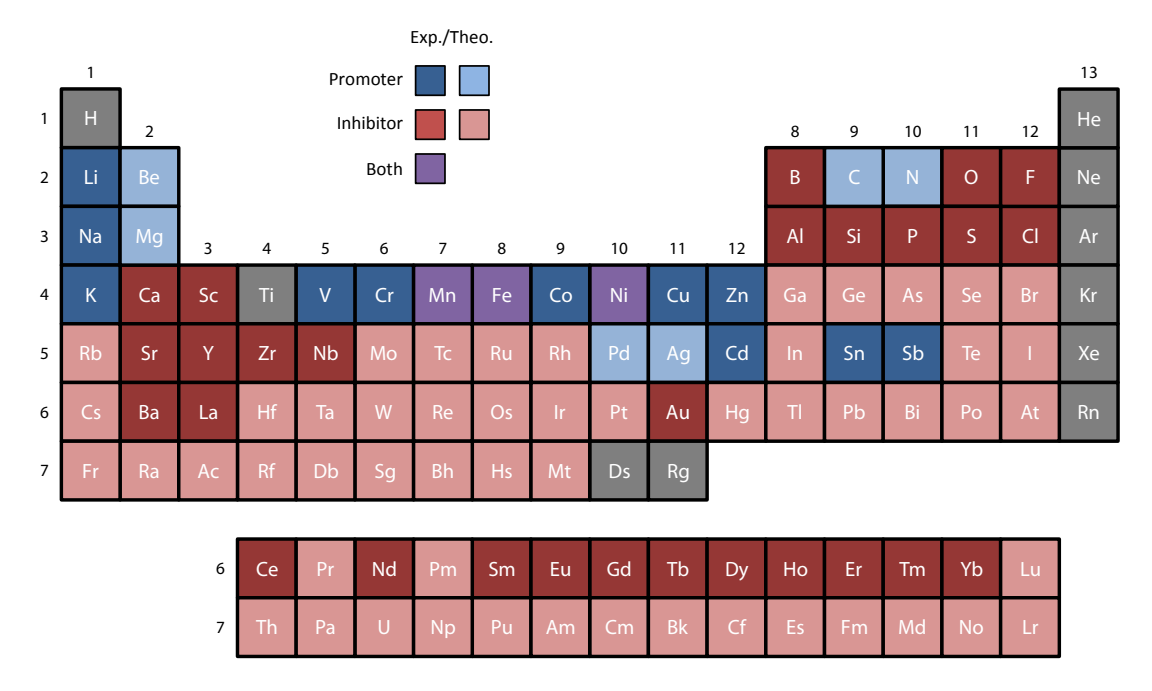


Figure 2.4 | **Summary of the influence of dopants on the TiO**₂ **phase transformation.** Experimental results from literature and theoretical predictions using the boundary line (Eq. 2.2) in Fig. 2.3 as well as additional considerations discussed in [HS11] have been used to predict the influence of dopants for which no experimentally obtained data on the anatase to rutile transformation are available so far. Data taken from [HS11].

doping with elements of valence 2 and 3 it can be concluded that the formation of oxygen vacancies has a stronger impact than the formation of Ti interstitials.

Using the boundary line (Eq. 2.2) in Fig. 2.3 and additional considerations discussed by Hanaor and Sorrell [HS11] allows the prediction of the influence of dopants for which no experimentally obtained data on the anatase to rutile transformation are available so far [HS11]. By doing this the periodic table can be color-mapped with respect to the behavior of the individual elements on the anatase to rutile transformation. The periodic table shown in Fig. 2.4 includes all experimentally reported dopants as well as theoretically predicted promoters and inhibitors. Most dopants inhibit the phase transformation, whereas only a few, most of them already experimentally proven, promote the transformation from anatase to rutile.

As the considerations for the influence of dopants on the phase transformation of TiO₂ given so far are based on powders, the substitution of a Ti atom in Eq. 2.1 assumes that the substitution is performed in an already existent lattice. If doping is achieved upon film growth, e.g. by serial co-sputtering, interstitials do not necessarily need to be formed. In this case,

the reaction can be written as:

$$Ti + X + \left(2 + \frac{n}{2}O_2\right) \longrightarrow Ti^{4+}2O^{2-} + X^{n+}\frac{n}{2}O^{2-} + \left(2 - \frac{n}{2}\right)\square.$$
 (2.3)

In serial co-sputtering the effect of doping onto the phase formation and the anatase to rutile transformation might therefore be different to the results reported by experiments performed using TiO₂ powders.

The influence of dopants on the phase formation and transformation of TiO₂ upon doping by serial co-sputtering is discussed in Chap. 7.

Thin film deposition

All samples analyzed within this work have been deposited by magnetron sputtering and, in some cases, annealed afterwards. This chapter describes the deposition of multi-component thin films as well as the deposition equipment utilized. Different concepts and techniques for sputtering multi-component thin films are discussed and a recently published theoretical model describing the sputtering process is presented. Nevertheless, due to its complexity, many aspects of the sputtering process itself cannot be discussed in this chapter and a basic knowledge about reactive sputtering is assumed to be known. A detailed discussion of the sputtering process, the basic principle and the relevant parameters can be found in the literature [DM08].

3.1 Multi-component thin films

In order to produce multi-component thin films several different deposition techniques can be used. Concentrating on sputtering techniques, this includes

- use of compound targets,
- ♦ simultaneous sputtering from multiple targets on a stationary or rotating substrate,
- ♦ layer by layer sputtering from multiple targets on a substrate rotating along the targets
- and serial co-sputtering.

To produce metal oxides, the above mentioned techniques can be used utilizing either ceramic targets in inert or metal targets in reactive atmosphere. Reactive processes are more difficult to handle [Saf00], but ceramic targets, isolating in most cases, need RF (radio frequency; usually 13.56 MHz) or pulsed discharges [KA00]. Conductive targets on the other

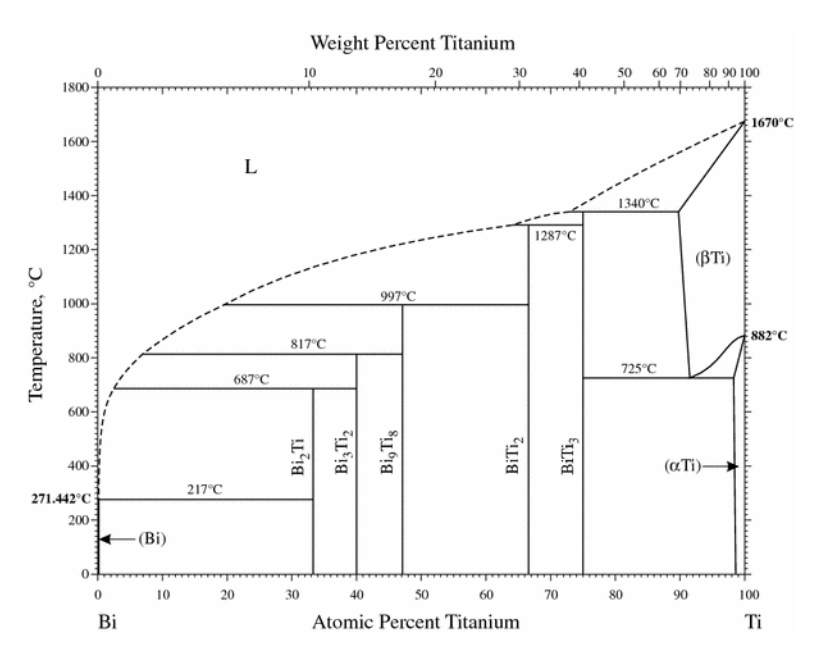


Figure 3.1 | **Phase diagram of Bi-Ti.** The maximum solubility of Bi in the α Ti phase at room temperature is less than 2 at.%, whereas the solubility at elevated temperatures in the β Ti phase is of about 10 at.%. Taken from [Oka10].

hand can be sputtered using DC (direct current) discharges, which do have a higher deposition rate at same power compared to the corresponding compounds, and are therefore preferred in industrial processes, if available. Substoichiometric targets (e.g. $TiO_{1.8}$) combine the advantages of conductivity, gentle process behavior and a high deposition rate [OTM $^+$ 01, KDM $^+$ 08], but are more complicated to produce.

From the above mentioned possibilities to produce multi-component thin films, some are not favorable for a systematic study of the influence of different dopants. Compound targets for example, having a fixed stoichiometry, are obviously favored in processes, in which the optimal composition for the desired films is already known, but a more flexible process is needed in this work. Additionally, the production of doped compound targets can be difficult for specific material combinations due to different melting points and occurring segregation as can for example be seen in the phase diagram of Ti-Bi in Fig. 3.1. Reactive sputtering from two planar targets at the same time onto a stationary or rotating substrate may be challenging due to cross talk between the atmospheres of the targets [MR99].

Therefore, serial co-sputtering has been applied in this work, which offers great flexibility and control of the dopant content, separated atmospheres for all targets as well as a homogeneous deposition [Bel93, CBBK93, SPSU10]. The utilized setup as well as the process parameters are described in the next section.

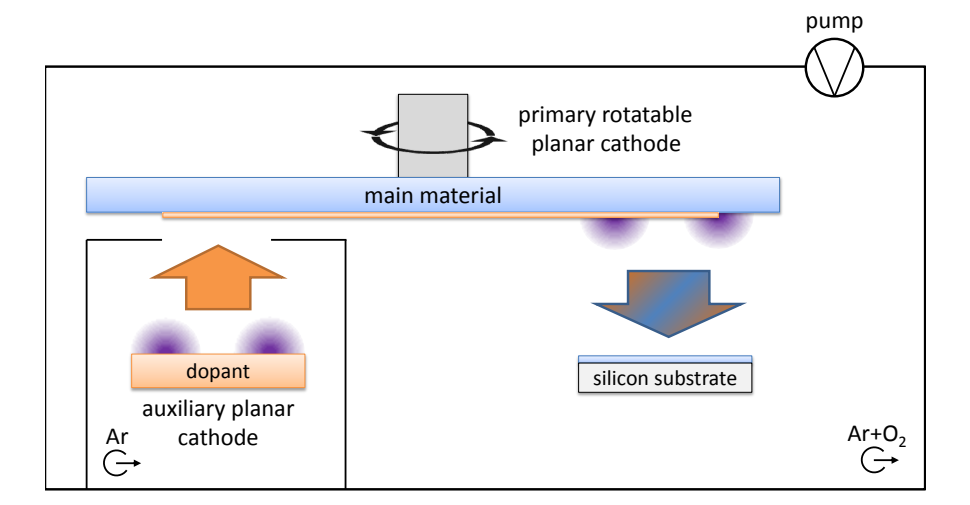


Figure 3.2 | Schematic of the principle of serial co-sputtering. The principle of serial co-sputtering is based on a primary rotating target, which is simultaneously coated with a dopant material from an auxiliary target in a non reactive atmosphere. Due to the rotation, the dopant is transported into the primary erosion zone, where the doped target surface is sputtered in an Ar/O_2 environment and doped films are deposited. A gas shielding of the auxiliary discharge volume allows independent operation at different pressures in each volume.

3.1.1 COSMOS

Serial co-sputtering of doped carbon and Ti thin films was performed using a custom made lab coater system called COSMOS (serial \mathbf{co} -sputtering for functional \mathbf{m} ulti \mathbf{co} mponent thin films). As summarized in Fig. 3.2, the principle of serial co-sputtering is based on a primary rotating target, which is simultaneously coated with a dopant material from an auxiliary target in a non-reactive atmosphere. Due to the rotation, the dopant is transported into the primary erosion zone, where the doped target surface is sputtered in an Ar/O_2 environment and doped films are deposited. A gas shielding of the auxiliary discharge volume allows independent operations at different pressures in each volume. By changing either the auxiliary or primary target power, the O_2 flow or the total pressure, the stoichiometry of the deposited films can be modified. Additionally, the dopant deposition rate can be controlled by inserting different apertures between auxiliary and primary target. Four aperture sizes, named: S, M. L and XL are available.

For the depositions performed in this study, the rotating primary ring-shaped target had an inner and outer diameter of 150 mm and 300 mm, respectively, whereas the cylindrical auxiliary targets had a diameter of 75 mm. For the depositions, identical magnetrons were installed for the primary and auxiliary discharge and constant pressures of 0.4 Pa and 5 Pa were used in the main and auxiliary chamber, respectively. The pressures were moni-

tored using MKS Baratron capacitance gauges in all volumes. To keep the pressure constant, an MKS 647C control unit was used for the main chamber, utilizing a computer controlled feedback loop, while MKS type 250 controllers equipped with proportional valves were employed for the auxiliary volumes. The gas flows for the sputter atmospheres were controlled by MKS flow controllers. For all depositions, the target-to-target and target-to-substrate distances were 65 mm and the rotation speed of the rotary target was 8 rpm. A substrate holder, capable of holding up to 24 samples, shielding all other samples except the one exposed to the plasma, was used in order to allow a whole series of samples to be deposited without breaking the vacuum. Prior to the deposition experiments, the lab coater system had been pumped down to $< 2 \times 10^{-4}$ Pa by two Pfeiffer turbo-molecular pumps (TMU 521 P and HiPace 700) backed by a scroll pump (Edwards XDS 10).

Both sputter cathodes were operated simultaneously by an Advanced Energy dual channel Pinnacle DC power supply $(2 \times 10 \text{ kW})$. In the case of HiPIMS deposition (see Sect. 3.4), a MELEC SPIK 2000 A pulsar was included between the power supply and the target generating pulses with 50 μ s on-time and a frequency of 488 Hz. Constant discharge currents at the rotating primary target of 350 mA and 800 mA were used for the deposition of carbon and TiO₂, respectively. The deposition of the dopants from the auxiliary cathode onto the rotating target was performed using DC discharges. The power of the auxiliary discharge was varied to allow for different dopant deposition rates, but was held constant during the deposition of each sample. A discussion of the deposition rates of the utilized dopants is given in Appx. B.

A more detailed description of the lab coater design, its equipment and controlling system is provided in [Aus11, AKZ⁺11].

3.2 The upgraded Berg-Model

The variable parameters in a sputter process include gas flows, pumping speed as well as the discharge parameters. Normally, the target stoichiometry is defined by the target itself. Using serial co-sputtering, the target stoichiometry can be modified in situ, giving rise to a new way to alter the process conditions. To gain insight into the influence of dopants onto the process behavior, hysteresis curves can be recorded. Hereby, it is important to have a fundamental understanding of the participating effects to be able to interpret the changes of the curves correctly.

The original Berg-model published by S. Berg in 1987 [Ber87] is a powerful way to describe the hysteresis behavior of a sputtering process with a minimum set of parameters. Even

though the model uses a rather simple mathematical description and neglects various phenomena, like atom sputtering, the predictions of the model fit experimental results quite well for a wide range of sputter conditions [BN05]. Recently, an updated version of the original model was published by Berg et al. [BSN14]. The upgraded model includes atomic sputtering instead of compound sputtering, ion implantation and knock-in effects. With this addition, it is now possible to predict e.g. changes in the hysteresis when changing the target current, which was not possible with the original model. Here, an overview of the new model is given based on the recent publication [BSN14].

3.2.1 Poisoning mechanisms

Chemisorption of reactive gas molecules is the only mechanism considered in the original Berg-model. In contrast, three mechanisms are considered to cause compound formation in the upgraded Berg-model:

- Chemisorption of reactive gas atoms,
- bombardment with ionized reactive gas molecules and
- ♦ knock-in of surface reactive gas atoms by bombardment with Ar ions.

It is assumed that implanted and chemisorbed reactive gas atoms form a homogenous compound layer without a gradient. Besides the dissociative chemisorption of neutral reactive gas molecules at the target surface, the target will be bombarded by ionized reactive gas molecules and Ar. The bombardment with reactive gas molecules leads to incorporation and therefore possible compound formation somewhat below the target surface [DCE+02, DHG02], whereas the bombardment with Ar may knock-in surface reactive gas atoms deeper into the target [RKBM05]. There is a probability that these knocked-in atoms do not find a free metal atom and therefore are released from the target. In equilibrium, the number of ejected reactive gas atoms needs to be equal to the number of incorporated and chemisorbed atoms. The mechanisms described here are in contrast to the original Bergmodel, which assumed that compound formation happens at the target surface by dissociative chemisorption of neutral gas molecules, exclusively.

3.2.2 Preferential sputtering

In the original Berg-model, atoms were either sputtered as metal atoms from the metal region of the target or as compound molecules from the compound region. The upgraded model includes atomic sputtering of single atoms and by that preferential sputtering of the, in general, lighter reactive gas atoms. The following sputtering yields are used:

- \diamond sputtering yield of metal atoms from metallic target regions ($Y_{\rm mm}$)
- \diamond sputtering yield of metal atoms from compound regions (Y_{mc})
- \diamond partial sputtering yield of reactive gas atoms from compound regions (Y_c)

Preferential sputtering of reactive gas atoms is achieved by assuming $Y_c \ge Y_{mc}$.

3.2.3 Equilibrium

In Fig. 3.3, all gas flows and mechanisms altering the metal and compound fractions of target and substrate are summarized. In equilibrium, all of these contributions form a steady-state and the fractions of compound and metal regions stay constant. The chemisorption of reactive gas molecules per unit time and unit area can be described by

$$2\alpha F(1-\Theta_{t}), \tag{3.1}$$

where α denotes the reaction probability of an reactive gas molecule, F denotes the flux of reactive gas molecules per unit time and unit area and Θ_t denotes the compound fraction of the target. As reactive gas molecules consist of two atoms (e.g. O_2), the factor 2 is added to account for the fact that 2 compound molecules will form out of one reactive gas molecule. Besides chemisorption, compound molecules in the target will be formed due to direct implantation of reactive gas molecules:

$$2\alpha_{\rm i} \frac{J}{q} \left(\frac{P}{P_{\rm A} + P} \right) (1 - \Theta_{\rm t}). \tag{3.2}$$

Here, α_i is the probability for a reactive gas ion to be implanted into the bulk target, J is the total ion current density per unit area, q is the elementary charge and P and P_A are the partial pressure of reactive gas and Ar, respectively. Gas molecules, which do not find a metal atom to form a compound molecule, desorb when they reach the target surface. The implantation of reactive gas atoms is only one consequence of the total ion current J. It also causes removal of reactive target atoms:

$$\frac{J}{a}Y_{c}\Theta_{t}.\tag{3.3}$$

In contrast to the direct removal of reactive gas atoms, some reactive gas atoms get knockedin. If these atoms end up in the compound fraction of the target, no additional compound is formed and the atoms are released. Using the knock-in yield Y_k , the rate of released gas atoms can be written as

$$\left(\frac{J}{q}Y_{k}\Theta_{t}\right)\Theta_{t}.$$
 (3.4)

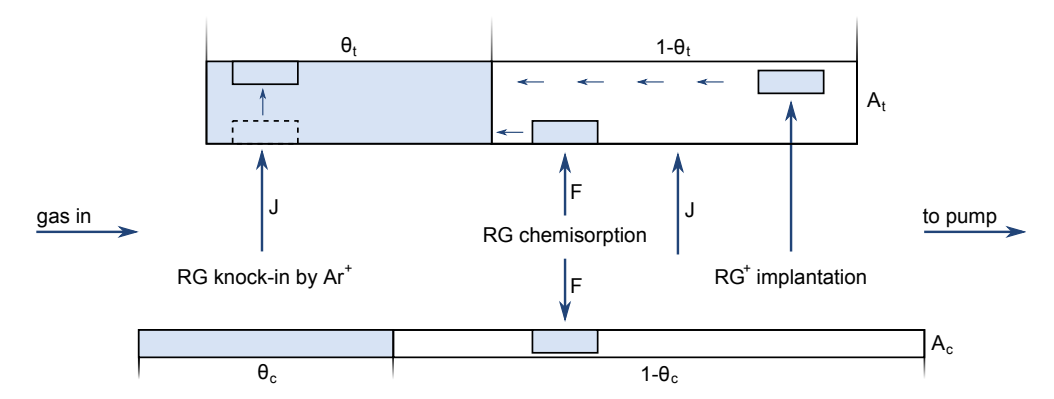


Figure 3.3 | **Mechanisms and fluxes considered altering surface and bulk composition.** The bombardment with reactive gas molecules (RG) leads to incorporation and therefore possible compound formation in a certain volume under the target surface, whereas the bombardment with Ar may knock-in surface reactive gas molecules deeper into the target. Modified with permission [BSN14].

With the equations previously described, the steady-state equation can be expressed by:

$$\left(\frac{J}{q}Y_{k}\Theta_{t}\right)\Theta_{t} + \frac{J}{q}Y_{c}\Theta_{t} = 2\alpha F(1 - \Theta_{t}) + 2\alpha_{i}\frac{J}{q}\left(\frac{P}{P_{A} + P}\right)(1 - \Theta_{t}). \tag{3.5}$$

Knowing that the reactive gas flux F is a function of the reactive gas partial pressure P and the absolute temperature T

$$F = \frac{P}{\sqrt{2kT\pi m}},\tag{3.6}$$

where k is the Boltzmann constant and m is the mass of the reactive gas molecule, the fraction Θ_t can be solved as function of F using Eq. 3.5.

3.2.4 Deposition

All sputtered metal atoms result in a flux $F_{\rm mc}$. It consists of the rate of sputtered metal atoms per unit area from the target $F_{\rm mt}$ multiplied with the effective sputter erosion zone at the target $A_{\rm t}$ and uniformly distributed at the collecting area $A_{\rm c}$:

$$F_{\rm mc} = \frac{F_{\rm mt} A_{\rm t}}{A_{\rm c}} = \frac{J}{q} \left(Y_{\rm mc} \Theta_{\rm t} + Y_{\rm mm} (1 - \Theta_{\rm t}) \right) \frac{A_{\rm t}}{A_{\rm c}}.$$
 (3.7)

As atomic sputtering is assumed and no compound will be deposited, chemisorption is the only mechanism for compound formation at the collecting area. The rate of chemisorpted reactive gas molecules is

$$F_{\rm cc} = 2\alpha_{\rm c}F(1 - \Theta_{\rm c}),\tag{3.8}$$

where α_c denotes the reaction probability of a reactive gas molecule and Θ_c denotes the compound fraction of the surface of the deposited film. The factor 2 is again added to account for biatomic reactive gas molecules. The fraction Θ_c itself must be equal to the quotient of metal atoms which form a compound by chemisorption and the total flux of arriving metal atoms at the substrate area:

$$\Theta_{\rm c} = \frac{F_{\rm cc}}{F_{\rm mc}}. (3.9)$$

As reactive gas molecules in this model can either be consumed by compound formation at the substrate area or pumped out by the system pump, the number of reactive gas atoms supplied to the chamber *Q* can be written as

$$Q = 2\alpha_{\rm c}F(1 - \Theta_{\rm c})A_{\rm c} + PS, \tag{3.10}$$

where *S* is the pumping speed of the system pump.

Using equations 3.5 - 3.10 the partial pressure P, the compound fraction of the target area Θ_t , the compound fraction of the substrate area Θ_s and the sputter erosion rate F_{mc} can be calculated as a function of the reactive gas flow Q. The major difference of these dependencies with respect to the original Berg-model is that these curves will depend on the partial pressure of Ar, which was previously neglected.

3.3 Sputter yield amplification

Particle removal by sputtering is a relatively inefficient process with only a few of the target atoms, participating in the collision cascade caused by the impinging Ar⁺ ions, leaving the target surface [Beh81]. The majority of the impinging ions' energy is lost deeper in the target as thermal heat and, in consequence, sufficient cooling of the targets has to be ensured. In reactive sputter deposition processes the oxide deposition rate is even smaller, compared to the deposition of the corresponding metal, since the surface binding energy of the oxide is higher [Dul84]. To overcome this issue, an addition of nitrogen to the process atmosphere can be used to lower the surface binding energy, as nitrides have a lower surface binding energy than oxides, and to enhance the deposition rate [SKK+06]. This approach is obviously limited to the deposition of oxides and can not be applied for the deposition of carbon and metals. For these materials, the surface binding energy can be lowered by increasing the temperature of the target [CHWL96, MLP+99, BMPF99], but sufficient cooling becomes challenging and the target design has to be modified [MPB06].

For a wide range of metals, ceramics and other materials sputter yield amplification can be used to increase the deposition rate by utilizing the so called sputter yield amplification (SYA) effect, which was first proposed by Berg et al. in 1992 [BBG⁺92, BBN⁺92]. In SYA, heavy atoms in the target act as recoil centers, which reflect the recoiled atoms towards the target surface. Hence, the depth of the collision cascade is reduced and the number of sputtered atoms per impinging ion is increased. The mass of the doping element strongly effects the efficiency of this effect.

Light elements have a higher sputtering yield than heavy elements. In consequence, these are preferentially sputtered, increasing the concentration of the heavier element at the target surface until a steady-state is reached. If the atoms are sputtered from a compound target, the partial sputter yield ratio of different constituents needs to be equal to their relative abundance in the target [BK99]:

$$\frac{\gamma_1}{\gamma_1 + \gamma_2} = \frac{C_1}{C_1 + C_2},\tag{3.11}$$

where γ_1 and γ_2 denote the partial sputter yields, and C_1 and C_2 denote the concentrations of the two target elements, respectively. The partial sputter yields of the target components are therefore directly dependent on the target stoichiometry. If the masses and densities of the corresponding parts of the compound are chosen correctly, this effect can increase the sputter yield of the lighter element above its value sputtered from a pure elemental target. While it is generally possible to produce doped compound targets, for some material combinations difficulties arise due to diverging melting points and occurring segregation. Besides, the use of compound targets is obviously difficult in experimental studies, where the doping concentration is one of the parameters to be optimized. Fortunately, the SYA effect also occurs for a target that is only contaminated with an impurity at the target surface [BBG+92], for example by serial co-sputtering [AKZ+11, KSA+12]. Hence, the deposition of heavy elements from an auxiliary target onto a primary target can be utilized to increase the deposition rate of the primary target, as is shown for carbon and TiO₂ in Chap. 5 and Chap. 6, respectively.

As the doping element is sputtered together with the target atoms, this method is inherently limited to those applications which can tolerate the incorporation of the dopant in the deposited coating. The influence of doping on the properties of TiO₂ is discussed in Chap. 7.

3.4 High power impulse magnetron sputtering (HiPIMS)

Besides the well-known and frequently applied sputter discharges like direct current (DC), pulsed direct current (pDC) and radio frequency (RF), a novel technique called high power

impulse magnetron sputtering (HiPIMS), also known as high-power pulsed magnetron sputtering (HPPMS), has drawn major attention in the past years [SAK10].

In ordinary sputter discharges, there is nearly no ion flux towards the growing film as the degree of ionization of the plasma is comparatively low [CB00]. However, high ion fluxes may be needed to achieve desired film properties, necessitating high bias voltages applied to the substrates, which result in a controlled bombardment of the growing film [PBHG03]. Unfortunately, this bombardment of the film is mainly due to Ar⁺ ions, which cause lattice defects, implantation of Ar atoms [LKR89], residual stresses [Pau01, Koc94] and weak film adhesion [Hov88].

In 1999 Kouznetsov et al. [KMS⁺99] introduced a new sputter technique using a power supply, which provides short pulses ($50\,\mu s$ to $100\,\mu s$) and a low repetition frequency ($50\,Hz$), resulting in a high degree of ionization of $70\,\%$ and the possibility to fill trenches with an aspect ratio of 1:2. High power impulse magnetron sputtering was born. Today, the range of used pulse lengths (on-times) are wide, typically ranging from $5\,\mu s$ to $5\,m s$, while the pulse repetition frequency spans from $10\,Hz$ to $10\,k Hz$, resulting in high power densities in the range of kW/cm.

There are several applications in which HiPIMS depositions are favorable. The deposited films show superior film properties like high density, low roughness [APM+05, SRW+08] and increased film adhesion [ENM+02]. Complex shaped substrates can be successfully coated by HiPIMS, for which DC discharges are not sufficient [KMS+99, APM+05]. Besides, HiPIMS has led to new products like the ice-free windshield [SDG+12].

However, besides its tremendous advantages, HiPIMS suffers from a major drawback: the deposition rate in HiPIMS is low [HLB+06]. The high degree of ionization in the discharge [GAH01, KDH06] causes the so called self-sputtering effect [Chr05], in which ionized target atoms are accelerated back towards the target. In consequence, less target atoms reach the substrates and the deposition rate is lowered. Additionally, the increased ionization is connected to a larger target voltage, which results in a smaller target current if the power is held constant. Hence, the deposition rate, which scales with the target current, is further reduced [ASMW06].

In Sect. 6.4, this drawback is addressed by using the sputter yield amplification effect (see Sect. 3.3) to increase the deposition rate of HiPIMS sputtered TiO_2 .

Analytical equipment

In this work, thin films have been investigated by use of various analytical tools to determine their properties. This chapter describes the functional principle of the techniques utilized as well as the deposition equipment employed.

4.1 X-ray analysis

X-ray measurements are a powerful tool to investigate various properties of thin films. Thickness and density values can be extracted from X-ray reflectivity measurements (XRR) [SS99], whereas X-ray diffraction (XRD) can be used to investigate the structure, grain size and texture of the sample under test [Cul78].

A schematic of an X-ray setup and some relevant angles is shown in Fig. 4.1. The sample under test is exposed to a monochromatic X-ray beam of wavelength λ at an incident angle ω . The reflected or diffracted beam gets detected by a detector at the angle 2θ with respect to the incident beam. During the measurement, the detector and/or the sample is moved to scan the angular range of interest, whereby the utilized scan and sample-to-detector geometry is chosen with respect to the desired information.

In this work, all X-ray measurements were performed with a Philips X'Pert PRO MRD diffractometer (45 kV, 40 mA) using CuK_{α} radiation with a wavelength of $\lambda=1.5418$ Å. A more detailed description of the setup, its measurement techniques, adjustment and accuracy of the results can be found in [Wei02].

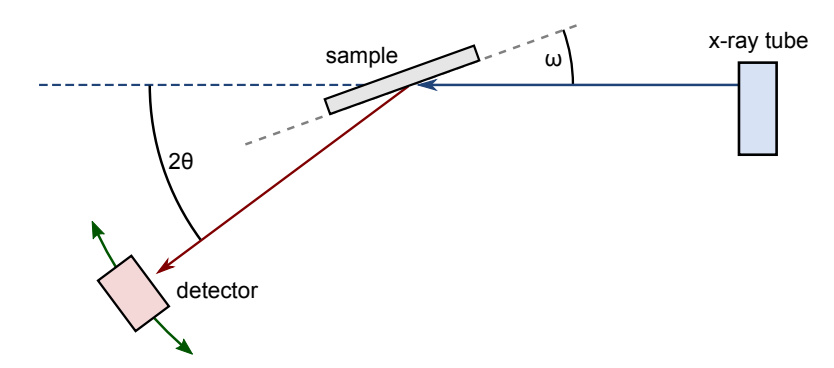


Figure 4.1 | Schematic of beam path and corresponding angles in an X-ray setup. The sample under test is exposed to a monochromatic X-ray beam of wavelength λ at an incident angle ω . The reflected or diffracted beam gets detected by a detector at the angle 2θ with respect to the incident beam. The detector is moved during the measurement to scan the angular range of interest. Depending on the measurement technique, ω can either be fixed or the sample may be turned to maintain $\omega = \theta$.

4.1.1 X-ray reflectivity (XRR)

In X-ray reflectivity measurements, sample and detector are moved simultaneously to maintain the same angle between sample and incident beam as well as between sample and detector. Since ω equals θ in this case, this scan is called $\theta/2\theta$ -scan or Bregg-Brentano-scan [Bre24].

The measured intensity is a superposition of all reflected beams from surface and interfaces of the sample. Below a critical angle θ_C , the X-ray beam is not capable of penetrating the sample and the full intensity is reflected. Above this angle, the beam reflected at the surface interferes with beams reflected at lower interfaces (e.g. layer/substrate) and the measured intensity will show interference fringes as a function of the incident angle θ . The distance between two adjacent interference maxima $\Delta\theta_{\rm max}$ is given by Bragg's law, so that the film thickness d is

$$d = \frac{\lambda}{2\Delta\theta_{\text{max}}}. (4.1)$$

As the reflectance of an interface depends on the differences in electron densities $n_{\rm e}$ of the two materials, the refractive index can be expressed as a function of the density ϱ [Wei02]

$$\tilde{n} = 1 - \frac{r_0 \lambda^2}{2\pi} \sum_{k} c_k \left(Z_k + f_k' - i f_k'' \right) \cdot \frac{\varrho}{\sum_{k} c_k M_k},$$
(4.2)

where Z_k is the atomic number, M_k represents the atomic mass, r_0 is the Bohr radius and f_k'' and f_k'' denote correction terms to the complex atom form factor \tilde{f}_k . The sum over k takes into account that a material may consist of different elements, where c_k denotes the fraction

of the individual elements. Using Eq. 4.2, the density can be calculated from the critical angle θ_C using Snellius' Law.

In this work, samples were measured in an angular range from 0° to 1.5°. Subsequently, the measured data were fitted using the WinGixa software from Philips and film thickness and density values were extracted.

4.1.2 X-ray diffraction (XRD)

Upon exposing a material to an incoming wave front, each point in the material \vec{r} will emit a spherical wave with a fixed phase relationship between the primary and the emitted wave. If coherent scattering is assumed, this leads to a superposition of the scattered waves at the observation point \vec{B} . The intensity which is detected at this point is given by

$$I(\vec{K}) \propto |A_{\rm B}|^2 \propto |\int \varrho(\vec{r}) \mathrm{e}^{-i\vec{K}\vec{r}} d\vec{r}|^2,$$
 (4.3)

where $A_{\rm B}$ is the amplitude of the detected wave, $\varrho(\vec{r})$ denotes the complex scattering density, describing the phase and amplitude of each scattered wave with respect to the primary wave, and $\vec{K} = \vec{k} - \vec{k_0}$ represents the scattering vector, which is the difference in the wave vectors of the scattered and the primary wave.

For periodic structures the scattering density $\varrho(\vec{r})$ can be expressed as

$$\varrho(\vec{r}) = \sum_{\vec{G}} \varrho_{\vec{G}} e^{i\vec{G}\vec{r}},\tag{4.4}$$

where \vec{G} is a reciprocal lattice vector and $\varrho_{\vec{G}}$ denotes the fourier coefficients of the scattering density $\varrho(\vec{r})$. Insertion of Eq. 4.4 in Eq. 4.3 leads to values of the scattered intensity $I(\vec{K})$ greater zero, resulting in a Bragg reflex, only if the scattering vector \vec{K} equals a reciprocal lattice vector, which is mathematically equivalent to the Bragg equation

$$\vec{K} = \vec{G} \tag{4.5}$$

$$\Leftrightarrow \lambda = 2d_{\rm hkl}\sin\theta,\tag{4.6}$$

where $d_{\rm hkl}$ denotes the distance between two lattice planes. X-ray diffraction measurements can be performed in e.g. Bregg-Brentano ($\theta/2\theta$) or grazing incidence (GI) geometry. In grazing incidence geometry, the angle between incident beam and sample ω is fixed to rather small angles of less than 1.5° and the detector is moved in a 2θ -scan. From Eq. 4.5 and Eq. 4.6, it can be calculated that a reflex will only occur for lattice planes perpendicular to \vec{K} . A $\theta/2\theta$ -scan will therefore only probe lattice planes parallel to the substrate surface and

measurements performed in GI-geometry will show Bragg-reflexes only if the sample consists of randomly orientated crystallites. A more detailed description of the scattering theory, calculation of the measured intensities and determination of phases can be found in the literature [IL09, Spi08].

In this work, XRD analysis was performed for sputtered TiO_2 samples only. These samples show an amorphous or polycrystalline structure and were therefore analyzed by GI-XRD. For these samples it is sufficient to probe first order reflexes and therefore an angular range covering the anatase (101) and rutile (110) peak at 25.4° and 27.5°, respectively, was utilized [AKW10].

4.2 Optical analysis

One of the most important parameters for industrial applications using TiO_2 is its high refractive index [Ric04]. Direct measurements of the refractive index are difficult and indirect methods which determine the dielectric function, from which the refractive index can be extracted, are preferred. To analyze the evolution of the refractive index upon doping of TiO_2 with different elements, ellipsometry and UV-VIS-spectroscopy measurements can be performed and subsequently fitted.

4.2.1 Ellipsometry

In ellipsometry the sample under test is illuminated with light of a wide energy range (IR-UV), known polarity and known angle to the sample's normal. The reflected light, generally elliptically polarized, is detected in an energy dispersive detector and the complex reflectance ratio ρ is determined. The reflectance ratio ρ is the ratio of the Fresnel coefficients of the s- and p-polarized fractions of the reflected light, $r_{\rm s}$ and $r_{\rm p}$. These two coefficients can be parametrized by the two ellipsometric angles Ψ and Δ , which denote the amplitude component and the phase difference, respectively [TI05]:

$$\frac{r_{\rm p}}{r_{\rm s}} = {\rm e}^{i\Delta} \tan \Psi. \tag{4.7}$$

The angle of the incident light should be close to the Brewster angle of the sample to maximize the change in polarization and by that the accuracy of the measurement [TM99]. To gain access to the refractive index, the values determined for Ψ and Δ need to be modeled subsequently (see Sect. 4.2.3), since, in general, a direct conversion to optical constants is not possible.

For the measurements performed in this work a Woollam M-2000UI variable angle spectroscopic ellipsometer was used. Data were recorded in a wavelength range from 240 nm to 1700 nm at angles of 65°, 70° and 75°.

4.2.2 Ultraviolet-visible spectroscopy (UV-VIS spectroscopy)

UV-VIS spectroscopy is performed to measure the transmittance or reflectance of a sample as a function of the photon energy. The sample under test is illuminated with a light beam of known wavelength and intensity, and the intensity of the transmitted or reflected light is measured by a detector. Different light sources and monochromators are used to provide the wavelengths needed. Some setups are equipped with a beam splitter, which provides a reference beam that is used to compensate fluctuations in the intensity over time.

A Perkin Elmer Lambda 25 dual beam spectrometer, equipped with a tungsten and a deuterium light source, was used for transmittance and reflectance measurements performed in this work. As this spectrometer is originally designed to gather transmittance data only, a custom made reflectance unit was used to measure the reflectance at an angle of 8°. In this unit the intensity is reduced by additional mirrors so that the gathered raw data had to be subsequently convoluted with a reference spectra of a sputtered aluminum mirror with known reflectance. Data were gathered for the full spectral range from 190 nm to 1100 nm in steps of 0.5 nm.

4.2.3 Modeling

To gain access to the refractive index the CODE (Coating Designer) software [The12] can be utilized. In CODE a sample is described by a layer stack of different materials with individual dielectric properties. These properties can either be loaded from a database or calculated using various models. Based on the layer stack, numerous spectra can be simulated and different properties can be extracted. Among these are ellipsometry, transmittance and reflectance spectra as well as the refractive index. Comparing the simulated spectra with measured data allows the modification of the layer stack and the material properties in CODE to get a good reproduction of the experimental data and by that access to the material properties of the sample.

In this work, CODE was used to determine the refractive index at 550 nm as well as the thickness of (doped) TiO_2 thin films on glass substrates. The dielectric function of the glass substrates, which was deduced from optical measurements of an uncoated substrate, was held constant for all simulations, whereas the dielectric function of TiO_2 was altered to describe the measured data. The dielectric function of TiO_2 was modeled by an OJL model (named

OJL2 in CODE), based on the work of O'Leary et al. [OJL97], and a dielectric background consisting of a constant part as well as an additional harmonic oscillator in the UV to model a slightly inconstant offset at higher energies [Wei02].

The OJL model describes the density of states (DOS) of the conduction band $N_c(E)$ with exponential tails in the forbidden region

$$N_{c}(E) = \frac{\sqrt{2}m_{c}^{*3/2}}{\pi^{2}\hbar^{3}} \begin{cases} \sqrt{E - V_{c}}, & E \ge V_{c} + \frac{\gamma_{c}}{2} \\ \sqrt{\frac{\gamma_{c}}{2}}e^{-\frac{1}{2}}e^{\frac{E - V_{c}}{\gamma_{c}}}, & E < V_{c} + \frac{\gamma_{c}}{2}, \end{cases}$$
(4.8)

where E denotes the energy, $m_{\rm c}^*$ is a DOS effective mass in the conduction band, $V_{\rm c}$ represents the conduction band disorderless band edge, $\gamma_{\rm c}$ is the breadth of the conduction band tail and \hbar is the reduced Planck constant. Accordingly, the density of states of the valence band $N_{\rm v}(E)$ is

$$N_{\rm v}(E) = \frac{\sqrt{2}m_{\rm v}^{*3/2}}{\pi^2\hbar^3} \begin{cases} \sqrt{\frac{\gamma_{\rm v}}{2}}e^{-\frac{1}{2}}e^{\frac{V_{\rm v}-E}{\gamma_{\rm v}}}, & E \ge V_{\rm v} - \frac{\gamma_{\rm v}}{2}\\ \sqrt{V_{\rm v}-E}, & E < V_{\rm v} - \frac{\gamma_{\rm v}}{2}. \end{cases}$$
(4.9)

Here, $m_{\rm v}^*$ denotes a DOS effective mass in the valence band, $V_{\rm v}$ represents the valence band disorderless band edge and $\gamma_{\rm v}$ is the breadth of the valence band tail.

An exemplary fit of the optical data of an undoped TiO_2 sample can be seen in Fig. 4.2, the model describes the experimental data with only minor deviation. For this specimen, a refractive index of 2.46 and a sheet thickness of 102.8 nm is extracted from the simulation.

4.3 Composition

The knowledge of the stoichiometry of multi-component thin films is important to gain insight into the impact on the film and process properties of the involved elements. The sputter yield amplification effect (see Sect. 3.3) for example can be quantified by comparing the additional sputter yield per dopant atom to the yield of an undoped process.

Although it would be generally possible to calculate the stoichiometry of a deposited sample, if the rates of all components are known, this is difficult in application as no process drifts do have to occur during deposition. A more direct approach for the determination of the stoichiometry is therefore favorable.

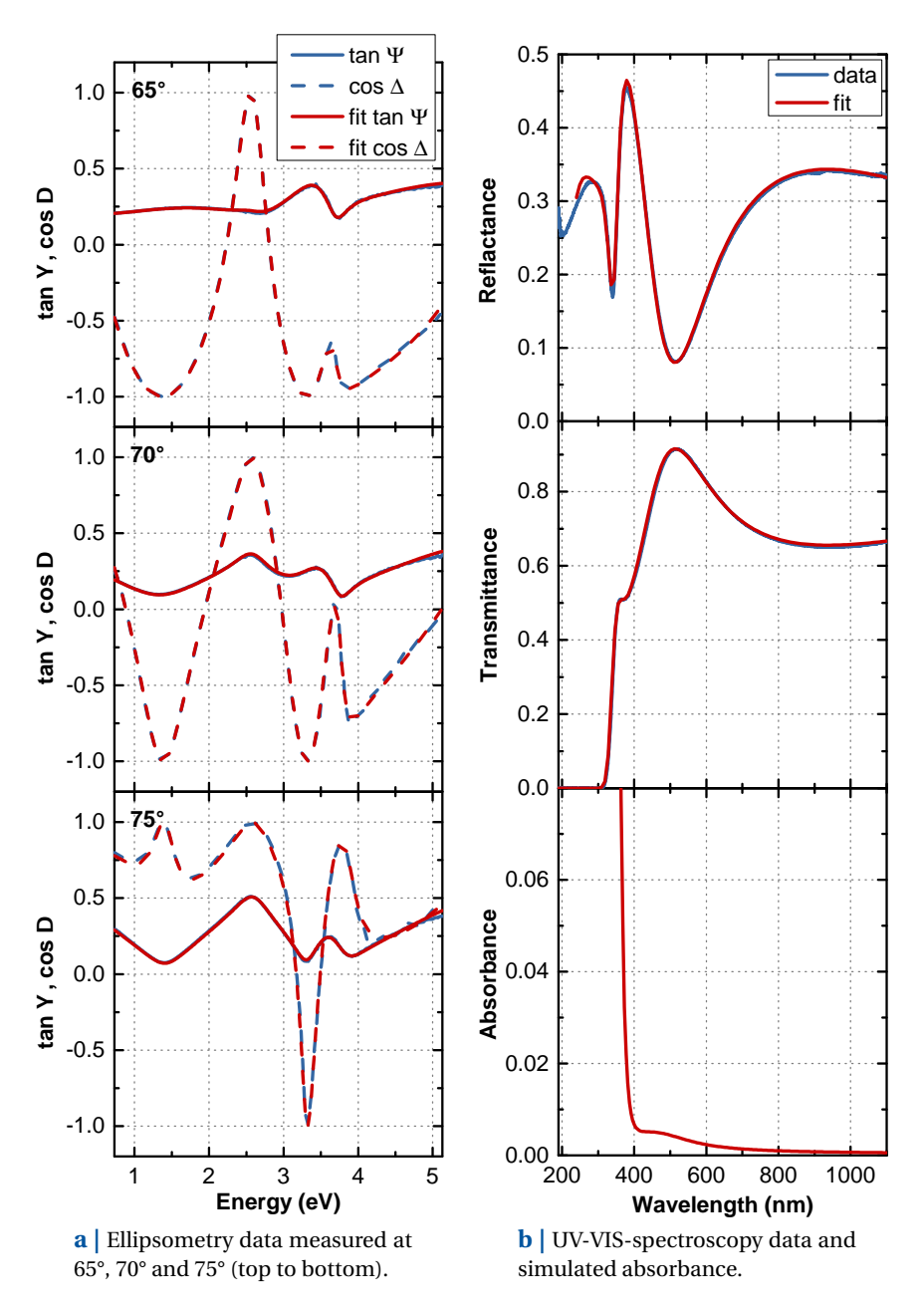


Figure 4.2 | Example of measured and simulated optical data of an undoped TiO₂ film. The CODE Software was used to model ellipsometry, transmittance and reflectance spectra of an undoped TiO₂ sample on a glass substrate. The fits are in very good agreement with the experimental data. Additionally, the absorbance, simulated at 0° and calculated by A = 1 - R - T, where R is the reflectance and T is the transmittance of the whole sample including substrate, is shown. The absorbance in the visible range is less than 1 %.

4.3.1 Rutherford Backscattering Spectrometry (RBS)

Rutherford backscattering spectrometry (RBS) is an analytical method, in which the sample under test is bombarded with high energetic ions of small mass and known energy. After collision with an atom of the sample the energy of the backscattered ion will depend on the mass of its collision partner and the energy distribution function of the scattered ions can be used to gain insight into the structure and the stoichiometry of the sample.

The energy E of a scattered ion can be written as a function of the mass of the target nucleus M, the scattering angle θ and the penetration depth z [Our03]

$$E(M,\theta,z) = \left(\frac{m\cos\theta \pm \sqrt{M^2 - m^2\sin^2\theta}}{m + M}\right) \left[E_0 - \int_0^z \left(\frac{dE}{dz}\right) dz\right] - \int_0^{\frac{z}{\cos\theta}} \left(\frac{dE}{dz}\right) dz, \quad (4.10)$$

where E_0 is the initial energy of the projectile and m is the mass of the incident nucleus. Normally, the projectile is lighter than the target and the plus sign has to be taken. If the projectile is heavier, the minus sign hast to be taken. For the latter, backscattering might not be possible and the argument of the square root can become negative. The first term in Eq. 4.10 describes the energy loss due to the collision itself in dependency of the scattering angle. This term is multiplied with the energy of the projectile at the time of the collision, which is the initial energy lowered by the energy lost due to the stopping power $\frac{dE}{dz}$ of the target material. After the collision, the ion passes through the sample back to the surface, where it leaves the sample with its final energy.

The probability of a scattering event is described by the Rutherford scattering cross section, from which the technique got its name from [Rutl1, Rutl2]:

$$\frac{d\sigma}{d\Omega} = \left(\frac{Z_1 Z_2 e^2}{16\pi\epsilon_0 E_0}\right)^2 \frac{1}{\sin^4 \frac{\Theta}{2}}.$$
 (4.11)

Here, Z_1 and Z_2 are the atomic numbers of the colliding atoms, e is the charge of an electron and Θ is the scattering angle in the center of mass frame of reference. As the scattering cross section depends on the square of the atomic numbers, this method is very sensitive to heavy atoms, but the detection of light elements as well as the discrimination between elements of similar weight is difficult.

In the experiment, the scattered ions are detected by an energy resolved detector, which counts the number of scattered ions per time and energy. This detector can either be mounted at a fixed position or an angle resolved version may be used. In the obtained spectrum, each element in the sample results in a peak with its high energy flank at a distinct energy, which reflects the elemental mass. As the ions lose energy during their way through the

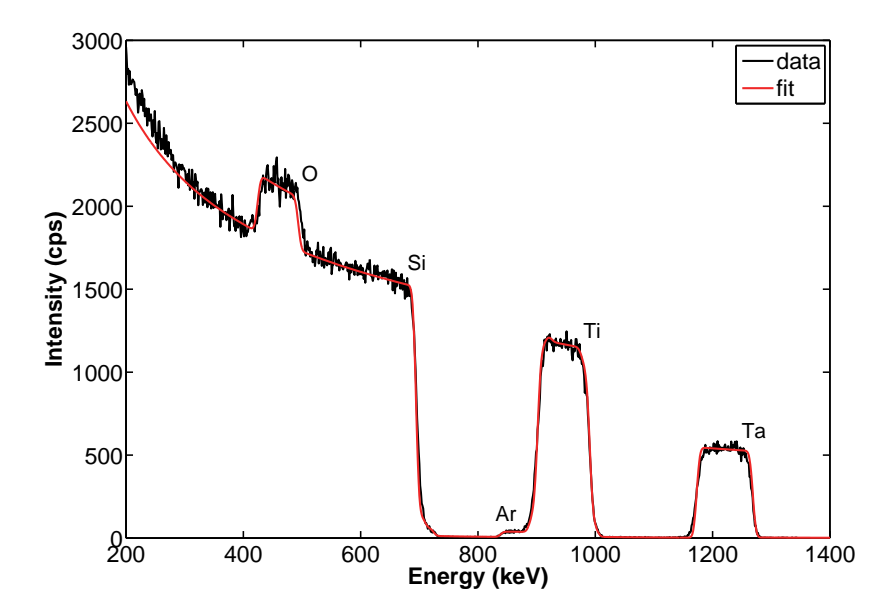


Figure 4.3 | **RBS spectrum of a TiO₂:Ta film on a silicon substrate.** The data were modeled using a composition of $TiO_{1.9}Ta_{0.045}Ar_{0.04}$. The Ar content can be attributed to Ar ions, which have been implanted during sputter deposition.

sample (see Eq. 4.10), the width of the peaks includes information about the depth of the collision partners (film thickness). Besides, from the height of the peaks the stoichiometry of the sample can be deduced [CMN78]. RBS is limited to conductive substrates or conductive films, so that the sample remains uncharged during the measurement.

A typical spectrum of a Ta-doped TiO₂ film (TiO₂:Ta) on a Si substrate is shown in Fig. 4.3. It can be seen that the Ti-peak at about 1 MeV (right flank) is only about twice as high as the Ta-peak at 1.3 MeV, even though there is more than 20 times of Ti compared to Ta in the sample. This is a good example for the sensitivity of RBS in case of heavy elements (see Eq. 4.11). In contrast to this, the oxygen peak at about 500 keV, overlapping with the broad Si background at 570 keV of the substrate, is very small although it is the element with the highest concentration. The last contribution in the spectrum comes from a small fraction of Ar. The specimen investigated was deposited by sputter deposition using Ar as an inert gas, therefore the Ar content in the film originates from Ar ions, which were implanted during sputter deposition.

In this work, all samples were irradiated with a $1.4\,\text{MeV}$ He⁺-ion beam for a fixed ion dose of $15\,\mu\text{C}$ at the Jülich $1.7\,\text{MV}$ Tandem Accelerator. The backscattered ions were detected at an angle of 170° and the resulting spectra were fitted using the RUMP software [Doo85].

4.3.2 Energy-dispersive X-ray spectroscopy (EDX)

In energy-dispersive X-ray spectroscopy (EDX) and electron probe microanalyzer (EPMA) spectroscopy, the sample under test is exposed to a high energy electron beam of several keV. The impinging electrons hit the electron shells of the sample atoms, kicking out electrons of the inner orbitals. The generated holes recombine with electrons of higher orbitals, emitting photons of distinctive wavelengths v. A detector is used to measure the number and energy of the emitted X-ray photons. As the emitted wavelengths are unique for each element, the emitted spectrum of a sample can be used to determine the stoichiometry. The wavelength of the emitted photons can be calculated by Moseley's law [Mos13]

$$v = \frac{cR(Z-S)^2}{1 + \frac{m_e}{M}} \left(\frac{1}{n_1^2} - \frac{1}{n_2^2} \right),\tag{4.12}$$

where c is the speed of light, R is the Rydberg constant, Z is the atomic number, M is the atomic mass, S is the average number of electrons between the nucleus and the electron in question, $m_{\rm e}$ is the mass of an electron, and $n_{\rm 1}$ and $n_{\rm 2}$ are the quantum numbers of the final and initial energy level, respectively.

The emitted radiation is named by the inner energy level (K, L, M) followed by a greek letter indicating the difference in principal quantum number to the outer level. Last, a numerical index may be used to distinguish between different lines due to fine structure splitting. Besides the characteristic lines of the sample elements, the spectrum consists of a continuous background from bremsstrahlung. This radiation is caused due to the deceleration of the electrons within the sample and has a sharp cutoff at low wavelengths, corresponding to the energy of the electron beam used.

For the EDX analysis in this work, a FEI Helios nanolab 650 and a Cameca SX100 EPMA were used. The energy of the electron beam was set to 10 keV and 5 keV, respectively.

4.3.3 X-ray photoelectron spectroscopy (XPS)

X-ray photoelectron spectroscopy (XPS) uses the photoelectric effect, first detected by Bequerel [Bec67] and later explained by Einstein [Ein05], to determine the surface stoichiometry of a sample.

The sample under test is irradiated by an X-ray beam of known energy and the number and energy of the emitted electrons is measured. The analyzed region is thereby limited by the attenuation length of the photons $\lambda_{\rm ph}(\omega)$, where ω is the angular frequency, and the inelastic mean free path of the electron in the solid $\lambda_{\rm e}(E,n)$, which is a function of the electron

energy E and the valence electron density n [TPP88]. Using X-ray photons, the analyzed region is of about 2 nm [TPP88, Son52], limiting this technique to the top most surface region of the sample.

The absorption of X-rays depends on the atomic number Z of the irradiated material and is given by the cross section σ [Gill1]

$$\sigma \propto Z^5 (E_{\rm ph})^{-\frac{7}{2}},\tag{4.13}$$

where $E_{\rm ph}$ is the energy of the X-ray photons. Due to the absorbed energy, electrons leave the surface with a kinetic energy $E_{\rm kin}$. The binding energy $E_{\rm B}$ of an electron can thus be calculated by

$$E_{\rm B} = E_{\rm ph} - (E_{\rm kin} + \Phi),$$
 (4.14)

where Φ denotes the work function of the detector. Resulting spectra show the number of detected electrons as a function of the binding energy. As the binding energy of the detected electrons represents the electronic configuration of the involved atoms, the elements can easily be identified. Furthermore, the number of detected electrons is proportional to the concentration of the element, which allows the calculation of the stoichiometry of the analyzed sample.

As XPS is a surface-sensitive technique, a depth profile of the sample stoichiometry can be recorded by use of an ion gun. The stoichiometry is normally plotted as a function of the sputter cleaning time, which is a first order approximation for the depth. If the sputter yields of the materials are known, the corresponding depth profile can be calculated.

For the XPS measurements performed in this work, a Specs Phoibos 100 system using AlK_{α} radiation (1.4867 keV) installed in a custom-built chamber [Sch12] was utilized. Sputter cleaning was performed using an IQE-11/35 ion gun, generating an Ar beam with an energy of 5 keV.

4.4 Optical emission spectroscopy (OES)

Using optical emission spectroscopy it is possible to identify, analyze and quantify different elements in a plasma. During sputtering, target atoms as well as inert and reactive gas atoms in the plasma get excited by collisions into an excited electronic state. The excited atoms relax to a lower or their ground electronic state emitting a photon of distinct energy $E=\hbar\omega$, where \hbar is the reduced Planck constant and ω represents the angular frequency, giving a characteristic emission spectrum for each atom and ion.

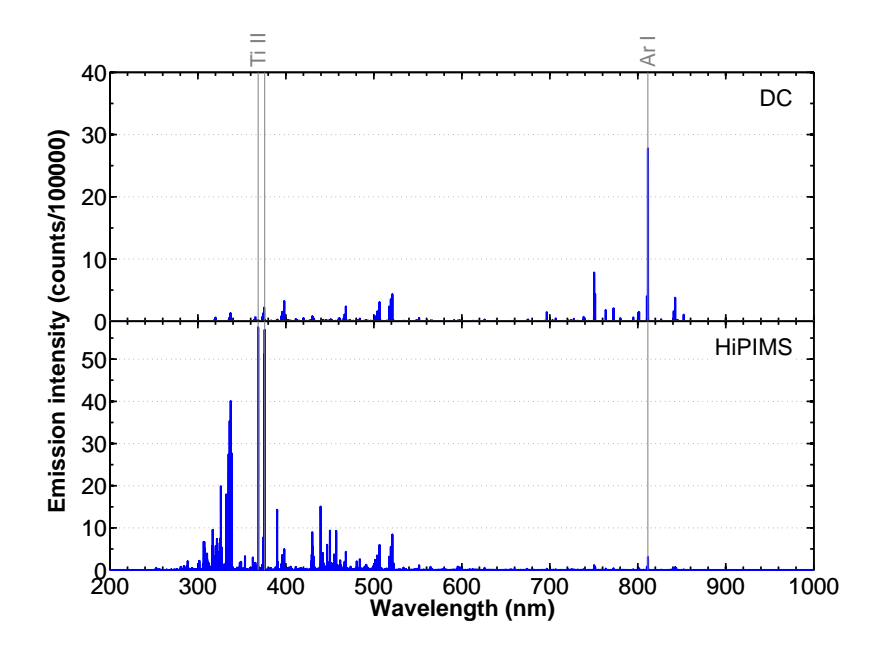


Figure 4.4 | Optical emission spectra of DC and HiPIMS sputtered TiO₂ in Ar. The spectrum of a DC discharge (top) is dominated by the emission of neutral Ar atoms at 811.5 nm [Nor73]. Using HiPIMS (bottom) the degree of ionization is much higher and the spectrum is dominated by the emission of ions at lower wavelengths. Here, the Ti II lines at 368.5 nm and 375.9 nm [Int28, DK80] show the highest intensity.

The energy differences between the electron states of an atom are unique for each element and therefore the emitted atomic spectral lines are unique for each element as well. This allows an identification of a plasma composition by recording the spectra emitted. Furthermore, the spectra emitted by neutral atoms differ significantly from spectra emitted by ionized atoms of the same element as their electronic states are altered due to the removed electrons. These differences in the emitted spectra allow an identification of different ionization states in the plasma, as can be seen in Fig. 4.4, showing the emission spectra of a DC and HiPIMS sputtered Ti target using Ar as an inert gas. The DC spectrum is dominated by the emission of neutral Ar atoms at 811.5 nm [Nor73], whereas the HiPIMS discharge is dominated by emission lines of ions at lower wavelengths due to a higher degree of ionization, with the Ti⁺ lines at 368.5 nm and 375.9 nm [Int28, DK80] having the highest intensity.

Spectrometers optimized for very short acquisition times allow for an investigation of plasma evolutions on very short time scales, e.g. in pulsed discharges like pDC [LZF⁺05] or HiPIMS [ASMW06].

The emission lines of an element are typically labeled by its atomic symbol, followed by a roman numeral, e.g. Ti II. The roman numeral thereby counts the ionization state, where I denotes the neutral atom and II represents the first ionization state and so on.

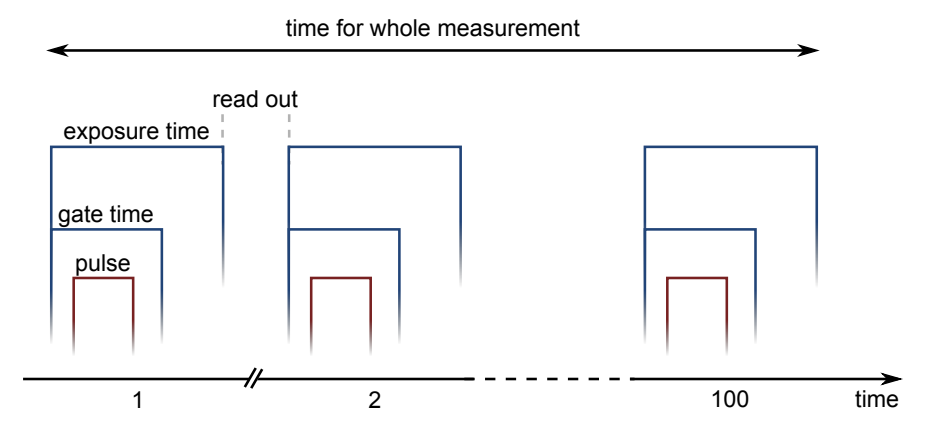


Figure 4.5 | **Timings in accumulated digital direct gate (DDG) mode.** All spectra shown in this work were recorded by accumulation of 100 acquisitions in DDG mode, which uses the intensifier of the ICCD camera as a shutter with ns time-scale. Using gate times which are similar to the pulse length allows to minimize the noise recorded by the detector. During the read out the charge-coupled device is read out and cleared for the next acquisition. The DDG mode is recommended by the manufacturer regardless of pulsed or permanent light sources are analyzed.

Fiber optics are usually employed to transfer the plasma emission to the spectrometer. Those fibers can either be mounted on view ports, having a direct line-of-sight to the plasma, or next to the plasma by use of vacuum feedthroughs. In general, the best results are achieved if the receiving optics are placed parallel to the magnetron in a way that the line-of-sight crosses the plasma ring twice. The use of fibers allows to use additional optics. Lenses can be employed to increase the intensity of the signal, whereas collimators protect fibers and lenses from being coated.

An Andor Mechelle 5000 spectrometer equipped with an intensified charge-coupled device (ICCD) camera for optimized signal count was used for the measurements performed in this work. A glass fiber with a length of 2 m and an inner diameter of 50 µm attached to the spectrometer allowed the transfer of the gathered light into the detector. Prior to the acquisitions, the spectrometer was calibrated using a mercury lamp placed directly in front of the fiber. The calibration was started by identifying the Hg I line at 253.652 nm [SSR96] and adjusting the calibration accordingly. In a second step, the calibration was redone with a higher accuracy using 6 lines. Finally, a last calibration using 18 lines of the mercury lamp could be successfully performed ensuring a precise calibration of the spectrometer. After the calibration the fiber was attached to a vacuum feedthrough at the chamber.

Light emission of the plasma was collected using collimator optics from Plasus attached to an additional single core fiber inside the chamber connected to the vacuum feedthrough. The collimator was positioned parallel to the target in a distance of about 2 cm using a custom made holding attached to the shielding of the main target of the COSMOS chamber.

Table 4.1 | **Settings used for optical emission spectroscopy of TiO₂.** All spectra shown in this work were recorded using the digital direct gate mode (DDG). The exposure time, gate time and gain were adjusted to maximize the measured intensity without saturating the detector.

Discharge	Atmosphere	Exposure time (ms)	Gate time (µs)	Gain
DC	Ar	10	3000	200
DC	Ar/O_2	10	3000	200
HiPIMS	Ar	2	50	180
HiPIMS	Ar/O_2	2	50	200

The second fiber inside the chamber had a length of 2 m and an inner diameter of $400\,\mu m$. The use of a fiber with a greater diameter inside the chamber ensured that the fiber outside the chamber was fully illuminated at the feedthrough and no signal was lost.

All spectra shown in this work were recorded by accumulation of 100 acquisitions in digital direct gate mode (DDG), which is illustrated in Fig. 4.5. The DDG mode uses the intensifier of the ICCD camera as a shutter with ns time-scale. Using gate times which are similar to the pulse length of the discharge allows to minimize the noise recorded by the detector. To ensure a correct timing of the DDG in case of a HiPIMS discharge an external trigger was used, which synchronizes the gating with the on-time of the HiPIMS discharge. The DDG mode is recommended by the manufacturer regardless of pulsed or permanent light sources are analyzed. As the light falling onto the detector without intensifier is negligible, the amount of photons can be controlled by adjusting the gate time and by that the detector can be protected from too high intensities.

The exposure time, gate time and gain of the accumulated acquisitions were adjusted with respect to the discharge utilized to maximize the intensity of each single aquisition without saturating the detector. The values used in this work are summarized in Tab. 4.1. A summary of all spectral emission lines assigned within this work including wavelengths and transition orbitals is provided in Appx. C.

4.5 Annealing

Post deposition annealing in ambient air can be performed to analyze the influence of dopants on the phase transformation of sputtered samples upon annealing (see Chap. 7).

For the annealing performed in this work, a Heraeus M 104 muffel furnace was utilized. Previous to the annealing procedure, the empty furnace was preheated to the designated temperature until no further change in temperature could be noticed. Multiple samples

were put into a metal dish and simultaneously transferred into the hot furnace. After the annealing time, the dish was taken out of the furnace and the samples were removed from the dish as soon as possible to avoid subsequent annealing. To ensure that the temperature inside the furnace was altered only slightly due to the opening, the opening times of the furnace were kept as short as possible. Samples within this work were either annealed at $300\,^{\circ}$ C for 1 h or at $700\,^{\circ}$ C for 10 min. The annealing temperatures used within this work were chosen according to tempering processes used in the architectural glazing industry [SL13].

Part II

Results

Sputter yield amplification of carbon

The simulation of sputter yield amplification in a reactive sputter process can be difficult, because suboxides, created due to the presence of dopants at the target surface, may alter the surface binding energy and by that the deposition rate of the oxide, drastically. If so, a quantitative prediction of the sputter yield amplification by simulations is nearly impossible, since the formation of suboxides can not be simulated with present tools and simulations have to be made assuming a target stoichiometry [KDM+08]. For this reason a quantitative comparison between experimental and simulated data in a nonreactive atmosphere has to be used to evaluate the accuracy of the simulation of the sputter yield amplification effect.

Carbon is hampered by a very low deposition rate due to the low sputter yield of carbon [BE07] and was therefore chosen to compare experimental and simulation results in a non-reactive atmosphere, quantitatively. The results in this chapter have already been published in [SRP+14].

5.1 Deposition rates

Doped carbon thin films were deposited using serial co-sputtering (see Sect. 3.1.1). The dynamic deposition rates of the dopants onto the rotating carbon target by use of aperture L were determined to $R_{\rm W} = 0.52\,\rm nm/Wh$ for W and $R_{\rm Nb} = 0.48\,\rm nm/Wh$ for Nb. For the deposition of the doped carbon films auxiliary powers of 100 W, 50 W, 25 W, 75 W, 0 W, 200 W and 300 W, with a pre-sputtering time of 10 min between each deposition, were applied for W,

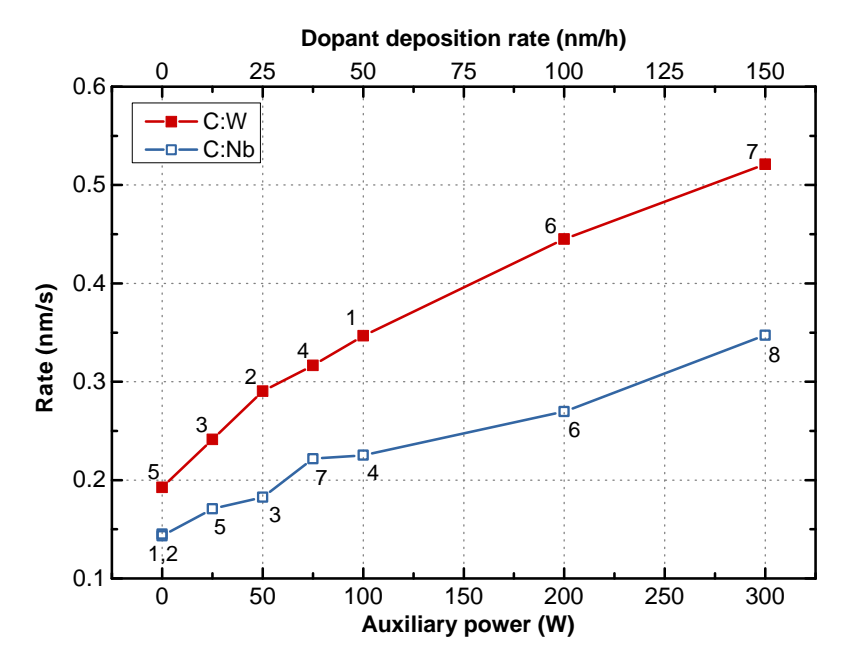


Figure 5.1 | **Total deposition rate of carbon as a function of the auxiliary power.** The small numbers denote the order of depositions. The order of depositions was chosen in order to reveal possible systematic effects caused by i.e. unintentional heating or process drifts. The difference in the deposition rates of the undoped films (at 0 W auxiliary power) is attributed to W, which remained in the target, after the experiment previously performed at 75 W auxiliary power, in line with the composition analysis reported in Fig. 5.2.

whereas auxiliary powers of 0 W, 0 W, 50 W, 100 W, 25 W, 200 W, 75 W and 300 W, with a presputtering time of 15 min in between each deposition, were applied for Nb. The order of depositions was chosen in order to reveal possible systematic effects caused by i.e. unintentional heating or process drifts. Prior to each series, the target had been sputter cleaned for 1 h.

If no dopant is present, only carbon atoms will be deposited, and the total deposition rate R equals the deposition rate $R_{\rm C}$ of pure carbon. Adding dopant material to the target will increase the deposition rate of carbon from $R_{\rm C}$ to $G \cdot R_{\rm C}$ due to the sputter yield amplification factor $G = \gamma_{\rm C}/Y_{\rm C}$, where $\gamma_{\rm C}$ and $Y_{\rm C}$ are the partial sputter yield of carbon and the sputter yield of pure carbon. The dopant will be sputtered together with carbon and the total deposition rate R can be written as

$$R = G \cdot R_{\rm C} + R_{\rm d},\tag{5.1}$$

where $R_{\rm d}$ is the rate of the dopant from the rotating target. Total deposition rates were calculated from XRR measurements to quantify the sputter yield amplification and are shown in Fig. 5.1, where the small numbers denote the order of depositions. With increasing auxiliary power and thereby increasing dopant concentration in the target, the total deposition

rate increases. It can be seen that Nb doping increases the rate of carbon from 0.15 nm/s to 0.35 nm/s and W doping to 0.52 nm/s for the maximum applied auxiliary powers of 300 W. It has already been shown that W is able to increase the rate upon serial co-sputtering of Al₂O₃ [KSA⁺12, AKZ⁺11], whereas Nb would not be effective for SYA of Al₂O₃, since its mass is too low. As the deposition rate of Nb onto the rotatory target is about equal to the rate of W and the Nb atoms have about half of the mass of W, the smaller rate increase of carbon, if doped with Nb, is expected. There is a noticeable difference between the deposition rates of pure carbon between the W and the Nb series (see Fig. 5.1). At first, this is surprising as in both cases identical deposition conditions were used and no dopant was introduced at 0W auxiliary power. Further analysis revealed that the higher rate in the W series can be correlated to W atoms, which remained in the target due to recoil implantation [BBG⁺92]. The pre-sputtering time of 10 min was not sufficient to remove all W after the prior experiment at 75 W auxiliary power. For the Nb doped session, the 0 W samples were sputtered first, after an initial sputter cleaning of 1 hour. These films were therefore used as a reference for undoped films in the calculation of the rate enhancement for both experimental series. The presence of W in the undoped films was also confirmed by the compositional analysis of deposited films, as discussed below.

5.2 Composition

The resulting film compositions were determined by EPMA and are shown in Fig. 5.2. The W content is greater than $0.4\,\%$ for all samples, as mentioned above, even for the sample sputtered with no auxiliary power. In contrast, the content of Nb is $0.21\,\%$ and $0.17\,\%$ for the two samples sputtered at $0\,\text{W}$ auxiliary power showing that the pre-sputter time of 1 hour removed most of the dopant. This also confirms that a long pre-sputtering time is indeed necessary to remove all implanted dopants. No W is found in the Nb session as the concentration is lower than $0.1\,\%$, which is the resolution limit of the technique utilized. The Nb content at 75 W is slightly higher than the trend would suggest, which can again be attributed to an effect of the preceding deposition with $200\,\text{W}$. Comparing the W-doped and the Nb-doped films reveals that the W content in the films is greater than the Nb-content at the same auxiliary power. In equilibrium, the number of dopant atoms sputtered from the rotatory cathode $\dot{n}_{\rm d}^{\rm rot}$ is equal to the number of atoms deposited onto the rotatory cathode from the auxiliary cathode $\dot{n}_{\rm d}^{\rm aux}$

$$\frac{dn_{\rm d}}{dt} = \dot{n}_{\rm d} := \dot{n}_{\rm d}^{\rm aux} = \dot{n}_{\rm d}^{\rm rot},\tag{5.2}$$

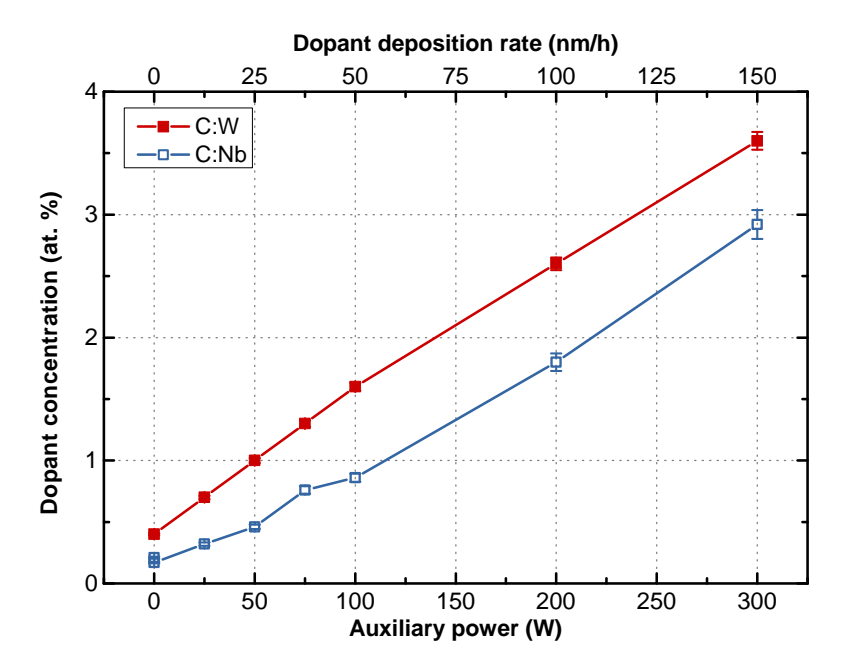


Figure 5.2 | **Dopant content of the sputtered films as a function of the auxiliary power.** Film compositions were measured by EPMA. The W content is greater than 0.4% for all samples even for the sample sputtered with no auxiliary power. W remained in the target during the pre-sputtering time of 10 min in between the depositions.

so that a higher dopant content can be directly attributed to a higher rate of dopant atoms deposited onto the primary cathode. The relation between the number of sputtered Nb and W atoms per time can be calculated from the dopant deposition rates $R_{\rm Nb}$ and $R_{\rm W}$, the mass densities $\varrho_{\rm Nb}$ and $\varrho_{\rm W}$ as well as the atomic masses $M_{\rm Nb}$ and $M_{\rm W}$ of Nb and W, respectively

$$\frac{\dot{n}_{\rm d}^{\rm W}}{\dot{n}_{\rm d}^{\rm Nb}} = \frac{R_{\rm W}\varrho_{\rm W}}{R_{\rm Nb}\varrho_{\rm Nb}} \cdot \frac{M_{\rm Nb}}{M_{\rm W}} = 1.5,\tag{5.3}$$

where mass densities obtained by XRR measurements of $13.95\,\mathrm{g/cm^3}$ and $5.05\,\mathrm{g/cm^3}$ for W and Nb, respectively, are used. This explains why the dopant content in the W-doped film is higher than in the Nb-doped films although the deposition rates of W and Nb are similar. Considering that the number of sputtered carbon atoms per time is amplified from $\dot{n}_{\rm C}$ to $G\cdot\dot{n}_{\rm C}$ due to the presence of the dopant, the dopant concentration c in the resulting film can be written as

$$c = \frac{\dot{n}_{\rm d}}{\dot{n}_{\rm d}^{\rm total}} = \frac{\dot{n}_{\rm d}}{\dot{n}_{\rm d} + G \cdot \dot{n}_{\rm C}} \tag{5.4}$$

where \dot{n}_d^{total} is the total number of atoms sputtered from the rotatory target per time.

Table 5.1 | **Material constants used in TRIDYN model.** Default TRIDYN values of the relocation threshold, atomic density and surface binding energy were used [Beh81].

Element	Atomic mass (u)	Relocation threshold (eV)	Atomic density (10 ²⁴ /cm ³)	SBE (eV)
С	12	25	0.114	7.41
Nb	92.9	28	0.0552	7.6
W	184	38	0.0632	8.68

5.3 Simulation

The sputter process was simulated by the binary collision approximation (BCA) code TRI-DYN [MEB88] using a model described in detail elsewhere [KNP+10]. In the model, a single point at the primary target is followed during rotation. Each turn of the primary target is described within two simulation steps: First, the surface gets coated by a thin layer of the dopant. Second, in the primary erosion zone, sputter erosion of the target takes place. A carbon target sputtered in a pure Ar atmosphere with W and Nb doping elements was assumed. Material parameters used in the simulations are summarized in Tab. 5.1, other parameters of the model were treated according to [MG07]. Simulations were performed for a cylindrical rotating magnetron with a diameter of 10 cm and a 6 cm wide erosion zone in a 0.4 Pa Ar atmosphere. A rotational speed of 8 rpm and a constant discharge voltage of 500 V resulting in a current density of 0.1 A/cm² were used, comparable to the experimental conditions.

5.4 Comparing experiment and simulation

To allow a fair comparison of the simulations as well as the experimentally determined rates and to compensate the different numbers of sputtered atoms per power from the auxiliary cathodes for the two dopants, the rate enhancement as well as the sputter yield amplification factor of carbon can be calculated. The simulations assumed that the density ϱ of the compound is equal to linear combinations of the elemental densities, providing an estimate for the expected density

$$\varrho = \varrho_{\rm C} + (\varrho_{\rm d} - \varrho_{\rm C}) \cdot c, \tag{5.5}$$

where ϱ_C is the density of carbon and ϱ_d is the density of the dopant. Here, mass densities of $2.25\,\mathrm{g/cm^3}$, $8.57\,\mathrm{g/cm^3}$ and $19.3\,\mathrm{g/cm^3}$ for the pure elements carbon, Nb and W are used, respectively. Film densities of the sputtered compound layers were deduced from X-ray reflectometry measurements. Fig. 5.3 shows the extracted values for different dopant contents. The heavy W atoms increase the density by up to $1\,\mathrm{g/cm^3}$, whereas Nb changes

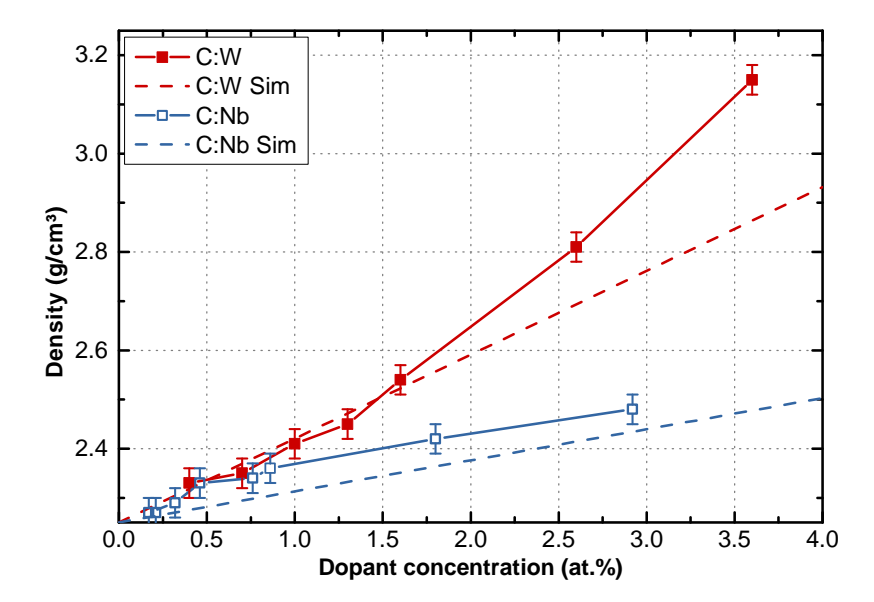


Figure 5.3 | Density of doped carbon films as a function of dopant concentration. The heavy W atoms increase the density by up to $1\,\mathrm{g/cm^3}$, whereas Nb changes the density by $0.2\,\mathrm{g/cm^3}$ only. The dashed lines show simulated results assuming that the compound density equals a linear combination of the elemental densities.

the density by $0.2\,\mathrm{g/cm^3}$ only. The simulations are included in Fig. 5.3 as dashed lines and are in an acceptable agreement with the data obtained. For higher dopant concentrations of W, the measured densities are higher than the calculated values, which is an indication for densification due to a higher bombardment of the film. Due to the presence of heavy recoil centers in the target, the impinging Ar ions may get reflected. The reflected Ar neutrals hit the growing film and could enhance the density [Mül86].

The rate enhancement factor F of the compound is defined as the ratio of the deposition rates of the doped $R_{\rm doped}$ and undoped $R_{\rm undoped}$ process and is approximately equal to the sputter yield amplification factor G of carbon if the fraction of sputtered dopant atoms is low and the densities remain constant

$$F := \frac{R_{\text{doped}}}{R_{\text{undoped}}} = \frac{\dot{n}_{\text{d}} + G \cdot \dot{n}_{\text{C}}}{\dot{n}_{\text{C}}} \approx G = \frac{\gamma_{\text{c}}}{Y_{\text{C}}}.$$
 (5.6)

For large values of $\dot{n}_{\rm d}$, the approximation $\dot{n}_{\rm d} \ll \dot{n}_{\rm C}$ is incorrect since the number of sputtered dopant atoms adds to the total deposition rate significantly. The simulations give direct access to all fractional sputter yields allowing a direct calculation of the sputter yield amplification factor G. In contrast to this, the rate enhancement factor can not be directly accessed by the simulation as the density of the resulting film is unknown and has to be calculated assuming constant elemental densities. For the experimental data, the sputter yield ampli-

fication factor can be calculated if the stoichiometry and the density of the film is known

$$G = \frac{\gamma_{\rm c}}{Y_{\rm C}} = \frac{\dot{n}_{\rm C}^{\rm SYA}}{\dot{n}_{\rm C}} = \frac{R_{\rm doped} \cdot \varrho}{R_{\rm undoped} \cdot \varrho_{\rm C}} \cdot \frac{M_{\rm C}(1-c)}{M_{\rm C}(1-c) + M_{\rm d} \cdot c},\tag{5.7}$$

where $\dot{n}_{\rm C}^{\rm SYA}$ is the number of sputtered carbon atoms in the presence of a dopant and $M_{\rm d}$ and $M_{\rm C}$ are the atomic masses of the dopant and carbon, respectively.

In Fig. 5.4, both values, the rate enhancement factor F and the sputter yield amplification factor G, are plotted against the dopant concentration. The simulations give a quantitative reproduction of the experimental results with an excellent agreement up to 2 at.% of dopant concentration. Above this value the deviation between the simulated and the experimental data is somewhat larger. It can be seen that W is more effective in increasing the deposition rate of carbon, because it results in a higher rate enhancement factor for the same dopant concentration. Nevertheless, it is notable that Nb increases the rate substantially, despite its lower mass. The experimental data shows a steeper increase of the total sputter yield than the simulation in which the slope decreases slowly with increasing dopant content for higher concentrations. Comparing both plots, one can see that the predicted additional sputter rate above a concentration of about 5 at.% is mainly due to the additionally sputtered dopant atoms, as the sputter yield amplification factor becomes constant at this point. At a certain amount of doping, the target surface is saturated with dopant atoms. Any additional doping atoms will quickly be sputtered away and therefore will not increase the carbon yield anymore [AKZ⁺11, KSA⁺12]. The experimental data shows no saturation in rate enhancement for the doping concentrations analyzed. Hence, it could be possible to use even higher dopant concentrations to further increase the deposition rate.

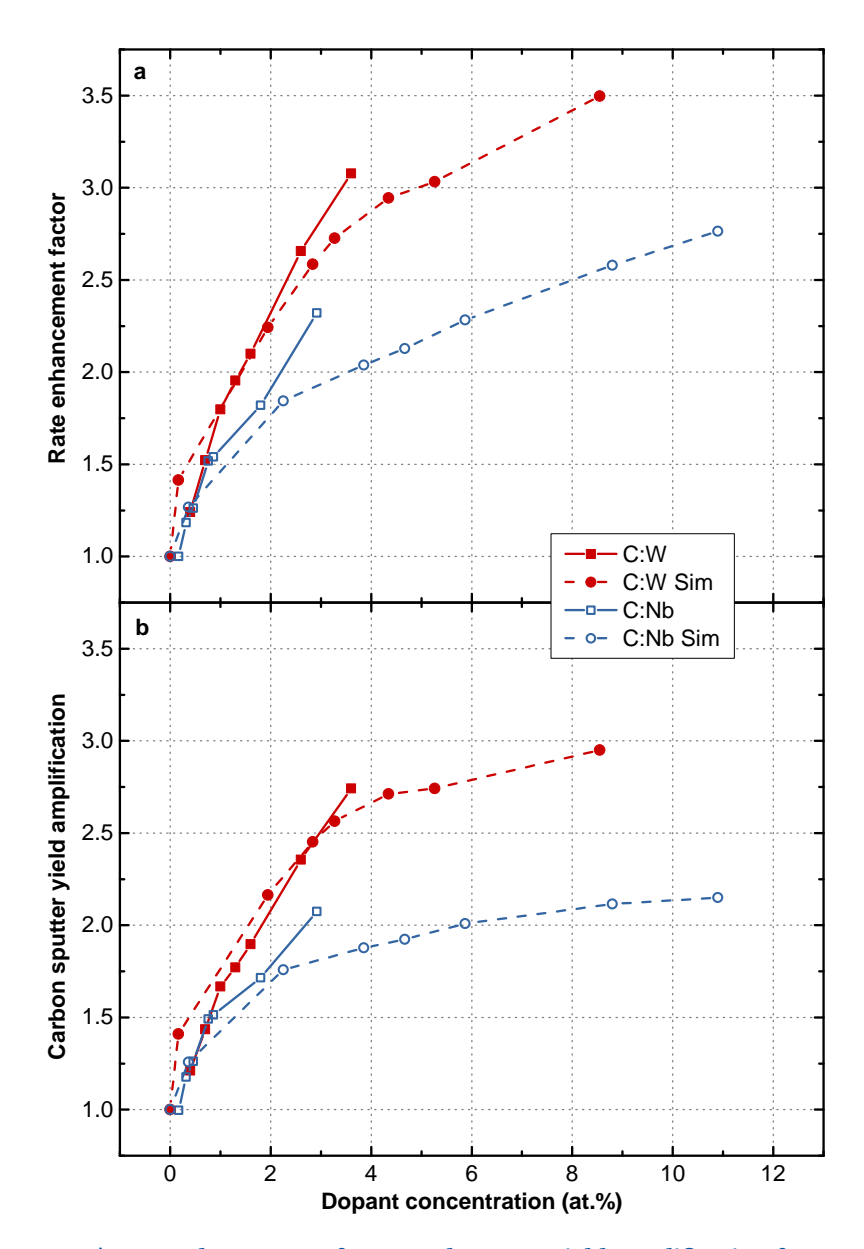


Figure 5.4 | Rate enhancement factor and sputter yield amplification factor of carbon. Rate enhancement factor (a) and sputter yield amplification factor (b) of carbon as a function of the dopant content in the resulting film. The circles (dashed lines) show data gathered from TRIDYN simulations, whereas the squares (solid lines) represent experimental data gathered from thickness measurements (XRR) and stoichiometry measurements (EPMA). A good agreement between the experimental data and the simulations is found.

Sputter yield amplification of TiO₂

Upon reactive sputtering, TiO_2 suffers from a comparatively low deposition rate. By doping with heavy elements this issue can be overcome using the sputter yield amplification effect. Previously, it has been shown by Austgen [Aus11] that Bi is not capable of increasing the sputter yield, although this was predicted theoretically [SPSU10]. Doping with W on the other hand results in a significant rate increase of TiO_2 . Austgen concluded that an effective sputter yield amplification does not only require a high mass, but also a high surface binding energy of the dopant. This could be confirmed by Kubart et al. for Al_2O_3 [KSA+12] by use of TRIDYN simulations in line with the results from Berg et al. [BBG+92].

In this chapter, the results for sputter yield amplification of TiO₂:W are reproduced and additional dopants, namely Pb, Ta and Hf are investigated with respect to their capability to increase the deposition rate of TiO₂. It is shown that the surface binding energy is indeed one of the crucial parameters, nevertheless there are more effects that alter the strength of the sputter yield amplification effect, which have not been considered by established models so far.

Using HiPIMS for the deposition of TiO_2 reduces the deposition rate even further [HLB $^+$ 06], as the high ionization lowers the target current [ASMW06] and self-sputtering reduces the number of target atoms reaching the substrate [Chr05]. Consequently, sputter yield amplification was utilized to increase the deposition rate in HiPIMS. The results are shown in the second part of this chapter. The resulting rate enhancement is significantly higher than in a DC process. Additional experiments, explaining that the stronger amplification is originated in a deeper implantation of the dopant, are provided.

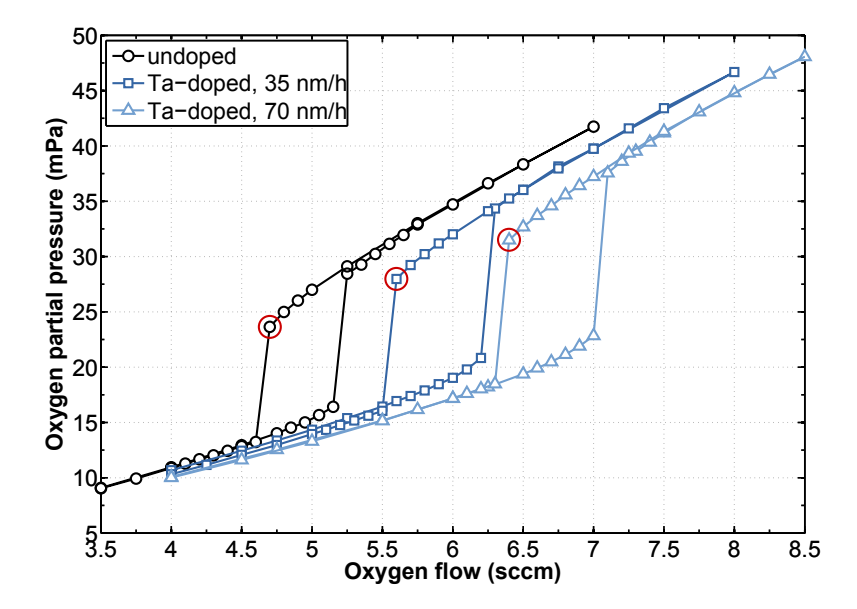


Figure 6.1 | O_2 partial pressure hysteresis shift upon doping of TiO_2 with Ta. The O_2 partial pressure hysteresis is shifted to higher O_2 flows upon doping with elements, which cause sputter yield amplification, in this case Ta. To maintain a fair comparison of the different rates of these processes, gathered data can be plotted as a function of the O_2 flow after the corresponding transition point (marked by red circles).

6.1 Quantification

In order to be able to compare rates of different reactive sputtering sessions, it is necessary to find a good reference point. High deposition rates are generally favored in industrial applications and films, sputtered as close as possible to the transition point coming from oxide mode to metal mode, where the rates are at their maximum [BN05], are preferred. This transition point can act as a reference point, when comparing different sessions, in order to maintain a fair comparison. Hence, data of this work are plotted as a function of the O_2 flow after the corresponding transition point if reasonable. An example of three hysteresis curves of a Ti target, sputtered in reactive atmosphere using different Ta deposition rates onto the rotating target, is given in Fig. 6.1. Due to the sputter yield amplification caused by Ta the oxygen consumption in the process is higher compared to the undoped process and the hysteresis curve is shifted to higher O_2 flows. To compare the rates of the three processes, the last stable point in oxide mode (marked by red circles), called transition point (TP), is used as a reference, since this point corresponds to the highest deposition rate, which results in stoichiometric films. At this point, further decrease of the O_2 flow results in a metallic deposition, whereas an increase of the O_2 flow results in a lower deposition rate.

For each dopant material investigated, hysteresis curves were recorded and samples were sputtered at different O_2 flows after the transition point. The resulting films were investigated by XRR and deposition rates were calculated from the gathered data. The results for W-doped TiO_2 can be seen in Fig. 6.2a, containing the deposition rates as a function of the O_2 flow after the transition point. An exponential function

$$R = R_0 + a \cdot e^{bF}, \tag{6.1}$$

where R is the deposition rate, F is the O_2 flow and R_0 , a and b are independent fit parameters, was fitted to each data set to interpolate the data to the full O_2 flow range.

The use of higher auxiliary powers and thereby higher deposition rates of dopant from the auxiliary cathode onto the primary target, results in a higher TiO2 deposition rate. At the transition point the deposition rate of TiO2 is amplified from 0.41 nm/s of the undoped process to 0.51 nm/s, 0.61 nm/s and 0.87 nm/s for dopant deposition rates onto the primary target of 13 nm/s, 26 nm/s and 52 nm/s, respectively. To quantify the enhancement, the rate enhancement factor (see Eq. 5.6) can be calculated. As data points are not available for the whole plotted O2 range in Fig. 6.2a for all data sets, the interpolated curves are used to calculate the enhancement. The results can be seen in Fig. 6.2b, which shows a significant rate enhancement factor of 1.22, 1.47 and 2.10 for a dopant deposition rate onto the primary target of 13 nm/s, 26 nm/s and 52 nm/s, respectively. With increasing O₂ flow, the rate enhancement increases until it saturates at about 3 sccm after the transition point for the 13 nm/h and 26 nm/h doped films and at about 4 sccm after the transition point for the 52 nm/h doped films. This is due to the fact that the deposition rate of TiO₂ decreases with increasing O₂ flow (see Fig. 6.2a), but the deposition rate of the dopant onto the primary target remains constant due to gas separation. In consequence, there is a higher dopant concentration in the target for higher O2 flows, which results in a higher rate enhancement factor. This can be confirmed by EPMA measurements of the dopant concentration in the resulting films as a function of the O₂ flow plotted in Fig. 6.2c. A clear increase of dopant concentration can be seen with increasing O₂ flow. The dopant content in the film is less than 3 at.% for all samples at the transition point and increases up to values of 9 at.% at an O₂ flow of 6 sccm after the transition point.

Using the data of Fig. 6.2b and Fig. 6.2c, it is possible to plot the rate enhancement factor as a function of the dopant concentration, which can be seen in Fig. 6.3. In a first approximation, the rate enhancement depends linearly on the dopant content and therefore a higher dopant concentration results in a higher rate enhancement. As the same dopant content for different O_2 flows does not correspond to the same deposition rate, it is favorable to sputter at low O_2 flows and high auxiliary rates, where the rate is generally higher and the dopant

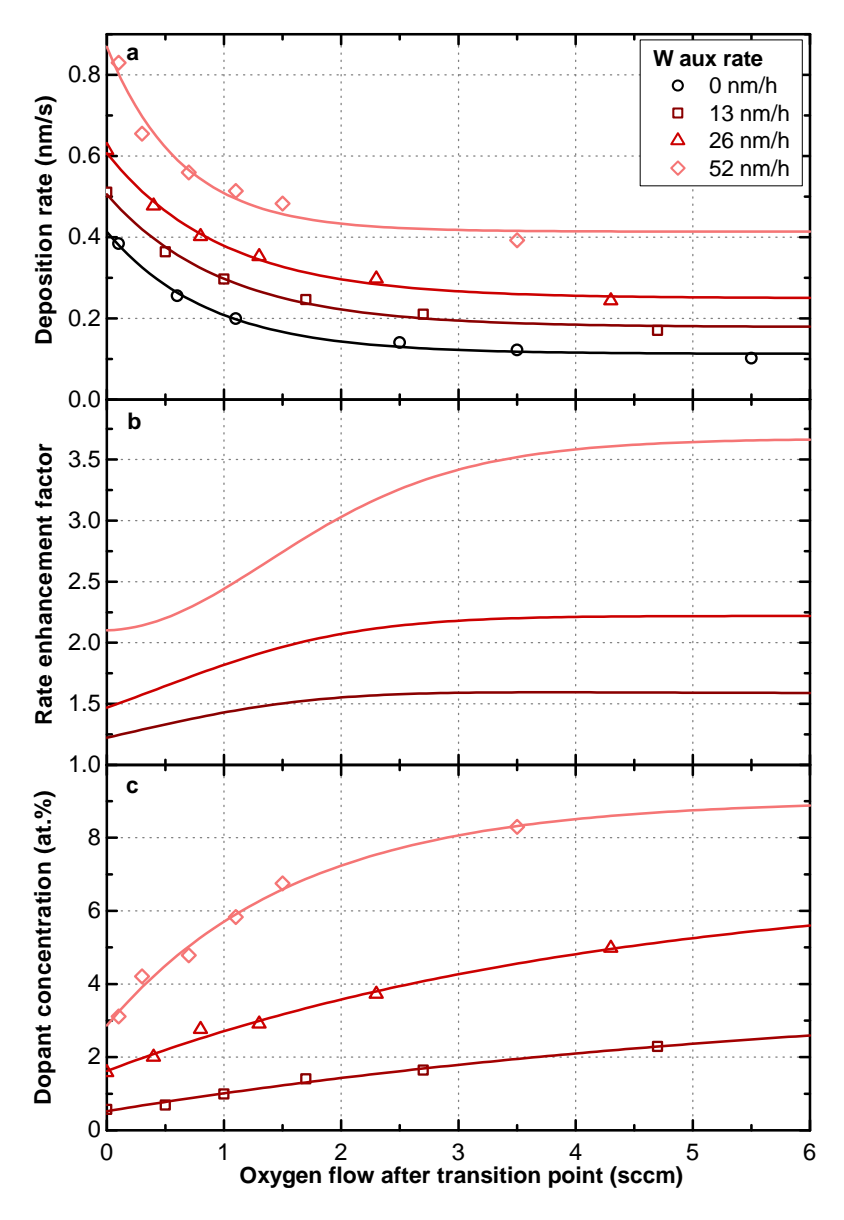


Figure 6.2 | Deposition rate, dopant content and rate enhancement of TiO_2 :W. The deposition rate of undoped and W-doped samples was measured using XRR (a) and the rate enhancement factor was calculated by normalizing the deposition rates of the doped samples to the undoped ones (b). EPMA measurements were performed and resulting compositions are plotted as a function of the O_2 flow (c). With increasing O_2 flow the deposition of TiO_2 decreases, but the deposition rate of the dopant remains constant (gas separation). This results in an increasing dopant concentration and consequently in a higher rate enhancement with increasing O_2 flow.

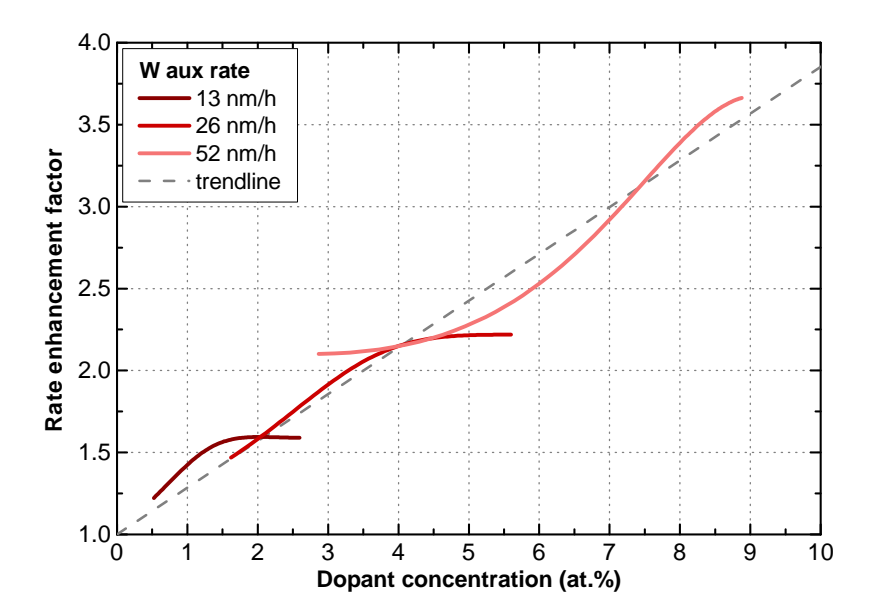


Figure 6.3 | Rate enhancement as a function of dopant content. Describing the dopant content and the rate enhancement as a function of the O_2 flow, the rate enhancement can be plotted as a function of the dopant concentration. In a first approximation, the dependence is linear (dashed trendline), a higher dopant concentration results in a higher rate enhancement. The dopant content can be used to compare the effectiveness of different dopants materials quantitatively.

content in the resulting film is minimal. The previously mentioned linear dependency of the rate enhancement on the dopant content allows the dopant content to be used as a basis for comparison of the effectiveness of different dopant materials by comparing the rate enhancement at a specific dopant content.

The way of quantifying the rate enhancement for TiO_2 :W presented in this work is different from the way of Austgen [Ausl1]. The quantification of the the sputter yield amplification differs due to the different ways of comparing the data sets. Austgen compared rates at the same absolute O_2 flow, whereas in this work the transition from oxide to metal mode is used as a reference point. Besides, the dopant concentrations presented here were calculated by using only the metal fraction of the film, independent of the oxygen content, which allows for using the results to produce doped targets. This is also different to the work of Austgen, who plotted dopant concentrations as a fraction of all atoms in the film. Taking these facts into account, the results in this study are in very good agreement with the data presented by Austgen, reproducing the effectiveness of W for the sputter yield amplification of TiO_2 qualitatively as well as quantitatively.

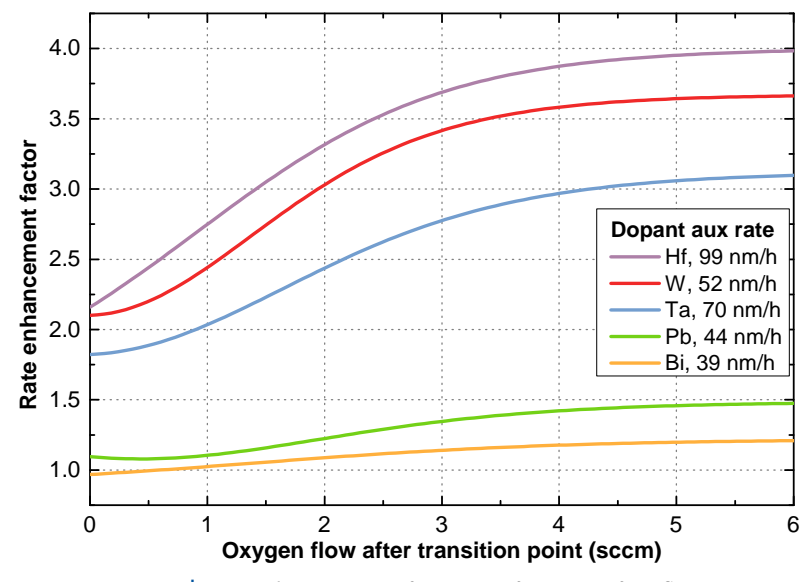
Table 6.1 | Comparison of atomic mass, density and SBE of Hf, Ta, W, Pb and Bi. The density and the surface binding energy (SBE) of Hf are lower than those of Ta and W, although Hf shows a more pronounced rate increase of TiO₂. For the values of the surface binding energy, values of the sublimation energy are used instead.

Element	Atomic mass (u)	Density (g/cm ³)	SBE (eV) [Lid97]
Hf	178.5	13.3	6.41
Ta	181.0	16.7	8.10
W	183.8	19.25	8.80
Pb	207.2	11.3	2.02
Bi	209.0	9.79	2.17

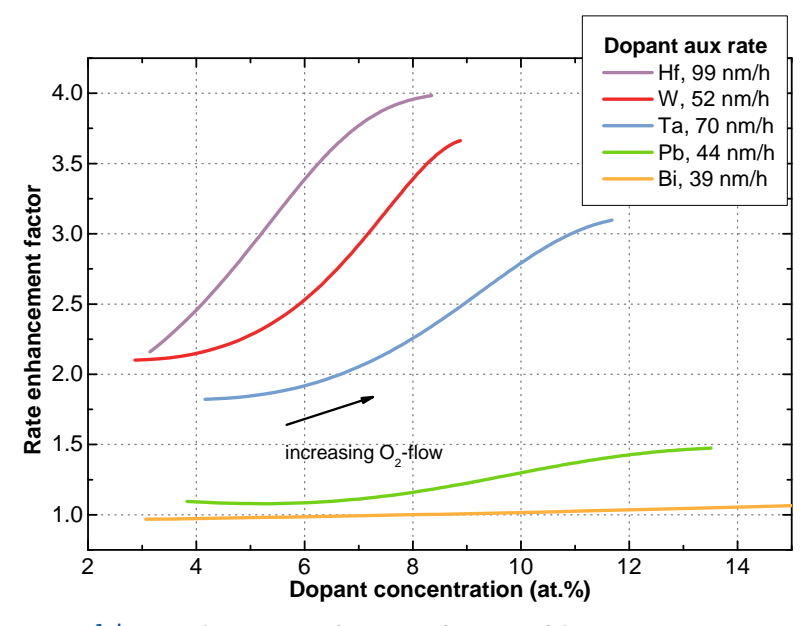
6.2 Dopant comparison

Additionally to W, the dopants Hf, Ta, and Pb were investigated with respect to their rate enhancement potential and Bi data were included from [Aus11]. For each dopant material, data were gathered and evaluated in the same way as described above. The resulting curves for the rate enhancement as function of the O_2 flow and the dopant concentration are presented in Fig. 6.4. Hf and W are the most effective dopants which result in a rate increase of more than 100% at the transition point. Ta is also effective showing an increase of 80%, whereas Pb and Bi result in nearly no rate increase at the transition point. The rate enhancement factor increases with increasing O_2 flow, due to a higher dopant concentration, as has been discussed before, and ends up in a maximum rate enhancement factor of 3.1, 3.7 and 4.0 for Ta, W and Hf, respectively (see Fig. 6.4a).

Using RBS and EPMA measurements, the results can be plotted as a function of the dopant concentration, as can be seen in Fig. 6.4b. Knowing that the dopant concentration is independent of O₂ flow and dopant deposition rate, this is the best way to compare different rate enhancements. Fig. 6.4b shows that the rate enhancement per atom is maximal for Hf, followed by W and Ta. The ineffectiveness of Pb is in line with the conclusion of Austgen [Aus11] that suggests a low amplification for materials with low surface binding energy and T-DYN simulations performed for sputtering of a metallic Al target by Berg et al. [BBG⁺92], who correlated the sputter yield amplification with the density of the impurities. Hf, Ta and W on the other hand, having a somewhat lower mass, result in a much higher rate increase due to their higher surface binding energy and density. The values for the atomic mass, density and sublimation energy, which is used in T-DYN [BK99] and other cases [KVGA05] as surface binding energy, are summarized in Tab. 6.1. For heavy atoms, the surface binding energy of the pure metal can also be used as the surface binding energy of the corresponding oxide, since sputtering is dominated by the mass difference between the metal and oxygen



a Rate enhancement of TiO_2 as a function of O_2 flow.



b | Rate enhancement of TiO_2 as a function of dopant concentration.

Figure 6.4 | Rate enhancement of TiO_2 as a function of O_2 flow and dopant concentration. Hf, W and Ta result in a major rate increase, whereas Pb and Bi do not increase the rate of TiO_2 significantly, despite having a higher mass (a). By use of RBS or EPMA analysis the rate enhancement can be plotted as a function of the dopant concentration, decoupling the enhancement from the auxiliary rate and the O_2 flow (b). The rate enhancement of Hf is higher at each concentration making it the most efficient dopant analyzed. Bi data taken from [Aus11].

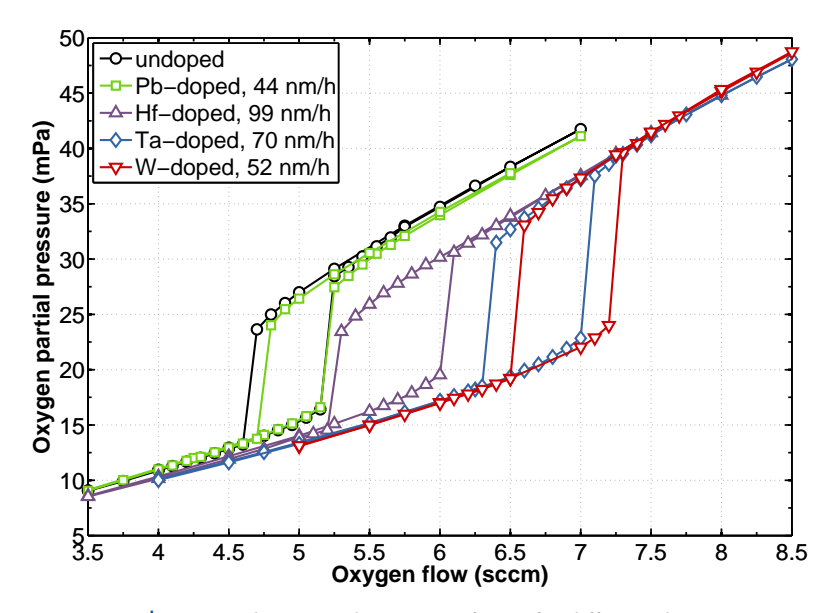
as has been shown by Baretzky et al. for Ta [BMT92]. In consequence, all dopants, with the exception of Hf, are in line with the conclusions of Austgen [Aus11] and Berg et al. [BBG $^+$ 92]. The density as well as the surface binding energy of Hf is lower than those of Ta and W. Consequently, there must be another explanation for the high rate enhancement of TiO₂ upon doping with Hf.

6.2.1 Target hysteresis

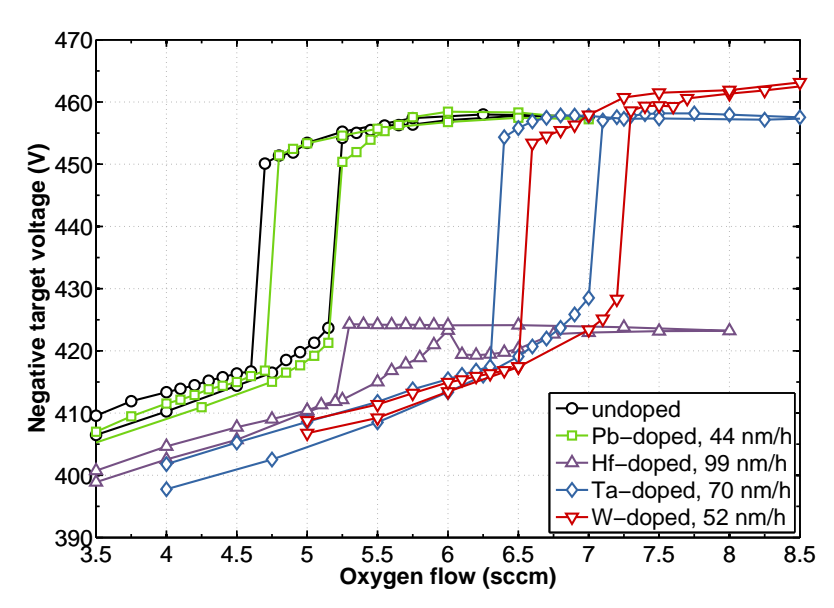
To gain a deeper insight into the sputter dynamics, hysteresis curves of doped TiO_2 processes are shown in Fig. 6.5. In general, the shift of the hysteresis curves to higher O_2 flows can be explained by a higher oxygen consumption due to a higher deposition rate [Aus11]. This is true for all analyzed dopants except Hf, which results in a much smaller shift of only 1.1 sccm compared to Ta and W, which result in a shift of 1.7 sccm and 1.9 sccm, respectively. The width of the hysteresis curve of TiO_2 :Hf is also broader than that of TiO_2 :Ta and TiO_2 :W.

But not only the O_2 partial pressure hysteresis of TiO_2 :Hf shows a unique behavior, the same is also true for the voltage hysteresis. The negative target voltage of Hf-doped TiO_2 in oxide mode is only about 425 V, which is close to the voltage of an undoped process in metal mode. The corresponding negative target voltage in oxide mode of all other doped TiO_2 processes is much higher and has a value of about 455 V. All samples were sputtered using a constant current and therefore the voltage drop is the result of a lower plasma impedance caused by a higher secondary electron emission. This, in turn, is an indication for a change in target chemistry due to the presence of Hf. It is known that HfO_2 has a higher secondary electron emission coefficient than TiO_2 [NKMW04]. Still, the voltage should increase upon increasing the O_2 flow since the total secondary electron coefficient would be lowered if Ti gets oxidized. As the target voltage stays about constant for all O_2 flows, this indicates that the oxygen is bound mainly to Hf instead of Ti. The simulations of Berg et al. are based on ballistic processes only and assume that no chemical compounds between the species are formed [BBG+92, BBN+92, BK99], which explains why such behavior could not be simulated using the model utilized.

In order to show that the lowering of the target voltage in Fig. 6.5b is due to the chemical behavior of Hf, hysteresis curves were recorded using an isoelectrical dopant, namely Zr, which has also been shown to have a higher secondary electron emission coefficient than Ti [NKMW04]. In Fig. 6.6 two hysteresis curves of TiO_2 :Zr with different dopant deposition rates as well as an undoped reference are shown. The transition points of the processes are located at higher O_2 flows compared to Fig. 6.5, as all three curves were recorded in a freshly cleaned (sand blasted) chamber, which shows a more pronounced getter effect [DG04]. It



a | O₂ partial pressure hysteresis of TiO₂ for different dopants.



b | Target voltage hysteresis of TiO₂ for different dopants.

Figure 6.5 \mid O₂ partial pressure and voltage hysteresis of TiO₂ for different dopants. In general, the shift of the hysteresis curves to higher O₂ flows can be explained by a higher oxygen consumption due to a higher deposition rate. This is true for all analyzed dopants except Hf, which results in a much smaller shift compared to Ta and W, but having an even higher rate. The target voltage of TiO₂:Hf in oxide mode is lower than for all other curves. All samples were sputtered using a constant current, therefore the voltage drop is the result of a lower plasma impedance caused by a higher secondary electron emission.

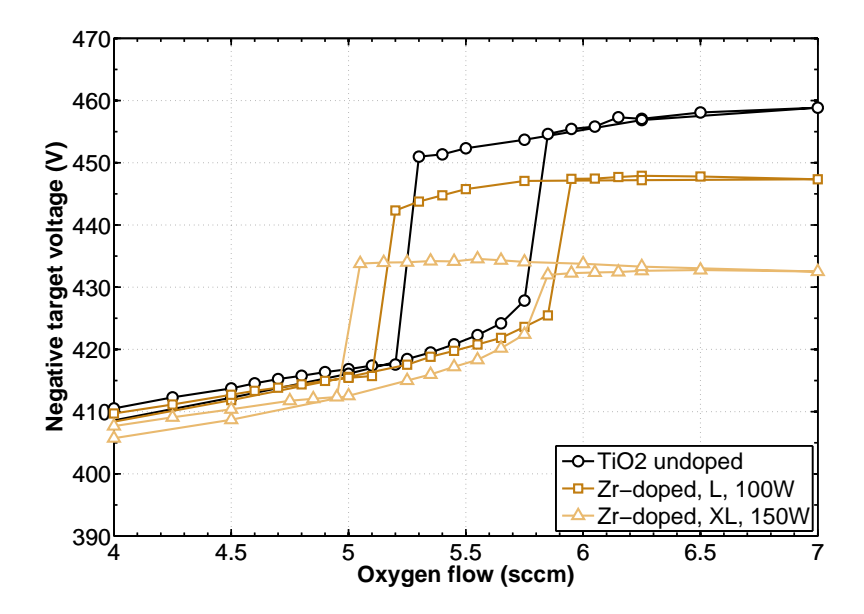


Figure 6.6 | Target voltage hysteresis evolution of TiO₂ upon Zr doping. TiO₂ was doped with Zr using an auxiliary power of 100 W and 150 W together with aperture L and XL, respectively. Upon doping of TiO₂ with Zr the negative target voltage is reduced substantially compared to the undoped case. The transition points of all curves are located at higher O₂ flows compared to the measurements shown before (see Fig. 6.5) due to a stronger getter effect of a freshly cleaned chamber.

can be seen that due to the presence of Zr the negative target voltage is reduced substantially compared to the undoped case, like it has been seen before for Hf in Fig. 6.5b. Both isoelectric elements, Zr and Hf, cause a drop of the target voltage in oxide mode. Nevertheless, the effect is more pronounced for Hf than for Zr. A lower negative target voltage is connected to a higher secondary electron emission, which can be explained by both, the higher secondary electron emission coefficient of ZrO_2 as well as HfO_2 and due to a more metallic target surface caused by the formation of TiO_{2-x} suboxides.

To explain why TiO_{2-x} suboxides might be formed in the presence of Zr and Hf, it is necessary to understand, whether TiO_2 or a dopant oxide Me_xO_y is formed at the target surface. The reaction

$$\frac{y}{2} \cdot \text{TiO}_2 + x \cdot \text{Me} \longrightarrow \frac{y}{2} \cdot \text{Ti} + \text{Me}_x \text{O}_y$$
 (6.2)

will take place if the total difference in Gibbs energy of the reaction is negative:

$$\Delta G = \Delta G \left(\frac{y}{2} \cdot \text{TiO}_2 + x \cdot \text{Me} \longrightarrow \frac{y}{2} \cdot \text{Ti} + \text{Me}_x \text{O}_y \right)$$
 (6.3)

$$= \Delta G(\text{Me}_x O_y) - \frac{y}{2} \cdot \Delta G(\text{Ti}O_2) < 0. \tag{6.4}$$

Table 6.2 | Properties of metal oxides formed upon doping of TiO₂. Standard molar enthalpy (heat) of formation $\Delta_f H^0$, standard molar Gibbs energy of formation $\Delta_f G^0$ and standard molar Gibbs energy of formation normalized to one oxygen atom $\Delta_f G^0/n(O)$ at at 298.15 K for different metal oxides [Lid97]. The formation of ZrO₂ and HfO₂ is favored in comparison to TiO₂. Doping TiO₂ with Zr or Hf this leads to a more metallic target surface, a lower target voltage and a higher sputter yield.

Material	$\Delta_{\rm f} H^0$ (kJ/mol)	$\Delta_{\rm f}G^0$ (kJ/mol)	$\Delta_{\rm f} G^0/n({\rm O})~({\rm kJ/mol})$
TiO ₂	-944.0	-888.8	-444.4
ZrO_2	-1100.6	-1042.8	-521.4
HfO_2	-1144.7	-1088.2	-544.1
Ta_2O_5	-2046.0	-1911.2	-382.2
WO_3	-842.9	-764.0	-254.7

Eq. 6.2 can also be rewritten as

$$Ti_{0.5}O + \frac{x}{y} \cdot Me \longrightarrow \frac{1}{2} \cdot Ti + Me_{x/y}O,$$
 (6.5)

so that the total difference in Gibbs energy ΔG can be determined by simply subtracting the Gibbs energy of the two metal oxides normalized to one oxygen atom:

$$\Delta G = \Delta G(\text{Me}_{x/y}\text{O}) - \Delta G(\text{Ti}_{0.5}\text{O}). \tag{6.6}$$

Tab. 6.2 shows the standard molar enthalpy (heat) of formation $\Delta_f H^0$, standard molar Gibbs energy of formation $\Delta_f G^0$ and standard molar Gibbs energy of formation normalized to one oxygen atom $\Delta_f G^0/n(O)$ at 298.15 K for the metal oxides of Ti, Zr, Hf, Ta and W. Zr and Hf are the only analyzed dopants, which lead to a preferred formation of their dopant oxide since their values for the standard molar Gibbs energy of formation normalized to one oxygen atom $\Delta_f G^0/n(O)$ are lower than that of TiO₂ and for this reason, the preferred oxidation for Ta and W will not take place:

$$TiO_2 + Zr \longrightarrow Ti + ZrO_2$$
 (6.7)

$$TiO_2 + Hf \longrightarrow Ti + HfO_2$$
 (6.8)

$$5TiO_2 + 4Ta \rightarrow 5Ti + 2Ta_2O_5$$
 (6.9)

$$3\text{TiO}_2 + 2\text{W} \longrightarrow 3\text{Ti} + 2\text{WO}_3.$$
 (6.10)

Note that above discussed equations are only valid if the amount of O_2 is limited and the oxygen atoms have to choose to which material they bond to. Due to the preferential sputtering of oxygen [MHS86], the target surface is always oxygen deficient and this requirement

is likely to be fulfilled. The formation of ZrO_2 and HfO_2 is then favored in comparison to TiO_2 .

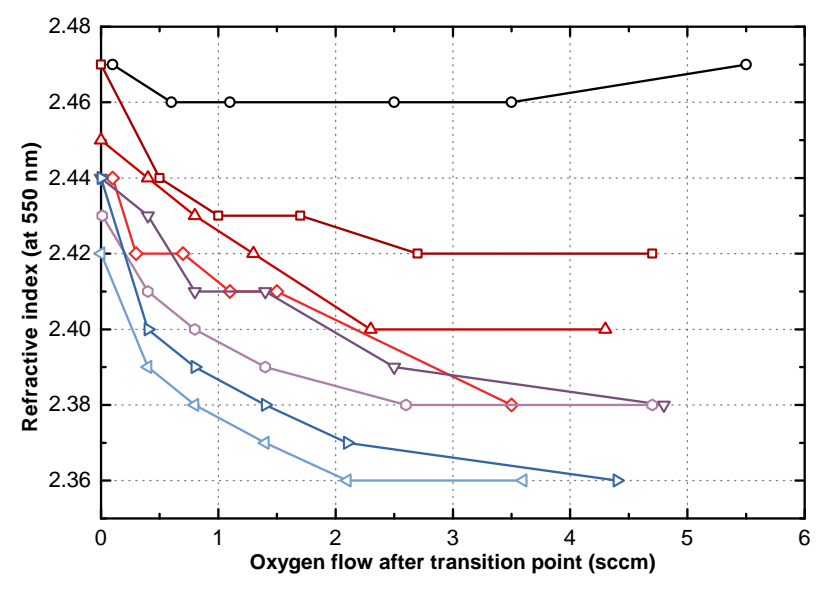
Upon doping of TiO_2 with Hf this leads to the formation of TiO_{2-x} suboxides and by that a more metallic target surface, a lower target voltage and consequently a higher sputter yield amplification of Ti [KDM⁺08] compared to other heavy dopants, like W and Ta.

6.3 Refractive index evolution upon doping

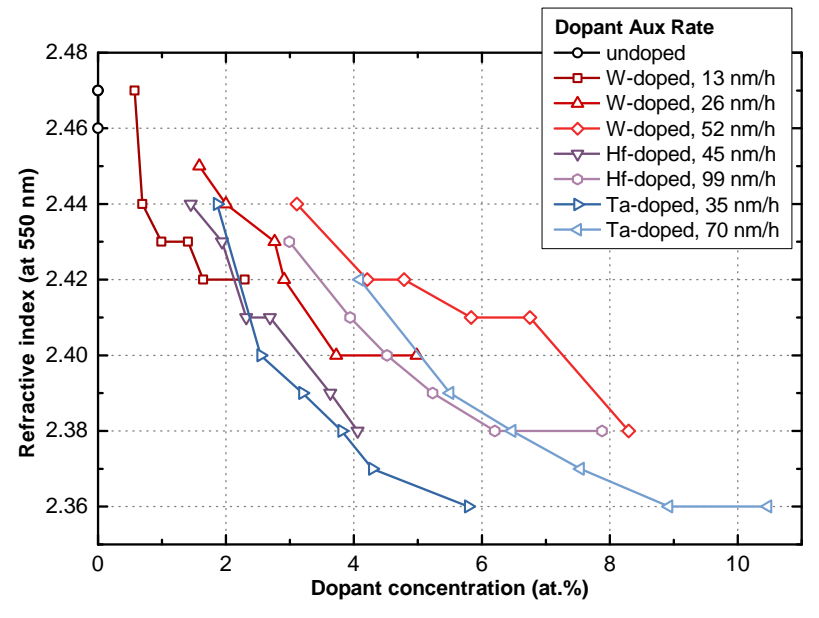
So far, the influence of heavy dopants on the sputtering process of TiO_2 was only analyzed with respect to the change in deposition rate. For industrial applications, however, it is obviously necessary to maintain the unique properties, especially the high refractive index, of TiO_2 .

The evolution of the refractive index of TiO_2 upon doping with Hf, Ta and W can be seen in Fig. 6.7. Without doping the refractive index of TiO_2 is independent of the O_2 flow after the transition point and has a value of 2.46-2.47. Upon doping with W the refractive index decreases with increasing O_2 flow, meaning that a higher dopant deposition rate results in a larger decrease of the refractive index. For a dopant deposition rate of 13 nm/h the refractive index at the transition point is unchanged and decreases only slightly to a value of 2.42 at an O_2 flow of 4.7 sccm after the transition point. For dopant deposition rates of 26 nm/h and 52 nm/h, the index at the transition point is slightly decreased to values of 2.45 and 2.44 and decreases further to values of 2.4 and 2.38 at 4.3 sccm and 3.5 sccm after the transition point, respectively.

For doping with Hf and Ta the results are similar to those for doping with W. At the transition point the refractive index is only slightly lower than for the undoped process, but with increasing O_2 flow the refractive index is lowered significantly. Doping with Ta decreases the refractive index at the transition point from 2.48 to 2.44 for a dopant deposition rate of $35\,\mathrm{nm/h}$ and to 2.42 for a dopant deposition rate of $70\,\mathrm{nm/h}$, wheras a dopant deposition rate of $45\,\mathrm{nm/h}$ and $99\,\mathrm{nm/h}$ lowers the refractive index to 2.44 and 2.43 at the transition point for doping with Hf, respectively. In the case of doping with Ta, increasing the O_2 flows to $4.4\,\mathrm{sccm}$ and $3.6\,\mathrm{sccm}$ after the transition point for a dopant deposition rate of $35\,\mathrm{nm/h}$ and $70\,\mathrm{nm/h}$, respectively, results in values of $2.36\,\mathrm{for}$ the refractive index in both cases. Hf doping lowers the refractive index at high O_2 flows a to a lesser extent than Ta, resulting in values of $2.38\,\mathrm{for}$ both dopant deposition rates of $45\,\mathrm{nm/h}$ at $4.8\,\mathrm{sccm}$ after the transition point and $99\,\mathrm{nm/h}$ at $4.7\,\mathrm{sccm}$ after the transition point.



a | Refractive index of TiO_2 upon heavy element doping as a function of the O_2 flow after the transition point. The legend is included in Fig. 6.7b.



 ${\bf b}$ | Refractive index of TiO $_2$ upon heavy element doping as a function of the dopant concentration

Figure 6.7 | Refractive index evolution of TiO_2 upon doping with heavy elements. Without doping, the refractive index of TiO_2 is independent of the O_2 flow after the transition point. Upon doping with Hf, Ta or W, the refractive index at the transition point is slightly lowered and decreases significantly with increasing O_2 flow (a). There is a clear correlation between the dopant concentration and the decrease in refractive index. Nevertheless, this correlation is only valid within a deposition series with a constant dopant deposition rate. At the same dopant concentration the O_2 flow is the parameter determining the refractive index.

As usual for reactive serial co-sputtering, the dopant concentration is linked to the O_2 flow. Hence, if the dopant concentration at a certain O_2 flow is known, the refractive index can be plotted as a function of the dopant concentration. From Fig. 6.7b it can be seen that there is only a correlation between the dopant concentration and the decrease in the refractive index within one series at a constant dopant deposition rate, but this correlation is lost upon switching between the series. If the dopant deposition rate is changed, the same dopant concentration, achieved by using different O_2 flows, results in different refractive indexes. A W concentration of 3.1 at.% for example results in a refractive index of 2.44 for a dopant deposition rate of 52 nm/h, whereas the same concentration results only in a refractive index of about 2.41 for the lower dopant deposition rate of 26 nm/h.

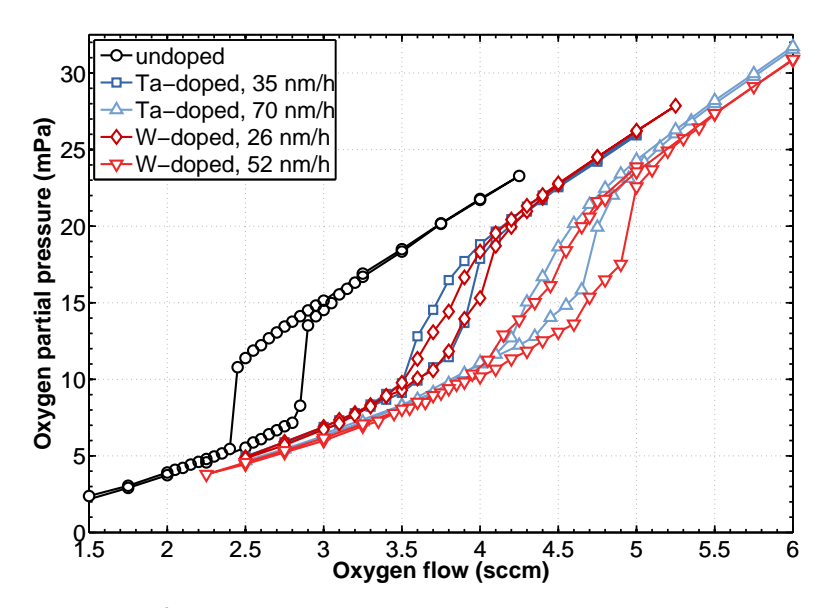
Looking at these results from another point of view, the observed correlation between dopant concentration, O_2 flow and refractive index implies that changing the dopant deposition rate results only in a minor change of the refractive index, as long as the O_2 flow is kept as low as possible. For the refractive index the O_2 flow is the determining factor, in contrast to the previously shown sputter yield amplification, where the dopant concentration is most important.

In summary, the highest refractive indexes are achieved next to the transition point. For industrial applications this is ideal as rates and sputter yield amplification are maximal at this point giving a clear concept to high rate, high index TiO₂ thin films.

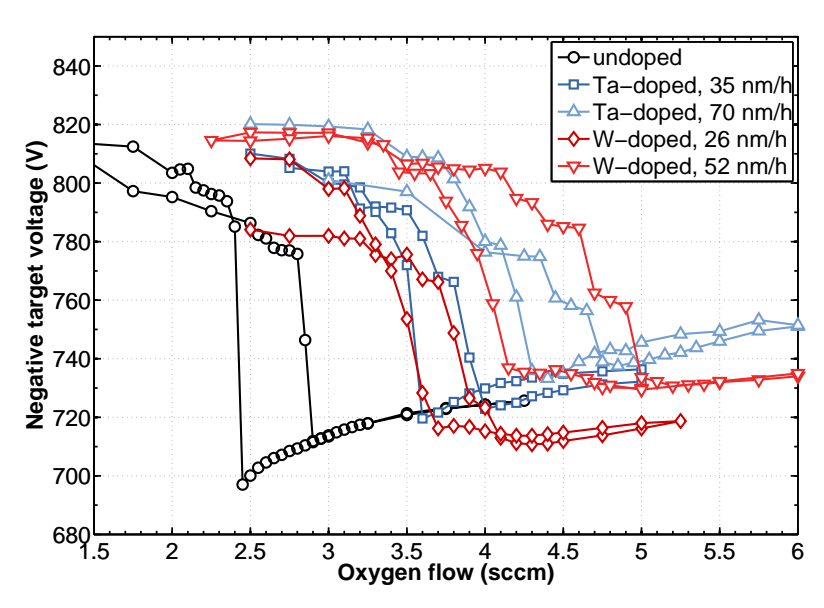
6.4 Sputter yield amplification using HiPIMS

Additionally to the sputter yield amplification experiments presented so far, the sputter yield amplification effect was also analyzed for HiPIMS processes (see Sect. 3.4) in this work. The deposition rate in HiPIMS is generally lower than in a DC process, by use of the same power [HLB+06, ASMW06], due to a higher ionization [GAH01, KDH06] and self sputtering [Chr05]. Consequently, increasing the deposition rate by sputter yield amplification in HiPIMS is of great interest.

For the investigation of the sputter yield amplification effect in HiPIMS, two heavy dopants, namely Ta and W, were chosen. Hysteresis curves of an undoped process and processes doped with different auxiliary rates were recorded to investigate the influence of the dopant on the process behavior and are plotted in Fig. 6.8. Due to the generally lower deposition rate in HiPIMS, the transition point of the undoped process is located at lower flows compared to the transition point of a DC process (see Fig. 6.5). Using HiPIMS, the hysteresis curves of the doped processes have a different shape compared to the undoped process. Especially in the partial pressure hysteresis curve (Fig. 6.8a), the transition from metal to oxide



a O₂ partial pressure hysteresis of HiPIMS sputtered TiO₂.



b | Target voltage hysteresis of HiPIMS sputtered TiO₂.

Figure 6.8 | **O₂** partial pressure and voltage hysteresis of HiPIMS sputtered TiO₂. The undoped target shows a sharp transition between oxide and metal mode for the partial pressure (a) and negative target voltage hysteresis (b). In contrast, doping with W or Ta leads to a smooth transition between the two modes. Upon doping, working points in the transition regime can be accessed without the need for fast feedback loops.

mode and vice versa is much smoother; there is no sharp transition between the two modes. Nevertheless, the transition points of the doped processes can be detected by looking at the voltage hysteresis curves in Fig. 6.8b, where the transition is more distinct.

The smooth transition of the doped processes allows the stabilization of the O₂ partial pressure in the transition regime without the need for a fast feedback loop. In doing so, substoichiometric films can easily be deposited. This might be interesting for transparent conductive oxides (TCO) [Gra93, HOO+02, SRW+08, SDG+12], especially for TiO₂:Nb and TiO₂:Ta [GvD+07, YHK+09], which benefit from oxygen vacancies with respect to their conductance.

It should be noted that the negative target voltage in metal mode is larger than the voltage in oxide mode, which is reversed to a DC process. In a reactive DC process operated at a constant current, the voltage rises at the transition point from metal to oxide mode in order to compensate the reduced secondary electron emission yield of the compound formed at the target surface [DHM $^+$ 07]. In HiPIMS on the other hand, the rise of the O_2 partial pressure in oxide mode, which is due to a less pronounced getter effect, is accompanied by an increase in the population of oxygen ions (O_2^+ and O^+), which contribute to the target ion current [NMD $^+$ 12]. Additionally, the secondary electron emission is enhanced through potential emission [And11] as the ionization energies of O_2 , O and O0 are 12.6 eV, 13.6 eV and 15.8 eV [Lid97], respectively, whereas the work functions of Ti and TiO2 are between 4 eV and 4.5 eV [LL05]. Hence, the voltage in oxide mode of a HiPIMS process is lower than in metal mode.

Upon doping the hysteresis curves are shifted to higher O_2 flows, indicating a higher oxygen consumption. For the samples doped with 70 nm/h and 52 nm/h of Ta and W the transition point shifts from 2.45 sccm in case of the undoped process to 4.3 sccm and 4.15 sccm, respectively. This should be connected to a higher deposition rate, which could be verified by modeling the thickness using ellipsometry and UV-VIS-spectroscopy data. The calculated rates are plotted as a function of the O_2 flow after the transition point in Fig. 6.9. Again, data points were fitted using exponential functions (see Eq. 6.1) to extrapolate the sputter yield amplification factor to the transition point.

The deposition rate is significantly amplified upon doping with Ta or W, with a higher dopant deposition rate resulting in a higher amplification. Looking at the transition point the rate of undoped ${\rm TiO_2}$ is amplified from 0.34 nm/s to 0.68 nm/s and 0.98 nm/s for Ta auxiliary rates of 35 nm/h and 70 nm/h and to 0.75 nm/s and 1.20 nm/s for W auxiliary rates of 26 nm/h and 52 nm/h, respectively. As before, all rates decrease with increasing ${\rm O_2}$ flow, if the dopant deposition rate is kept constant.

By use of RBS measurements and the extrapolated curves in Fig. 6.9, the rate enhancement

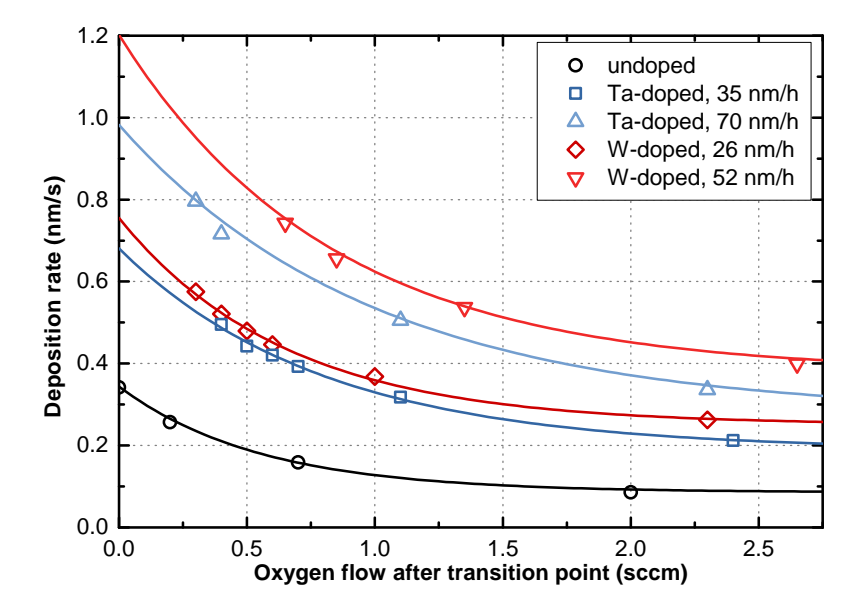


Figure 6.9 | Deposition rates of HiPIMS sputtered TiO_2 as a function of O_2 flow. The rates are plotted as a function of the O_2 flow after the transition point and decrease with increasing O_2 flow. Upon doping with Ta or W, the deposition rate is significantly amplified with a higher dopant deposition rate resulting in a higher amplification.

factor (Eq. 5.6) can be calculated as a function of the dopant concentration, which is the best way to quantify the sputter yield amplification (see Sect. 6.1). The calculated rate enhancement factors of the samples doped with 70 nm/h and 52 nm/h of Ta and W, respectively, are plotted in Fig. 6.10. Additionally the sputter yield amplification factor of a corresponding TiO_2 :W DC process with identical auxiliary rate is included to compare the sputter yield amplification of HiPIMS to DC.

The rate enhancement factors of both HiPIMS processes are higher than the enhancement factor of the DC process, for all dopant concentrations analyzed. Using W as a dopant the rate can be enormously amplified by a factor of up to 5, but even Ta-doping is able to increase the rate by a factor of up to 4.2, which is much higher than the amplification in a DC process, having a maximum of 3.7 using W as a dopant. Even more important are the rate enhancement factors at the lowest dopant concentration – at the transition point – where the total rates are maximal. Here, doping TiO_2 with W in HiPIMS shows a rate enhancement factor of 3.5 at 1.0 at.% of dopant concentration in the resulting film, being the most effective dopant. Doping with Ta in HiPIMS still results in a rate enhancement factor of 2.8 at 2.5 at.% in the resulting film, whereas doping with W in a DC process results in a rate enhancement factor of 2.1 at 2.9 at.% only.

The use of a HiPIMS discharge strengthens the sputter yield amplification caused by heavy

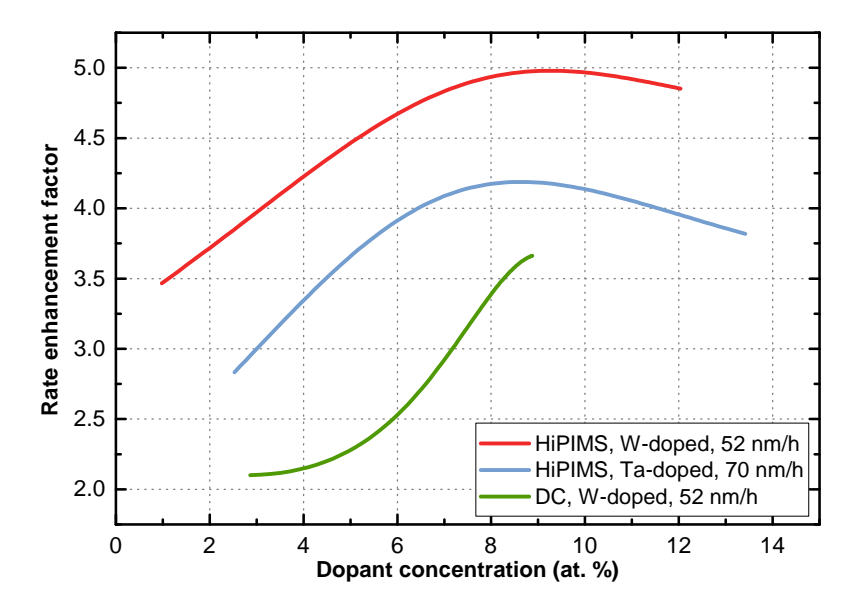


Figure 6.10 | Comparison of sputter yield amplification factors in DC and HiPIMS. The rate enhancement factors of both HiPIMS processes are higher than the enhancement factor of the DC process, for all dopant concentrations analyzed. By use of W as a dopant in a HiPIMS process the rate can be enormously amplified, but even doping with Ta is able to increase the rate significantly. The enhancement factor in HiPIMS at the transition point upon doping with W is as high as the maximum enhancement in DC at the highest dopant concentration. The amplification is significantly higher in a HiPIMS process.

dopants compared to DC. One of the major differences between HiPIMS and DC is the degree of ionization of the plasma [SAK10]. If the dopant is ionized in the plasma, this leads to an acceleration of the dopant ions towards the target, resulting in a deeper implantation depth and by that a more effective sputter yield amplification.

6.4.1 Implantation efficiency

To prove that the higher sputter yield amplification of TiO_2 using HiPIMS can be explained by a more effective implantation of the dopant due to an ionization of the dopant in the plasma, additional experiments were performed.

Upon doping with W, the target voltage increases. This effect can be used to analyze the W content during sputter cleaning of a previously W-doped Ti target [Aus11]. Here, the Ti target had been sputtered using a HiPIMS or DC discharge while being simultaneously coated with W from the auxiliary cathode. The sputter process was kept running until a steady state was reached, meaning no drift in process parameters (e.g. partial pressure and voltage) could be observed. Subsequently, sputtering was stopped and the target was sputter cleaned using

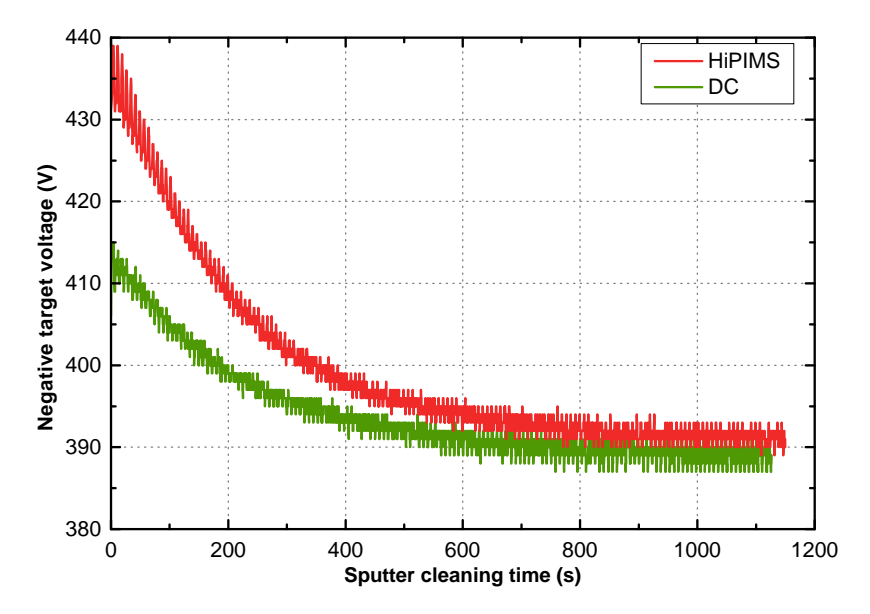


Figure 6.11 | **Voltage evolution upon sputter cleaning after using HiPIMS and DC.** A Ti target was sputter cleaned using a low DC current. Previously to the cleaning, the target had been W-doped by serial co-sputtering. The primary discharge used to implant the dopant had either been performed using HiPIMS or DC. Data taken from [Wag11].

a low DC discharge current and a high O_2 flow (250 mA, 7 sccm) to ensure a slow change in target voltage, which can easily be recorded. The resulting discharge voltages as a function of time can be seen in Fig. 6.11. The voltage drop during sputter cleaning after the HiPIMS sputtering is about 40 V, whereas the voltage drop after DC sputtering is only about 20 V. Furthermore, the time needed to clean the target after HiPIMS sputtering is longer. Both, a longer cleaning time and a higher voltage drop, indicate a much higher implantation depth in the case of HiPIMS.

In order to investigate if the origin of the thicker implantation layer is due to an ionization of the dopant, optical emission spectroscopy was performed. Emission spectra were recorded for a Ti target sputtered in Ar or Ar/O_2 atmosphere using various amounts of W doping with either a DC or a HiPIMS discharge applied. In order to show ionization of W, the spectral range from 238 nm to 252 nm was chosen including several W II lines (see Tab. C.1 in Appx. C).

The results of the optical emission spectroscopy are summarized in Fig. 6.12. The top four spectra show the emission of a TiO_2 plasma in a HiPIMS discharge with increasing doping concentration (black and purple lines, from top to bottom). Three Ti II lines at 244.02 nm, 245.04 nm and 251.74 nm [RVC75, PTP01] and an Ar II line at 251.56 nm [WAC⁺95] can be identified in all four spectra, underlining the high degree of ionization of all atoms in HiPIMS.

The W II lines at 239.71 nm, 246.65 nm, 247.78 nm, 248.92 nm, 249.75 nm and 249.97 nm [EKM00] become stronger with increasing auxiliary power as the intensity increases with the W content in the plasma, proving the W ionization in the HiPIMS discharge. Even in the presence of oxygen, shown in the fifth spectrum of Fig. 6.12 (red line) these lines remain visible showing that the ionization of W also occurs in Ar/O_2 atmosphere. In contrast to this, no emission lines of W⁺ are found in a DC discharge (Fig. 6.12, bottom spectrum, green line), even at a very high W concentration due to a high auxiliary power of 400 W. In a DC process, the degree of ionization is very low [CB00], even the emissions of Ar^+ and Ti^+ are not visible, and the emitted spectrum is dominated by the emission of neutral atoms (see Fig. 4.4).

The proof of W ionization in a TiO_2 :W plasma explains the higher sputter yield amplification in HiPIMS compared to DC. The W atoms get ionized in the HiPIMS plasma and are accelerated back to the target, resulting in a deep implantation in the Ti target, where they can act as recoil centers more efficiently.

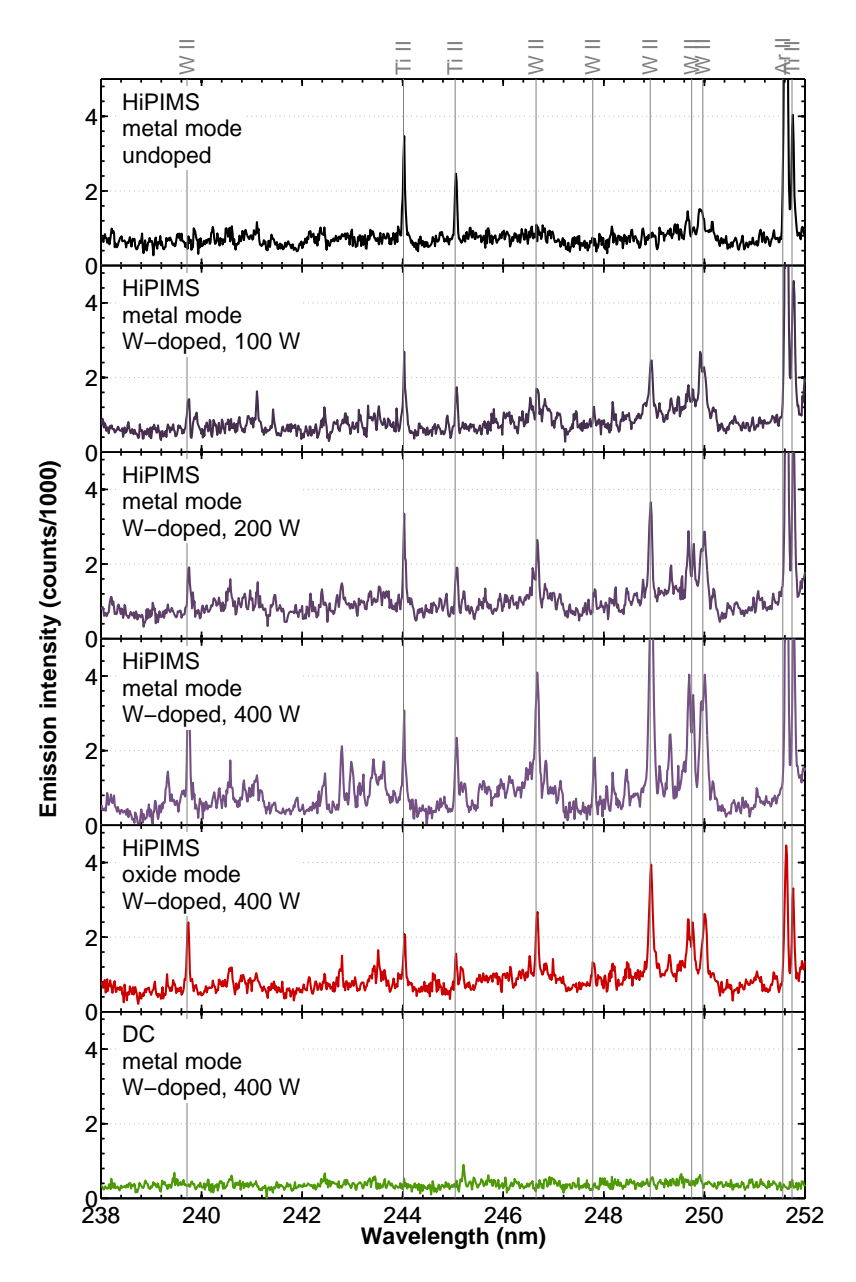


Figure 6.12 | **Evolution of optical emission spectra of HiPIMS and DC sputtered Ti:W.** The top four spectra show that emission lines of ionized W in Ar atmosphere become stronger with increasing auxiliary power as the intensity increases with the increasing W content in the plasma (from top to bottom, black and purple lines). Several strong W II lines can be identified showing a clear proof of W ionization in the HiPIMS discharge. The same is true in the presence of oxygen (red line). In contrast to this, no emission lines of W⁺ are found in a DC discharge (green line), even for very high W concentrations (400 W). This result is an explanation for the higher sputter yield amplification in HiPIMS. The W atoms get ionized in the HiPIMS plasma and are accelerated back to the target, resulting in a deep implantation within the Ti target.

Influence of dopants on structure and phase transformation of TiO₂

In Chap. 6, different dopants have been analyzed with respect to their capability to increase the deposition rate of TiO_2 . As outlined in Sect. 2.2.2, dopants can also be used to modify the crystallization behavior of TiO_2 . It might even be possible, by use of a well chosen dopant, to modify the crystallization behavior in such a way that sputtering of a thermally stable TiO_2 thin film in either amorphous, anatase or rutile phase could be possible.

Most literature data on the phase transformation of TiO_2 are gathered using powders starting in the anatase phase [SP65, Mac75, HS11]. In contrast, sputtered thin films are often amorphous and thermodynamically far away from equilibrium [DKY+09], making the transformation from amorphous to either anatase or rutile equally important. In this chapter, the influence of several dopants on the phase formation and phase transformation during annealing is analyzed using serial co-sputtered TiO_2 thin films.

7.1 Dopants

Ten dopants, namely V, Cr, Mn, Cu, Zr, Mo, Sn, Hf, Ta and W, were investigated with respect to their influence on the phase transformation and crystallization behavior of TiO₂. Doping of TiO₂ with Hf, Ta and W has already been shown to increase the deposition rate and therefore their influence on the crystallization behavior is of great interest. Additionally, Hanaor and Sorrell predict that these three elements inhibit the phase transformation from anatase to rutile [HS11], allowing for the deposition of thermally stable TiO₂. Two other elements

inhibiting the phase transformation from anatase to rutile are Zr and Mo, from which Zr has already been shown to inhibit the transformation experimentally [HNO⁺03], whereas Mo has been predicted to inhibit the phase transformation theoretically [HS11].

Inhibiting the phase transformation is one way to produce a thermally stable TiO₂ film. Another way is the deposition of a pure thermally stable rutile film. Unfortunately, a direct deposition of thermally stable rutile films is not possible using a standard DC sputter process [AKW10]. By adding a phase transition-promoting dopant it might be possible to initialize the formation of rutile already upon film growth. Consequently, V, Cr, Mn, Cu and Sn, which have been shown to promote the anatase to rutile transformation (ART) [ZR02, Kar03, Mac75, SP65, KFN+07], were investigated as well.

For each dopant, samples were deposited using different O_2 flows after the transition point (see Sect. 6.1) at a constant auxiliary power (dopant deposition rate). V, Zr, Hf, Ta and W were sputtered onto the rotating Ti target using 50 W and aperture L (see Sect. 3.1.1), whereas Cr, Mo and Sn were sputtered onto the rotating Ti target using 25 W, 40 W and 30 W, respectively. For the deposition of Mn and Cu a smaller aperture (M) and powers of 50 W and 25 W were used, respectively. The deposition rates of Cr, Mo, Mn, Cu and Sn were lowered as these materials show significantly higher sputter yields [SCGG05]. Deposition times from the doped Ti target onto glass substrates were adjusted to sputter films with thicknesses of about 100 nm. For each combination of dopant and O_2 flow three identical samples were deposited, from which one was measured by ellipsometry and UV-VIS spectroscopy to validate the thickness. Afterwards, the remaining two were annealed to either 300 °C for 1 h or 700 °C for 10 min.

The stoichiometry of the deposited thin films was investigated using either RBS or EDX. EDX had to be chosen for V, Cr and Mn, as the characteristic peaks of Ti, V, Cr and Mn overlap in the RBS spectrum due to their similar masses of $47.9\,u$, $50.9\,u$, $52.0\,u$ and $55.0\,u$, respectively, whereas both methods are suitable for the other elements. Unfortunately, the characteristic peaks of Ti and V overlap in the EDX spectrum as well and therefore the determined concentrations of V have to be used with caution. For the remaining elements, the concentrations of Cu, Zr, Mo, Hf, Ta and W were investigated by RBS, whereas EDX was utilized for the concentration of Sn. The determined dopant concentrations are plotted in Fig. $7.1\,a$ as a function of the O_2 flow after the transition point. With increasing O_2 flow the deposition rate of Ti O_2 decreases, but as the deposition rate of the dopant utilized was kept constant, the dopant concentration in the resulting films increases (see Sect. 6.1). All determined concentrations are in a range of $0.42\,a$ t.% (Zr) to $1.86\,a$ t.% (Ta) at the transition point and increase to values between $1.78\,a$ t.% (V) and $6.08\,a$ t.% (Sn) at higher O_2 flows. The measured V concentration decreases at the highest O_2 flow, which is not reasonable. This deviation is attributed to the

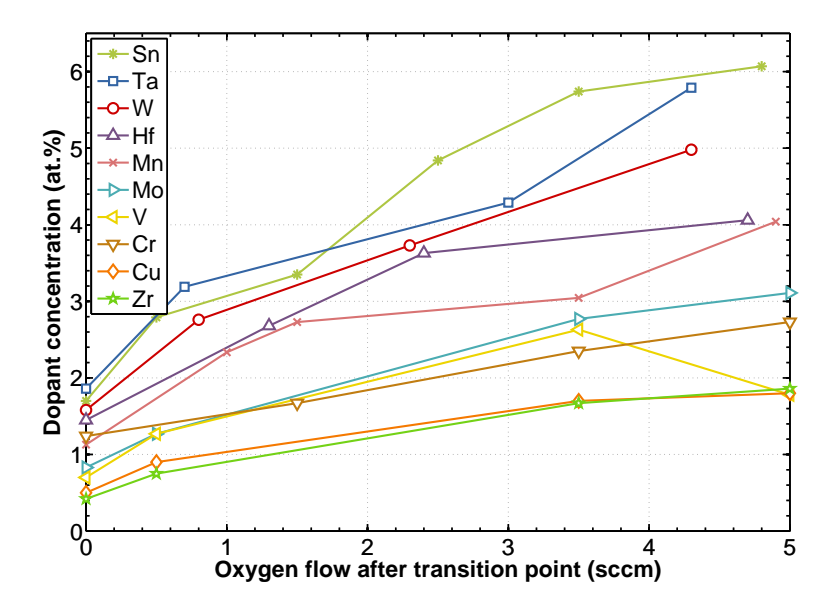


Figure 7.1 | Dopant concentrations of serial co-sputtered TiO_2 thin films. With increasing O_2 flow the deposition rate of TiO_2 decreases, but since the deposition rate of the dopant utilized was kept constant, the dopant concentration in the resulting films increases (see Sect. 6.1).

overlapping peaks in the EDX spectrum, which complicated a calculation of the stoichiometry. The determined concentration of V can either be too low for this sample or the other measurements of the samples sputtered at lower O_2 flows may be too high. The concentrations of Cu and Zr are the lowest within this study, showing less than 2 at.% for all O_2 flows. Nevertheless, their amount might already be sufficient to alter the phase transformation behavior, because influences of dopants have already been found for concentrations lower than 0.2 at.%, for example in the case of Sn-doping [MRS04]. Still, higher concentrations in the order of several percent have also been reported to have a significant influence [Mac75], allowing a wide range of possible concentrations.

7.2 Structural properties of as-deposited samples

There are several publications reporting either as-deposited crystalline [MTDR00, HUF+07, HYH+08, AKW10, MS11, AYR+12] or X-ray amorphous TiO₂ films [TPD+02, MS11, GRCVV11], depending on the sputter parameters utilized. Mráz et al. investigated the structure evolution of RF and DC sputtered TiO₂ thin films upon changing the total pressure and concluded that the phase formation is linked to the ratio between the ion energy flux to the growing film and the deposition flux [MS11]. Additionally, Amin et al. showed that the structure forma-

tion of anatase and rutile upon film growth is heavily dependent on the O_2 flow due to the corresponding energetic bombardment with high energy oxygen ions [AKW10].

The formation of O^- ions, which are accelerated towards the growing film due to the negative target potential, depend on the difference between ionization potential I_{Me} of the metal and the electron affinity of oxygen E_O^{ea} [Cuo78]. The probability of the formation of O^- ions due to the transfer of an electron from the metal atom to an oxygen atom can hence be written as

$$I_{\text{Me}} - E_{\text{O}}^{\text{ea}}.\tag{7.1}$$

Ngaruiya et al. stated that metal oxides of group 5 and 6 elements tend to be amorphous upon magnetron sputtering due to the damage caused by high energy O⁻ ions accelerated by a high target voltage. The target voltage shows a strong negative correlation to the number of negative oxygen ions, whose formation is most pronounced for group 4 elements and decreases for elements of higher groups. Hence, group 5 and 6 elements show less, but more energetic bombardment [NKMW04], which suppresses crystallization. In contrast to group 5 and 6 metal oxides, the bombardment with energetic O⁻ ions deteriorates the anatase, but promotes the rutile phase of TiO₂ [AKW10]. Accordingly, doping of TiO₂ with group 5 and 6 elements might promote the rutile phase upon film growth due to a higher bombardment with O⁻ ions. Zr and Hf on the other hand should lower the energy of the oxygen ions and, consequently, lead to anatase films. These conclusions, however, are only based on ion bombardment and do not consider the influence of the dopant in the resulting film itself.

To investigate the structure of the deposited films, grazing incidence X-ray diffraction (see Sect. 4.1.2) experiments were performed. The resulting diffractograms for as-deposited (a/d) films are plotted in Fig. 7.2 and Fig. 7.3 for dopants inhibiting and promoting the anatase to rutile transformation, respectively. All films are X-ray amorphous, no peaks can be detected in the diffractograms, independent of dopant and O_2 flow.

Films investigated within this work were sputtered using similar process conditions (total pressure, O_2 flow, target-substrate distance) as those, which have been used by Amin et al. [AKW10]. These conditions are likely to result in crystalline films, but still the as-deposited films within this work exhibit no crystalline structure. Films showing different growth behaviors in different publications, normally have been sputtered using different deposition chambers and target sizes, which is here the case, too. The geometry of the chamber as well as the fact that for the samples produced within this work a rotating primary target was utilized are therefore most likely to alter the process window for as-deposited crystalline films.

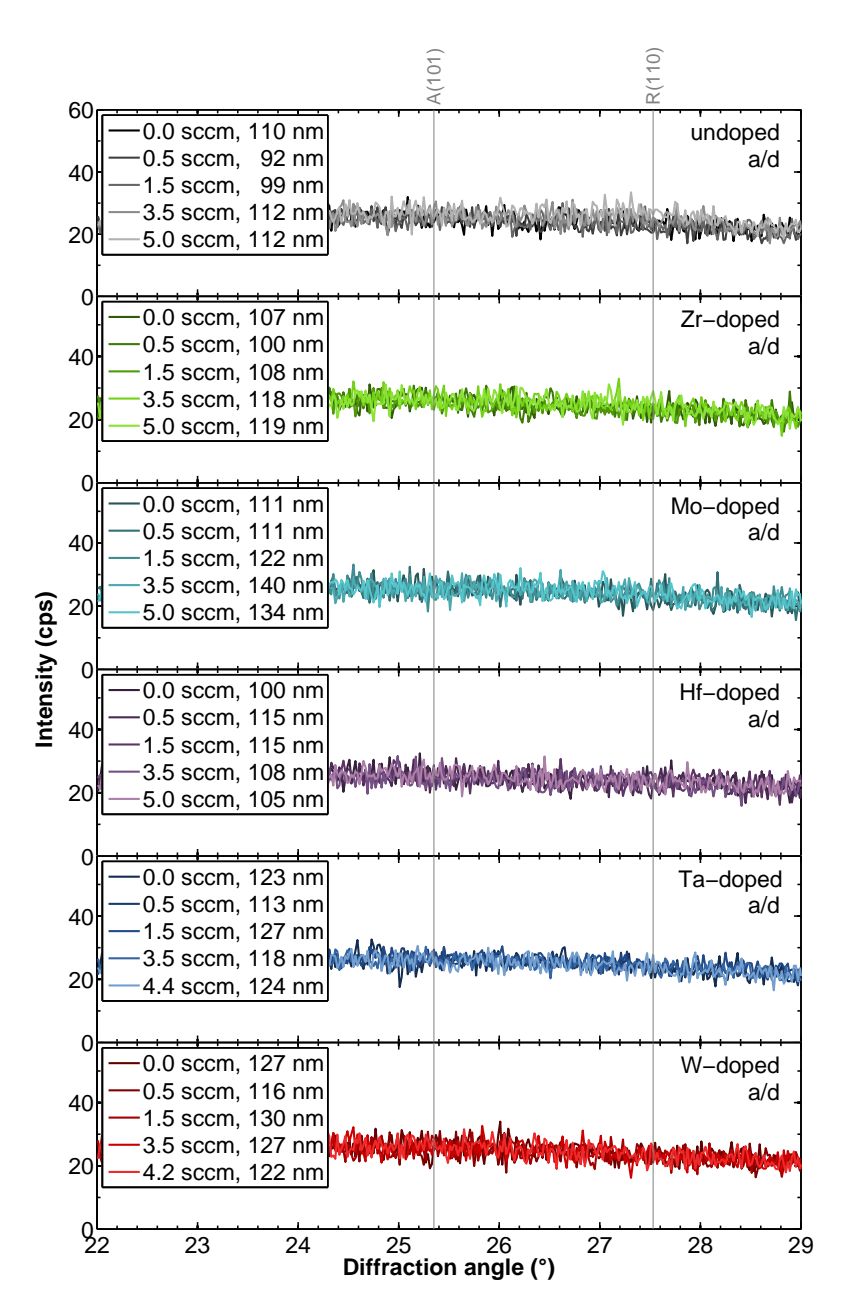


Figure 7.2 | GI-XRD measurements of as-deposited TiO_2 with ART-inhibiting dopants. As-deposited (a/d) undoped and with anatase to rutile transformation-inhibiting elements doped TiO_2 thin films sputtered at different O_2 flows after the transition point were measured by grazing incidence X-ray diffraction. All measurements are normalized to a background of 25 cps. The gray lines indicate the positions of the anatase (101) and rutile (110) peak. All films are X-ray amorphous, no peaks of either anatase or rutile can be detected.

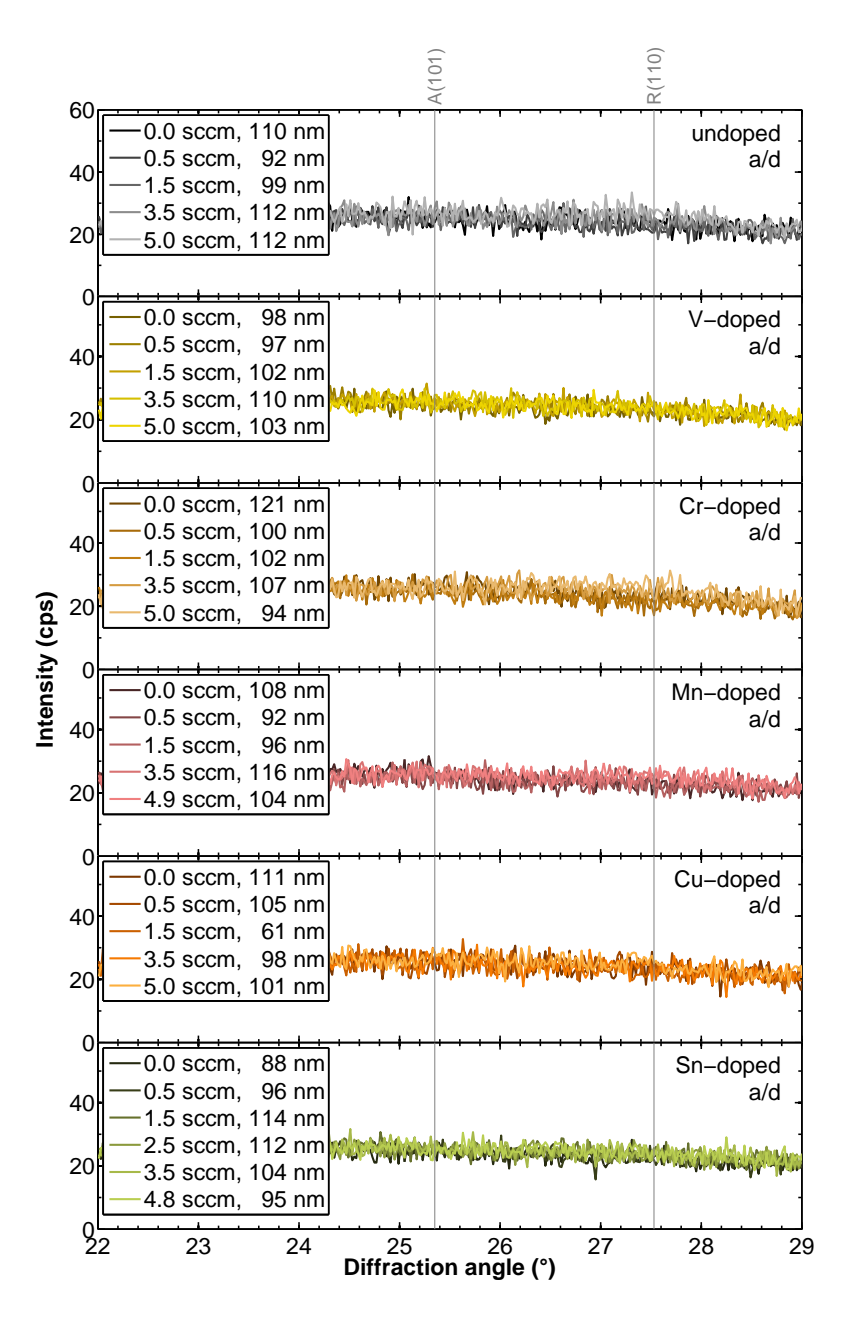


Figure 7.3 | GI-XRD measurements of as-deposited TiO_2 with ART-promoting dopants. As-deposited (a/d) undoped and with anatase to rutile transformation-promoting elements doped TiO_2 thin films sputtered at different O_2 flows after the transition point were measured by grazing incidence X-ray diffraction. All measurements are normalized to a background of 25 cps. The gray lines indicate the positions of the anatase (101) and rutile (110) peak. All films are X-ray amorphous, no peaks of either anatase or rutile can be detected.

It might be interesting to investigate the influence of the utilized dopants on the structure formation of films which exhibit an as-deposited crystalline structure, but unfortunately this investigation is beyond the scope of this work and, consequently, in the following the focus is on the structure evolution of as-deposited X-ray amorphous films upon annealing.

7.3 Phase transformation upon annealing

To analyze the influence of dopants on the phase transformation of as-deposited X-ray amorphous samples, grazing incidence X-ray diffraction measurements were performed for samples annealed at 300 °C and 700 °C with the anatase to rutile transformation-inhibiting and -promoting dopants. The classification into phase transformation inhibitors and promoters by Hanaor and Sorrell is based on the influence on the rigidity of the lattice against the creation or annihilation of oxygen vacancies as well as interstitials or substitutions with large ionic radii. If the lattice is weakened this allows for a rearrangement of the atoms to transform into rutile [HS11]. For an amorphous film, however, no lattice is available which could be weakened or strengthened and the influence of dopants on the formation and growth of grains can be investigated.

7.3.1 Anatase to rutile transformation-inhibiting dopants

The X-ray diffractograms plotted in Fig. 7.4 show the undoped samples as well as the samples doped with phase transformation-inhibiting elements, both of which were annealed at $300\,^{\circ}$ C. From the diffractograms, the heights of the anatase as well as the heights of the rutile peaks were extracted, which are plotted in Fig. 7.5 as a function of the O_2 flow after the transition point. Upon annealing of undoped TiO_2 at $300\,^{\circ}$ C, a phase transition from amorphous to anatase occurs. The height of the anatase peak is thereby connected to the O_2 flow during deposition. At the transition point the anatase peak of the undoped sample has a height of about 200 cps which increases to about 250 cps at 1.5 sccm after the transition point. Increasing the O_2 flow further leads to lower peaks, which decrease down to about 130 cps for the sample sputtered at $5.0\,\text{sccm}$ O_2 flow after the transition point. For the samples sputtered at high O_2 flows a broad rutile peak can be noticed, but the peak height is only $40\,\text{cps}$, hardly visible within the background of $25\,\text{cps}$.

None of the samples could be distinguished by their diffractograms before annealing (see Fig. 7.2) but tend to form different phases upon annealing. This behavior can be explained by a different bombardment with high energy ions during film growth. As the phase formation of TiO₂ is linked to the ratio between the ion energy flux to the growing film and the

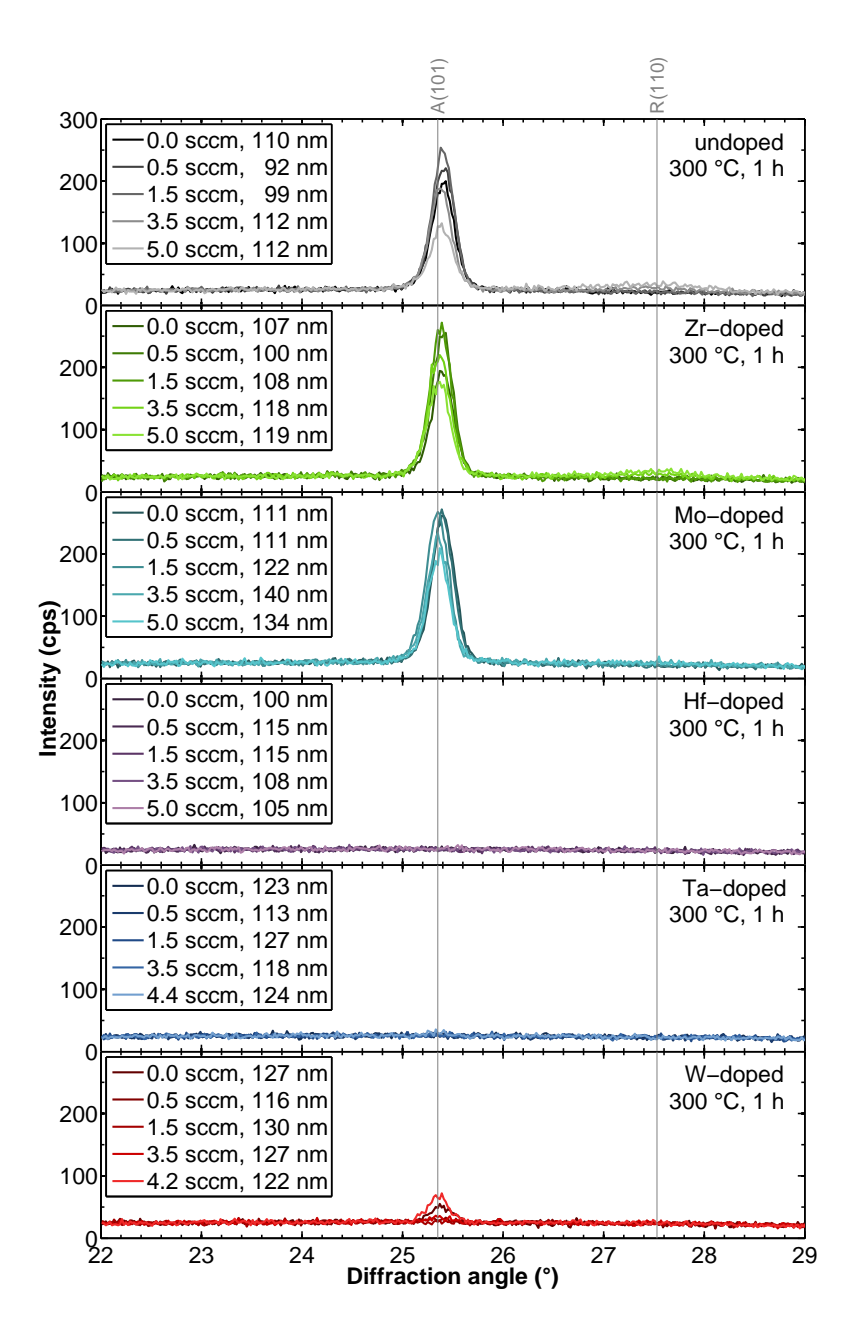


Figure 7.4 | GI-XRD measurements of TiO₂ ann. at 300 °C with ART-inhibiting dopants. Undoped and with anatase to rutile transformation-inhibiting elements doped TiO₂ thin films sputtered at different O₂ flows after the transition point were annealed at 300 °C for 1 h and measured by grazing incidence X-ray diffraction. All measurements are normalized to a background of 25 cps. The gray lines indicate the positions of the anatase (101) and rutile (110) peak. The undoped, Zr-doped and Mo-doped films show a pronounced peak of the anatase phase. Hf and Ta prevent any crystallization in the samples. W suppresses the crystallization as well, however, a small anatase peak can be found for some W-doped samples. Extracted peak heights are plotted in Fig. 7.5.

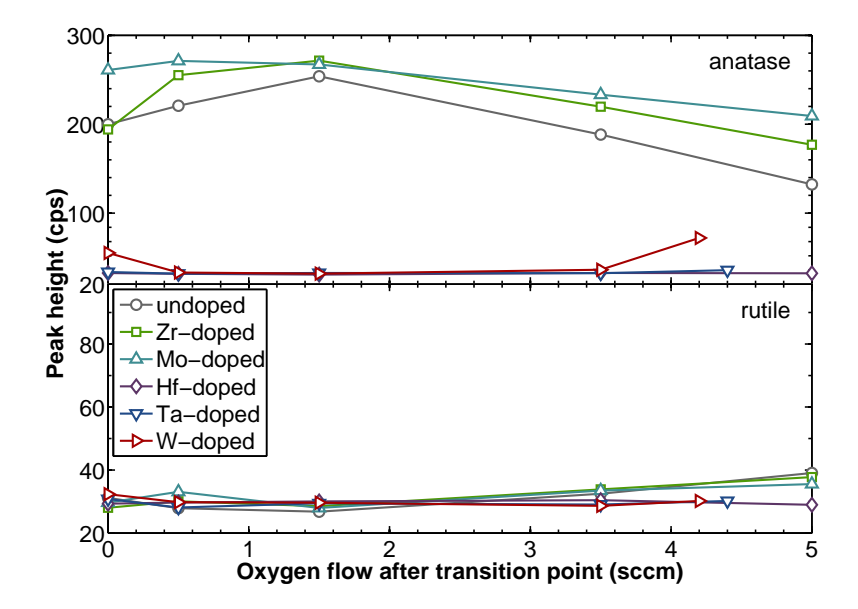


Figure 7.5 | Peak heights of TiO_2 annealed at 300 °C with ART-inhibiting dopants. The height of the anatase (top) and rutile peaks (bottom), extracted from Fig. 7.4, are plotted as a function of the O_2 flow after the transition point with respect to the utilized dopants.

deposition flux [MS11], a change in O_2 flow causes a change in deposition rate and O_2 partial pressure and by that a change of this ratio. At about 1.5 sccm after the transition point, this ratio is ideal for the formation of anatase grains, as the peak height is at its maximum for this flow. At higher O_2 flows, the bombardment with high energetic ions leads to a formation of rutile grains and a deterioration of anatase grains. However, these grains are too small to cause constructive interference in X-ray diffraction and hence can not be detected in the as-deposited film. Upon annealing these grains grow to a detectable size.

Doping of TiO_2 with Zr and Mo leads to a slightly increased anatase peak compared to undoped TiO_2 in the diffractograms after annealing at 300 °C. The samples doped with Mo sputtered at high O_2 flows are about 20 nm to 30 nm thicker than the undoped and Zr-doped samples. Nevertheless, the higher peak is attributed to the influence of the dopant, since the increased height is also found for the samples sputtered at lower O_2 flows, which do not show an increased thickness. For Zr and Mo, the decrease and increase of the anatase peak height is similar to that of the undoped films as well as the evolution of the hardly visible rutile peak (see Fig. 7.4 and Fig. 7.5). However, the rutile peak is much smaller for the samples doped with Mo, whereas the Zr-doped samples show peaks as broad and high as the undoped ones. Zr is an inhibitor of the anatase to rutile transformation [HNO+03] and Mo has been predicted to be one [HS11]. The inhibiting character of Zr is due to its ionic radius of 0.86 Å in sixfold coordination, which constrains the anatase lattice and thereby inhibits a

Table 7.1 | Comparison of ionic radii in sixfold coordination of ART-inhibiting dopants.

All phase inhibiting dopants used within this work have a larger radius than Ti upon substitution with a valence of 4. From these Zr and Hf are the largest having an up to 15% larger radius compared to Ti. Mo, Ta and W are more likely to substitute with a valence greater than 4, leading to the annihilation of oxygen vacancies and a decrease in radius. Nevertheless, Zr and Mo promote a formation of anatase at 300 °C, whereas Hf, Ta and W inhibit it. Data taken from [Sha76].

Dopant	Ti	Zr	Mo	Hf	Ta	W
Radius Me ⁴⁺ (Å) Radius Me ⁵⁺ (Å) Radius Me ⁶⁺ (Å)	0.75	0.86	0.79 0.75 0.73	0.85	0.82 0.78	0.80 0.76 0.74

phase transformation from anatase to rutile [Sha76, HS11], whereas Mo has a valence of 6 and therefore is likely to decrease the number of oxygen vacancies, which strengthens the oxygen sub-lattice. A dopant with a large radius, like Zr, might also inhibit the transformation from amorphous to anatase, but this can not be observed in Fig. 7.4. The fact that the rutile peak is smaller for the Mo-doped sample suggests that the valence of the dopant is more important for the suppression of the rutile phase than the ionic radius. On the other hand, Zr shows one of the lowest concentrations among all dopants investigated and the less pronounced influence might also be connected to an insufficient concentration.

In contrast to the samples doped with Zr and Mo, which crystallize into anatase, the samples doped with Hf and Ta do not show any crystallization. The same is true for the samples doped with W sputtered at $0.5 \, \text{sccm}$, $1.5 \, \text{sccm}$ and $3.5 \, \text{sccm}$ after the transition point, whereas the samples sputtered at $0.0 \, \text{sccm}$ and $4.2 \, \text{sccm}$ after the transition point show a small contribution of a crystalline anatase phase in their diffractograms (see Fig. 7.4 and Fig. 7.5). As Hf, Ta and W have a valence of $n \geq 4$ and ionic radii close to or larger than the radius of Ti, depending on their actual valence in the lattice (see Tab. 7.1), they should act like Zr and Mo. In consequence, as the formation of the anatase phase is suppressed by Hf, Ta and W, this must be due to other properties of the dopants or differences in the deposition processes. The concentration of Mo and Zr is lower than the concentration of Hf, Ta and W (see Fig. 7.1), but as the crystallization of the anatase phase is actually enhanced by Mo and Zr, this is likely not to be the reason.

In Chap. 6, it has been shown that Hf, Ta and W increase the deposition rate of TiO_2 by at least 80% by the so called sputter yield amplification effect (SYA). Consequently, the ratio between the ion energy flux to the growing film and the deposition flux is reduced. In SYA, heavy atoms in the target act as recoil centers, which reflect the recoiled atoms towards the target surface [BBG⁺92] (see Sect. 3.3). If target atoms are recoiled, it is also very likely that

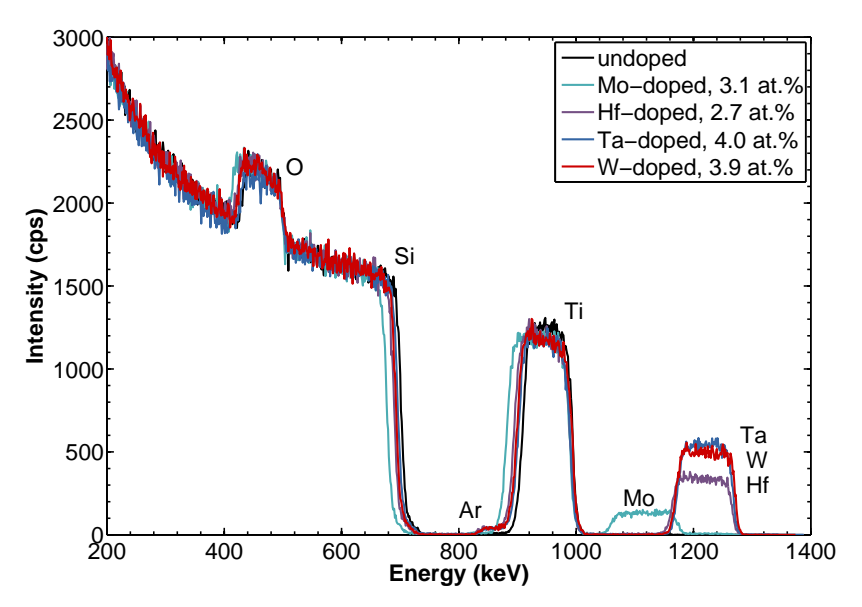
Ar atoms, which have been neutralized at the target surface from Ar⁺, are recoiled as well. The bombardment of the growing film with these Ar atoms could suppress a nucleation of anatase grains. Furthermore, Ar atoms which are incorporated in the growing film might lead to phase transformation-inhibiting Ar interstitials, due to their inertness, and hamper a crystallization.

In Fig. 7.6, RBS measurements (see Sect. 4.3.1) of TiO₂ films doped with Mo, Hf, Ta and W as well as an undoped reference are shown. The dopant concentrations were determined to 3.1 at.%, 2.7 at.%, 4.0 at.% and 3.9 at.% for doping with Mo, Hf, Ta and W, respectively. In Fig. 7.6a a small Ar peak can be seen on the left side of the Ti peak for some of the films. A magnification of this peak is shown in Fig. 7.6b for a better visibility of details. Upon doping with Hf, Ta and W the amount of Ar incorporated into the growing film is significantly increased to values about 4 at.% compared to less than 1 at.% in the undoped sample. In contrast, doping with Mo does not increase the Ar content in the film, even though the concentration of the dopant in the resulting film is higher than that of the Hf-doped film. This finding is a confirmation of the bombardment with Ar atoms of the growing film, induced by recoil of Ar⁺ ions at heavy dopant atoms in the target.

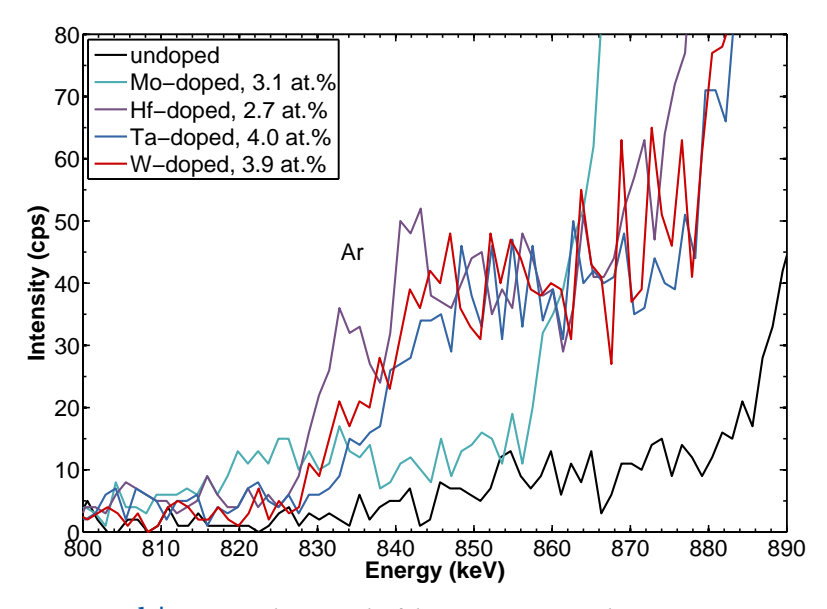
The anatase to rutile transformation-inhibiting dopants strengthen the anatase phase by reducing the number of oxygen vacancies and constraining the lattice [HS11]. These properties do not hinder the transformation from amorphous to anatase, they even accelerate it, as can be seen for Mo and Zr. If the dopants are heavy enough to provoke an Ar bombardment of the growing film, this bombardment suppresses a crystallization of the anatase phase due to the incorporation of Ar atoms in the resulting film, as can be seen for Hf and Ta. W provokes an Ar incorporation as well, which reduces the crystallization, but a weak crystallization remains. This can be explained due to the fact that W has the highest valence and the smallest radius of these dopants and hence promotes the anatase phase strong enough to allow the growth of some grains.

Additionally to the investigations of the annealing behavior at $300\,^{\circ}$ C, X-ray amorphous samples doped with phase transformation-inhibiting dopants were also annealed for $10\,\mathrm{min}$ at $700\,^{\circ}$ C and measured by grazing incidence X-ray diffraction, subsequently. The resulting diffractograms are plotted in Fig. 7.7 and the extracted peak heights of the anatase as well as the rutile peaks are plotted in Fig. 7.8.

Undoped films, which were sputtered using low O_2 flows, crystallize to anatase, whereas films sputtered using high O_2 flows crystallize to a mixture of anatase and rutile, during annealing at 700 °C. In comparison to the films annealed at 300 °C (see Fig. 7.4), the anatase phase is less pronounced for the films sputtered at low O_2 flows, which can be seen from



 ${\bf a} \mid {\rm RBS}$ measurements of ${\rm TiO_2}$ doped with Mo, Hf, Ta, and W as well as an undoped reference.



b Zoom on the Ar peak of the measurements shown in (a).

Figure 7.6 | **RBS measurements of TiO₂ with different dopants.** Upon doping with Hf, Ta and W the amount of Ar incorporated into the growing film is significantly increased. Without doping and upon doping with Mo, the Ar content is not increased. The heavy dopant atoms reflect Ar atoms, neutralized at the target surface from Ar⁺, which bombard the growing film and thus get incorporated as interstitials.

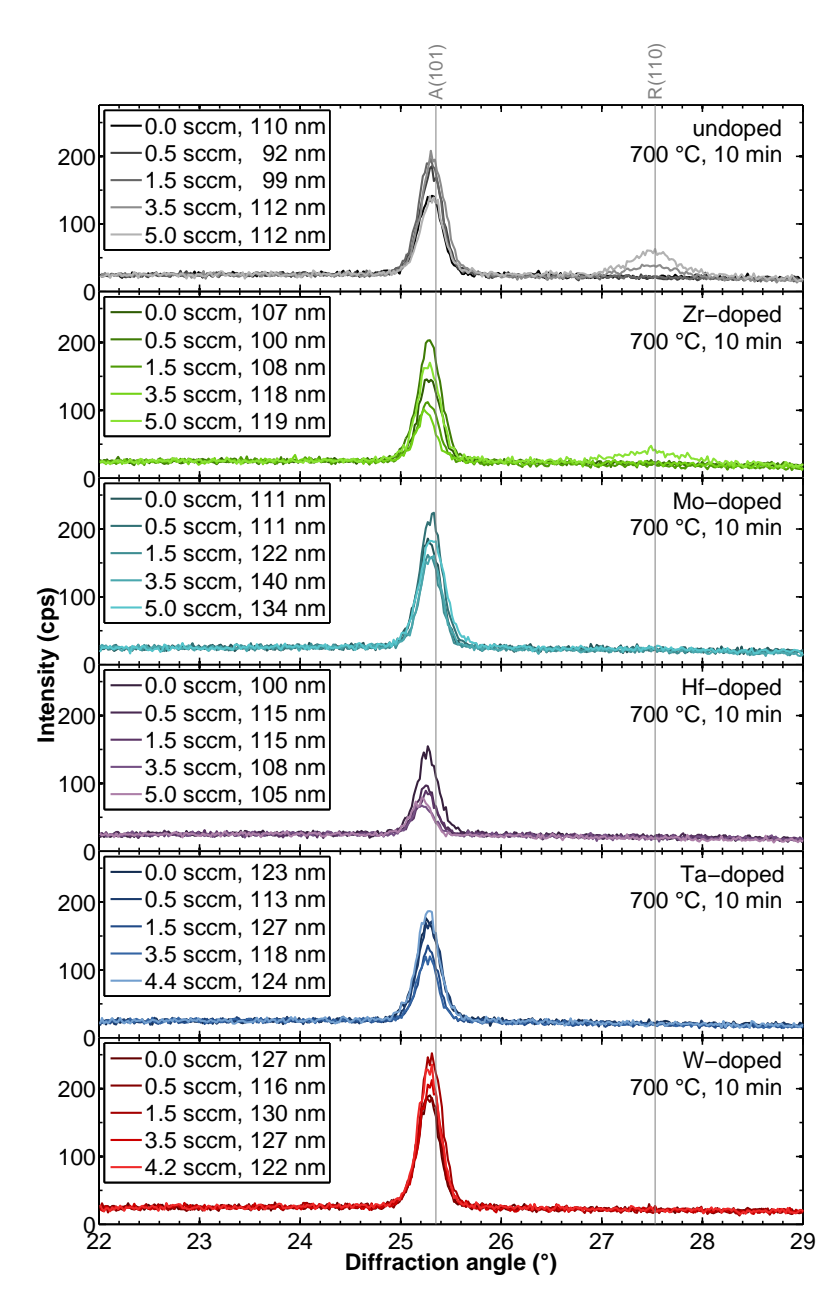


Figure 7.7 | GI-XRD measurements of TiO_2 ann. at $700\,^{\circ}C$ with ART-inhibiting dopants. Undoped and with anatase to rutile transformation-inhibiting elements doped TiO_2 thin films sputtered at different O_2 flows after the transition point were annealed at $700\,^{\circ}C$ for $10\,\text{min}$ and measured by grazing incidence X-ray diffraction. All measurements are normalized to a background of 25 cps. The gray lines indicate the positions of the anatase (101) and rutile (110) peak. The transformation to rutile is suppressed for all dopants except for the Zr-doped sampes sputtered at $5.0\,\text{sccm}$ after the transition point, which can be attributed to a low dopant concentration. The height of the anatase peak can be correlated to the valence of the dopant, a higher valence results in a higher anatase peak. Extracted peak heights are plotted in Fig. 7.8.

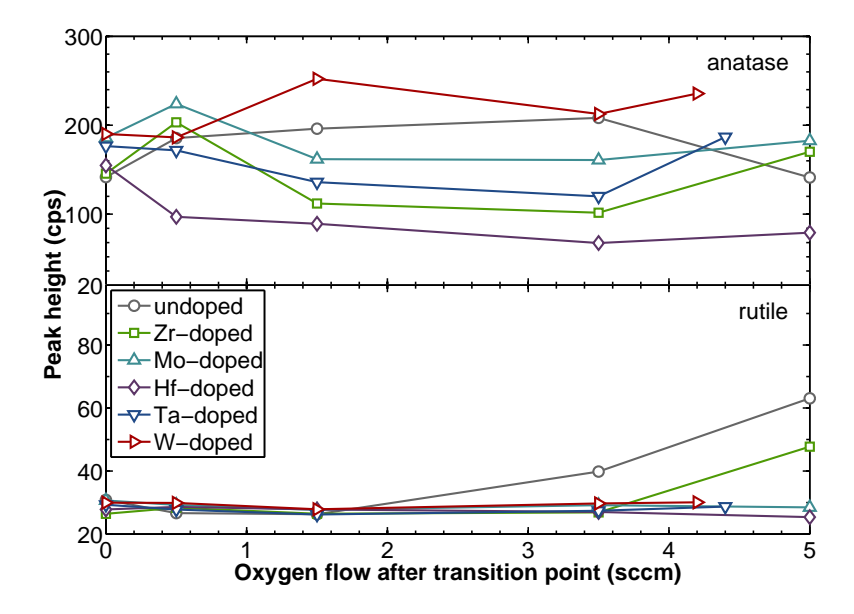


Figure 7.8 | Peak heights of TiO_2 annealed at $700\,^{\circ}C$ with ART-inhibiting dopants. The height of the anatase (top) and rutile peaks (bottom), extracted from Fig. 7.7, are plotted as a function of the O_2 flow after the transition point with respect to the utilized dopants.

slightly lower peak heights (see Fig. 7.7 and Fig. 7.8), whereas the peak heights of the samples sputtered at 3.5 sccm and 5.0 sccm after the transition point are higher. The heights of the anatase peaks of the samples annealed at 700 °C are maximal for O₂ flows of 1.5 sccm and 3.5 sccm after the transition point, having a value of about 200 cps, whereas the peak height of the undoped sample at 1.5 sccm after the transition point annealed at 300 °C reaches 250 cps. Annealing at either 300 °C for 1 h or 700 °C for 10 min results in equal anatase phases. For O₂ flows of 3.5 sccm and 5.0 sccm after the transition point, rutile peaks with peak heights of about 40 cps and 60 cps, respectively, can be seen. As rutile peaks can only be seen for high O₂ flows, this must be connected to the existence of rutile grains in the X-ray amorphous films induced by energetic bombardment during film growth. At 700 °C, existing anatase as well as rutile grains grow and anatase can be transformed to rutile, whereas at 300 °C the energy mainly provokes the growth of anatase grains. Consequently, a formation of a rutile phase is more likely at high temperatures.

Zr, Mo, Hf, Ta and W are phase transformation-inhibiting dopants due to their valence and ionic radii [HS11] (see Tab. 7.1) and therefore the transformation from anatase to rutile is suppressed by these dopants. Only one small rutile peak can be seen in the diffractogram of the Zr-doped film sputtered at $5.0 \, \text{sccm} \, \text{O}_2$ flow after the transition point. For the samples annealed at $300 \, ^{\circ}\text{C}$ it was already discussed whether the crystallization of a rutile phase in the Zr-doped samples is due to a low dopant concentration or the valence of 4. Here, Zr can be

compared to Hf, which also has a valence of 4, but successfully suppresses a crystallization of rutile. The formation of a rutile phase in the Zr-doped samples can, hence, be explained by the low dopant concentration, which is still high enough to suppress the transformation to rutile at 3.5 sccm after the transition point, but incapable of suppressing the transformation from anatase to rutile as well as the growth of rutile grains at 5.0 sccm after the transition point.

Doping with Hf, Ta and W leads to a suppression of the anatase phase during annealing at 300 °C due to the incorporation of Ar in the growing film. At 700 °C these Ar atoms cannot suppress the formation of anatase any more and the anatase phase supporting character of the dopant itself dominates the crystallization behavior, leading to pronounced anatase peaks but no formation of rutile.

The height of the anatase peaks in Fig. 7.7 and Fig. 7.8 for the films sputtered at 1.5 sccm and 3.5 sccm after the transition point can be linked to the valence of the dopant atoms. The higher the valence, the higher the anatase peak. The highest peaks are found for films doped with W, showing higher peaks than the undoped films, followed by films doped with Mo, both having a valence of 6. The peak height of the anatase peaks of films doped with Ta are in between the samples doped with Mo and Zr. Ta has a valence of 5, whereas Zr has a valence of 4, which perfectly fits the peak height to valence correlation. The samples with the least anatase peaks are the samples doped with Hf, which also has a valence of 4, showing a peak height lower than 100 cps for all samples except the one sputtered at the transition point.

The peak heights in a diffractogramm also scale with the thickness of the analyzed specimen, but as the films doped with Mo, Ta and W are equally thick, this can not be the reason for the different heights. The films doped with Zr and Hf are about $20\,\%$ thinner than those of the other three dopants, still this is not enough to explain the difference in peak heights, which are in a range of up to $300\,\%$.

7.3.2 Anatase to rutile transformation-promoting dopants

V, Cr, Mn, Cu and Sn have been shown to promote the anatase to rutile transformation [ZR02, Kar03, Mac75, SP65, KFN $^+$ 07, MRS04] and were therefore chosen in this work to investigate their influence on the phase transformation behavior of sputtered amorphous TiO₂ films.

The diffractograms of undoped and with phase transformation-promoting elements doped samples annealed at 300 °C are plotted in Fig. 7.9 and the extracted peak heights of the anatase as well as the rutile peaks are shown in Fig. 7.10. Doping with V does not seem to change the crystallization behavior of TiO₂ at 300 °C, as there is no significant difference

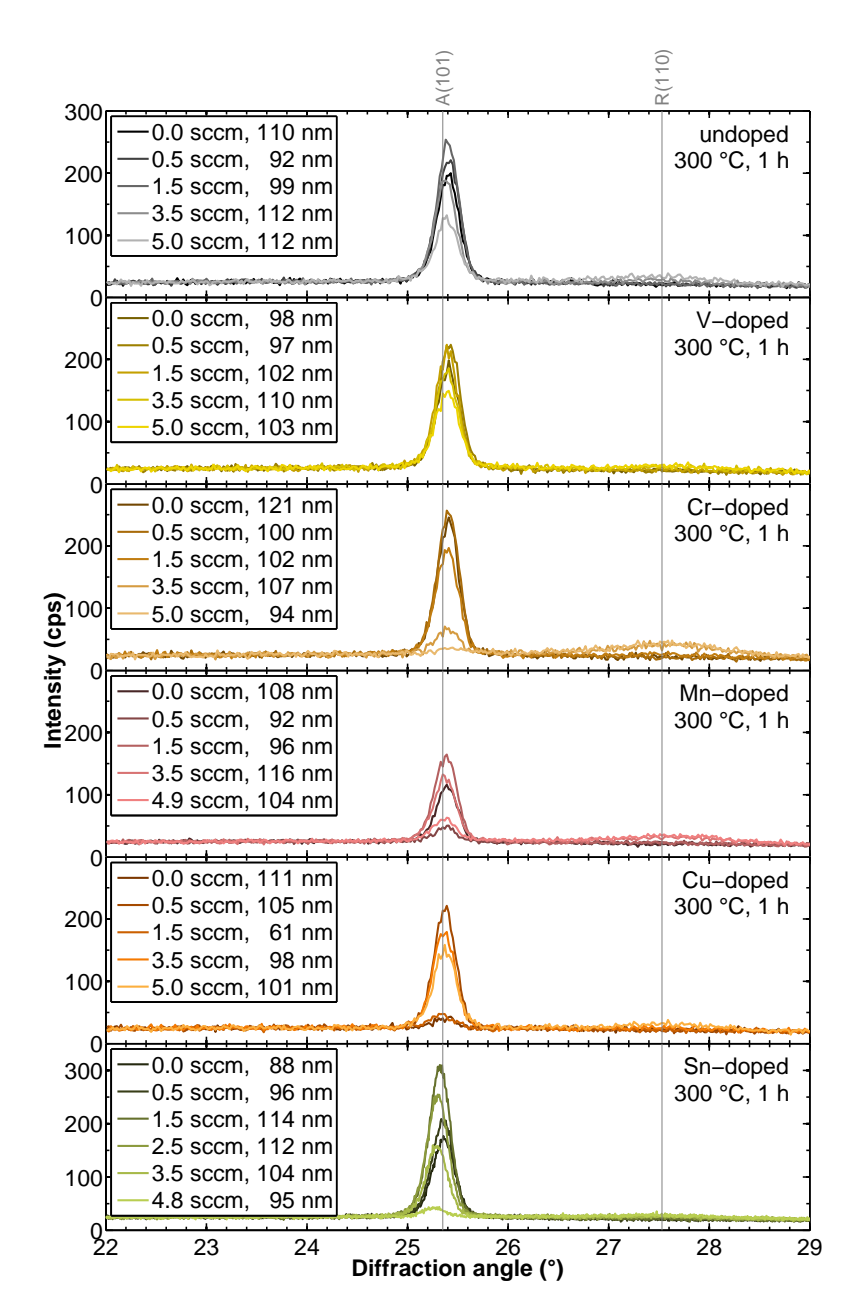


Figure 7.9 | GI-XRD measurements of TiO_2 ann. at 300 °C with ART-promoting dopants. Undoped and with anatase to rutile transformation-promoting elements doped TiO_2 thin films sputtered at different O_2 flows after the transition point were annealed at 300 °C for 1 h and measured by grazing incidence X-ray diffraction. All measurements are normalized to a background of 25 cps. The limits of the intensity scale of the diffractograms of the Sndoped samples (bottom) are adjusted to fit the data. The gray lines indicate the positions of the anatase (101) and rutile (110) peak. Cr, Mn and Sn show a deterioration of the anatase phase at high O_2 flows, whereas Sn also promotes a crystallization of the anatase phase at low O_2 flows. Extracted peak heights are plotted in Fig. 7.10.

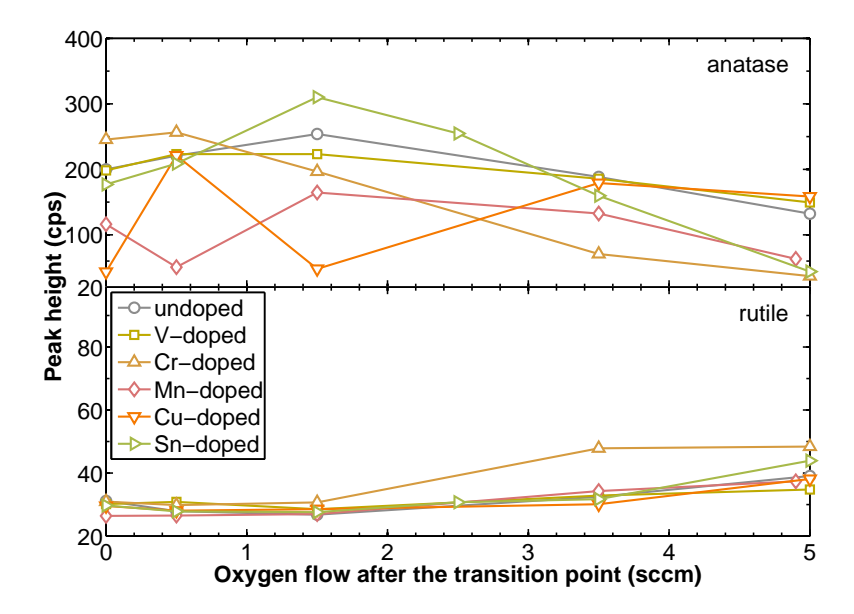


Figure 7.10 | Peak heights of TiO_2 annealed at 300 °C with ART-promoting dopants. The height of the anatase (top) and rutile peaks (bottom), extracted from Fig. 7.9, are plotted as a function of the O_2 flow after the transition point with respect to the utilized dopants.

in the peak heights of undoped and V-doped TiO_2 . The concentration of V was difficult to determine (see Sect. 7.1) and hence the missing influence might be due to a low dopant concentration. The concentration of Cu in the films is low as well and a suppression of the anatase phase upon doping with Cu can be seen only for the samples sputtered at 0.0 sccm and 1.5 sccm after the transition point. Further analysis reveales that the Cu-doped film sputtered at 1.5 sccm after the transition point has a thickness of only 61 nm, reducing the intensity of the peak. All other films have the desired thickness of about 100 nm, limiting the suppressing effect of Cu to the film sputtered at the transition point.

Cr and Mn show a deterioration of the anatase phase with increasing O_2 flow, which simultaneously implies an increasing dopant concentration (see Fig. 7.1). At 5.0 sccm after the transition point, this suppression leads to a film showing no anatase peak upon doping with Cr and to a film showing only a weak anatase peak for doping with Mn at 4.9 sccm after the transition point. With exception of the sample sputtered at 0.5 sccm after the transition point, which shows only a small anatase crystallization, the peak heights of the Mn-doped samples show a similar trend as the peak heights of the undoped samples, lowered by about $50\text{-}100\,\text{cps}$.

In contrast to all other dopants, Sn promotes the crystallization of the anatase phase at 1.5 sccm after the transition point, but then deteriorates it at higher O_2 flows, leading to a

Table 7.2 | Comparison of ionic radii in sixfold coordination of ART-promoting dopants. V, Cr, Mn, Cu and Sn will only promote the transformation from anatase to rutile if they substitute Ti with a valence of 2, according to Eq. 7.2. Data taken from [Sha76], no precise value is provided for Sn²⁺ as the coordination is too irregular.

Dopant	Ti	V	Cr	Mn	Cu	Sn
Radius Me ¹⁺ (Å)					0.91	
Radius Me ²⁺ (Å)		0.93	0.87	0.81	0.87	>1.1
Radius Me ³⁺ (Å)		0.78	0.76	0.72	0.68	1.10
Radius Me ⁴⁺ (Å)	0.75	0.72	0.69	0.67		0.83
Radius Me ⁵⁺ (Å)		0.68	0.63			

nearly full suppression of the anatase phase at 4.8 sccm after the transition point. To verify the maximum at 1.5 sccm after the transition point, another sample sputtered at 2.5 sccm after the transition point was deposited and added to the comparison, showing a slightly lower peak height.

For none of the dopants a pronounced rutile phase can be observed, however, the highest rutile peaks can be seen for the Cr-doped samples sputtered at $3.5 \, \rm sccm$ and $5.0 \, \rm sccm$ after the transition point. The transformation to rutile is not significantly promoted by V, Mn, Cu or Sn at temperatures of $300 \, ^{\circ} \rm C$.

The anatase to rutile transformation-promoting or -inhibiting character of a dopant is predicted by Eq. 2.2 in Sect. 2.2.2, which distinguishes between a promoting radius r_{promoter} and an inhibiting radius $r_{\text{inhibitor}}$ depending on the valence n of the dopant:

$$r_{\text{promoter}} < (-0.455 n + 2.045) \text{ Å} < r_{\text{inhibitor}}.$$
 (7.2)

As a consequence, an element has to have a radius $r_{n=2} < 1.14 \text{Å}$ or $r_{n=3} < 0.68 \text{Å}$, to be an anatase to rutile phase transformation-promoting dopant. The ionic radii for possible valences of V, Cr, Mn, Cu and Sn upon substitution of Ti can be found in Tab. 7.2. Comparing their radii reveals, that these elements will only promote the transformation from anatase to rutile if they occur as Me^{2+} .

Hanaor and Sorrell stated that Cr, Mn, Cu and Sn promote the anatase to rutile transformation as their most common valence is 2 and therefore increase the number of oxygen vacancies [HS11], which allow an easier transformation to rutile by weakening the oxygen sub-lattice [SP65]. From Fig. 7.9 and Fig. 7.10 it can be seen that these dopants do not only promote a transformation from anatase to rutile in powders, but also suppress a crystallization of the anatase phase in an amorphous sample, which can also be explained by a weakening of the oxygen sub-lattice.

Mn is likely to change its valence from Mn^{4+} to Mn^{2+} above temperatures of 400 °C as oxygen is released [WYMZ97, HS11], altering its character from inhibiting to promoting the anatase to rutile transformation during annealing. In consequence, Mn should support the anatase formation at 300 °C, but the opposite behavior is observed, leading to the conclusion that Mn^{2+} already forms during sputtering or during annealing at 300 °C.

As Cr and Mn successfully deteriorate a crystallization of the anatase phase at high O_2 flows and V has no influence, it is most likely that Cr occurs in the amorphous film with a valence of 2, like Mn, whereas V occurs with a higher valence, as long as the concentration of V is assumed to be high enough to have an influence. XPS measurements can be performed to investigate this further, but unfortunately this is beyond the scope of this work.

Cu only forms oxides with valences of 2 and 3, which both show radii promoting the phase transformation from anatase to rutile. The interpretation of the behavior of the Cu-doped samples is, however, difficult as an influence on the crystallization is only seen at the transition point. A more detailed analysis using several dopant concentrations and O_2 flows would be necessary to get a better insight into the influence of Cu doping on the crystallization behavior of TiO_2 . Unfortunately, this analysis could not be performed within this work and is therefore proposed to be investigated in future works.

Although Sn has been reported to promote the anatase to rutile transformation [MRS04], Chen et al. reported that Sn can substitute Ti in anatase Nb-doped TiO_2 films up to concentrations of 30 % [CFH⁺07]. If forming the anatase phase, the substitution is most likely to be performed as Sn^{4+} , having the smallest ionic radius. Besides, smaller valences would also weaken the oxygen sub-lattice due to a generation of oxygen vacancies. The strong deterioration of the anatase phase for higher O_2 flows suggests that the promotion of the anatase crystallization only occurs at a specific combination of dopant content and energetic flux to the growing film, which leads to the formation of more anatase grains. Using different deposition parameters might lead to the incorporation of Sn as an interstitial or as Sn^{2+} , which hinders a formation of anatase grains as well as a crystallization of the anatase phase.

Additionally to the investigations of the annealing behavior at 300 °C, X-ray amorphous samples doped with phase transformation-promoting elements were also annealed for 10 min at 700 °C and measured by grazing incidence X-ray diffraction, subsequently. The resulting diffractograms are plotted in Fig. 7.11 and the extracted peak heights of the anatase as well as the rutile peaks are shown in Fig. 7.12.

For all samples annealed at 700 °C, which were doped with anatase to rutile transformation-promoting elements, a deterioration of the anatase phase as well as an evolution of a rutile phase can be observed at high O_2 flows.

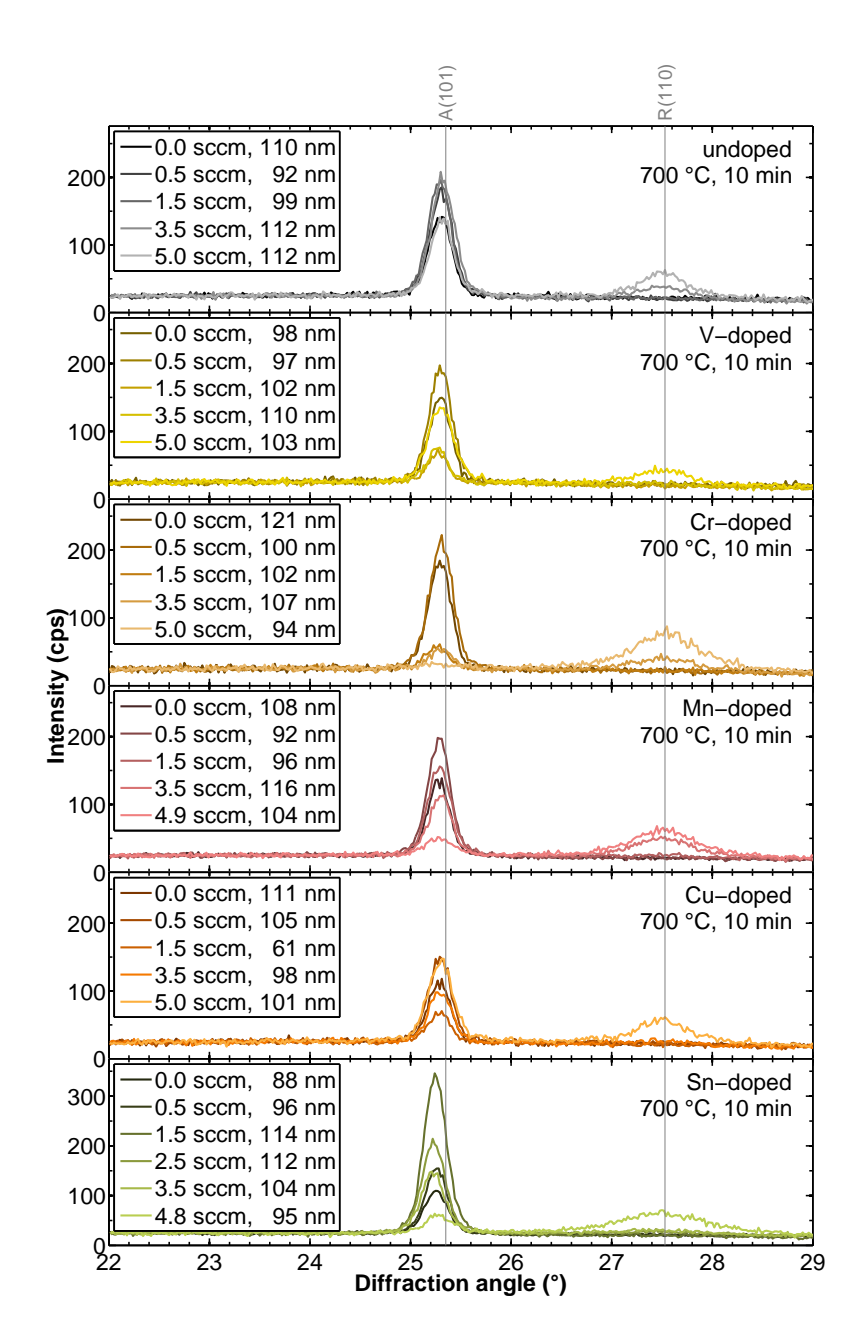


Figure 7.11 | GI-XRD measurements of TiO_2 ann. at $700\,^{\circ}\text{C}$ with ART-promoting dopants. Undoped and with anatase to rutile transformation-promoting elements doped TiO_2 thin films sputtered at different O_2 flows after the transition point were annealed at $700\,^{\circ}\text{C}$ for $10\,\text{min}$ and measured by grazing incidence X-ray diffraction. All measurements are normalized to a background of 25 cps. The limits of the intensity scale of the diffractograms of the Sn-doped samples (bottom) are adjusted to fit the data. The gray lines indicate the positions of the anatase (101) and rutile (110) peak. Upon doping a deterioration of the anatase phase is observed and a rutile peak evolves with increasing O_2 flow. In contrast to all other dopants, Sn, which also deteriorates the anatase phase at high O_2 flows, promotes it at 1.5 sccm after the transition point, resulting in the highest anatase peak of all measured samples. Extracted peak heights are plotted in Fig. 7.12.

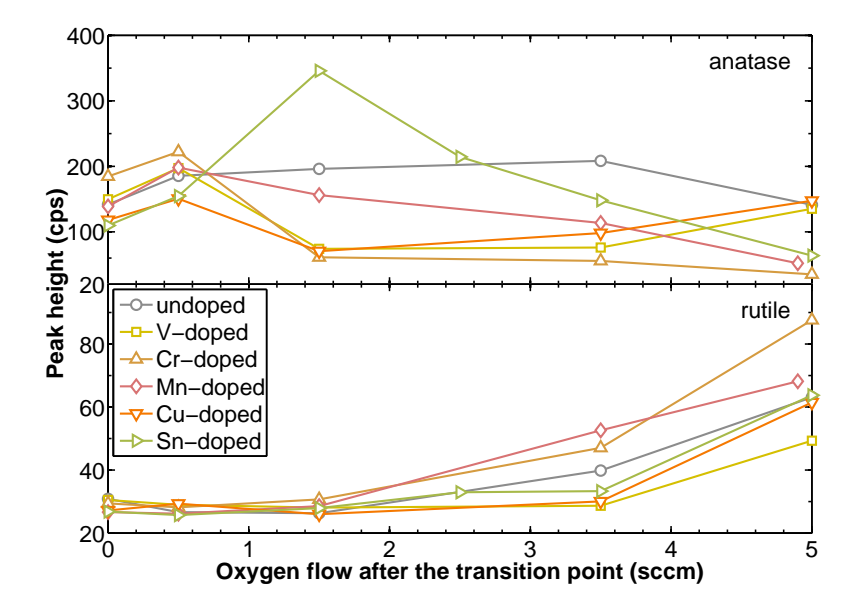


Figure 7.12 | Peak heights of TiO_2 annealed at 700 °C with ART-promoting dopants. The height of the anatase (top) and rutile peaks (bottom), extracted from Fig. 7.11, are plotted as a function of the O_2 flow after the transition point with respect to the utilized dopants.

For Cr this trend is very pronounced starting with a pure anatase film at the transition point. With increasing O_2 flow the anatase peak first increases slightly at 0.5 sccm after the transition point, as it has already been seen for the undoped films, and then decreases to very low values already at 1.5 sccm after the transition point, whereas the rutile peak simultaneously evolves ending in a pure rutile film with a higher peak height and a broader width than the undoped film sputtered at $5.0 \, \text{sccm} \, O_2$ flow after the transition point. For Mn the evolution of the peak is similar to that of the Cr-doped samples, besides the fact that the deterioration of the anatase peak and the promotion of the rutile peak are less. Still, the peak height of the rutile peak is slightly higher than that of the undoped sample. As the concentration of Mn is higher than the concentration of Cr (see Fig. 7.1), Cr is obviously more effective in promoting the crystallization of rutile.

For the samples doped with V and Cu, it can clearly be seen that the anatase peaks of the samples sputtered at $1.5\,\mathrm{sccm}$ and $3.5\,\mathrm{sccm}$ after the transition point are significantly suppressed. At $1.5\,\mathrm{sccm}$ after the transition point this might again be correlated to a decreased thickness of the Cu-doped sample, whereas all other samples, including the V-doped ones, are of about $100\,\mathrm{nm}$. At the highest O_2 flow of $5.0\,\mathrm{sccm}$ after the transition point, however, the samples doped with V and Cu show a pronounced anatase and rutile peak and no change to the undoped films can be seen in the diffractograms. Cu shows the least dopant concentration of all anatase to rutile transformation-inhibiting dopants analyzed and the concentration

Table 7.3 | **Comparison of rutile structures of different materials.** Lattice parameters and threshold of the crystallization temperature T_C . VO₂ forms rutile only above 65 °C, below it undergoes a monoclinic deformation to the MoO₂-type structure [KN79].

Material	a-axis (Å)	c-axis (Å)	<i>T_C</i> (°C)
TiO_2	4.594 [BHM ⁺ 87]	2.959 [BHM ⁺ 87]	< 600 [HS11]
VO_2	4.553 [KN79]	2.849 [KN79]	< 400 [MY06]
CrO_2	4.423 [SREF09]	2.918 [SREF09]	< 260 [EGK ⁺ 98]
MnO_2	4.398 [RSSG69]	2.874 [RSSG69]	< 450 [CWW47]
SnO_2	4.738 [Lid97]	3.188 [<mark>Lid97</mark>]	< 550 [GK74]

tration of V was difficult to determine. Therefore, the less pronounced trend within these series is likely to be correlated to the dopant concentration. This has to be kept in mind during the following discussion.

As it has already been seen for the annealing of the Sn-doped samples at $300\,^{\circ}$ C, doping with Sn also causes a special behavior for the samples annealed at $700\,^{\circ}$ C. At $1.5\,^{\circ}$ sccm after the transition point the anatase phase is significantly promoted by Sn, in contrast to all other dopants, leading to a peak height of about $350\,^{\circ}$ cps. This is the highest anatase peak measured. The undoped sample sputtered at $1.5\,^{\circ}$ sccm after the transition point for example only shows a peak height of about $200\,^{\circ}$ cps. This O_2 flow has already been shown to be suited for the formation of anatase grains, but doping with Sn amplifies the formation additionally. However, for higher O_2 flows doping with Sn does not promote the anatase phase, it even deteriorates it, and the behavior is similar to that of Mn and Cr, leading to the assumption that Sn substitutes the lattice as Sn^{4+} only at this specific O_2 flow and concentration, whereas it is incorporated as Sn^{2+} otherwise. By use of XPS measurements this may be investigated experimentally, but one has to keep in mind, that different atmospheres as well as the use of an argon gun, may have a major influence on the valence of Sn.

In general, all anatase to rutile transformation-promoting dopants seem to have an anatase phase deteriorating character, as could already be seen from the annealing experiments at $300\,^{\circ}$ C. Nevertheless, only Cr shows a real promotion of the rutile phase. The rutile peak of the Cr-doped sample sputtered at $5.0\,\mathrm{sccm}$ O₂ flow after the transition point is higher than the peaks of the samples doped with Mn and Sn sputtered at $4.9\,\mathrm{sccm}$ and $4.8\,\mathrm{sccm}$ O₂ flow after the transition point, respectively, which show about the same peak height as the undoped sample .

The formation of rutile grains is more likely for a dopant which itself is able to crystallize into rutile or a crystal structure similar to rutile. Cu occurs as Cu^{1+} and Cu^{2+} only and will not form a crystal with a stoichiometry of CuO_2 . V, Cr, Mn and Sn on the other hand do form

rutile crystal structures with similar lattice parameters to TiO_2 , as can be seen in Tab. 7.3. The crystallization temperatures of these phases are lower than the crystallization temperature of the rutile phase of TiO_2 , which may allow a rutile grain to form earlier during annealing. Additionally, anatase grains can be transformed to rutile during annealing, using the mechanisms discussed by Hanaor and Sorrell [HS11]. As CrO_2 has the lowest crystallization temperature, this dopant will increase the probability of the formation of rutile grains, which is in line with the promotion of the rutile phase observed in the annealing experiments.

In summary, it has been shown that the phase formation and transformation of serial cosputtered TiO_2 can be controlled by use of different dopants, even though no dopant has been found to alter the degree of crystallinity of as-deposited TiO_2 samples. Thermally stable TiO_2 thin films can be deposited upon doping with Hf, Ta and W, suppressing any crystallization at 300 °C, whereas doping with Mo can be employed to produce films that crystallize to anatase only. In addition, doping with Mo, Hf, Ta, and W inhibits a transformation to rutile at 700 °C. If high refractive indexes are favored, the use of Cr as a dopant allows the crystallization of films sputtered at high O_2 flows into pure rutile films at 700 °C.

Carbon print target

Multi-component metal oxides can be sputtered using compound targets, reactive co-sputtering or reactive serial co-sputtering (see Sect. 3.1). While compound targets are limited to the stoichiometry of the target used, co-sputtering and serial co-sputtering offer the possibility to tailor the stoichiometry of the resulting films. Nevertheless, depositing an exact stoichiometry in those processes is challenging since sputter yields are strongly dependent on the O_2 partial pressure in the chamber (see Chap. 6).

Ordinary co-sputtering of different targets at the same time is usually connected with an exchange of atmospheres and thereby a change in deposition rate of a least one of the components [MR99]. In serial co-sputtering, where gas separation can be achieved, the stoichiometry will change if the deposition rate of the primary or one of the auxiliary targets changes. If more material is sputtered onto the primary target this can and will change the oxygen consumption of the primary process and by this the deposition rate of the primary target itself, which will result in a nonlinear change of stoichiometry with respect to the deposition rate of the secondary process. Sputtering multi-component oxides with high stoichiometry precision therefore needs a lot of calibration work and time.

In this chapter, a new way of sputtering complex oxides by use of a carbon print target is proposed and the functional capability is proven by sputtering of TiO_2 via a carbon target.

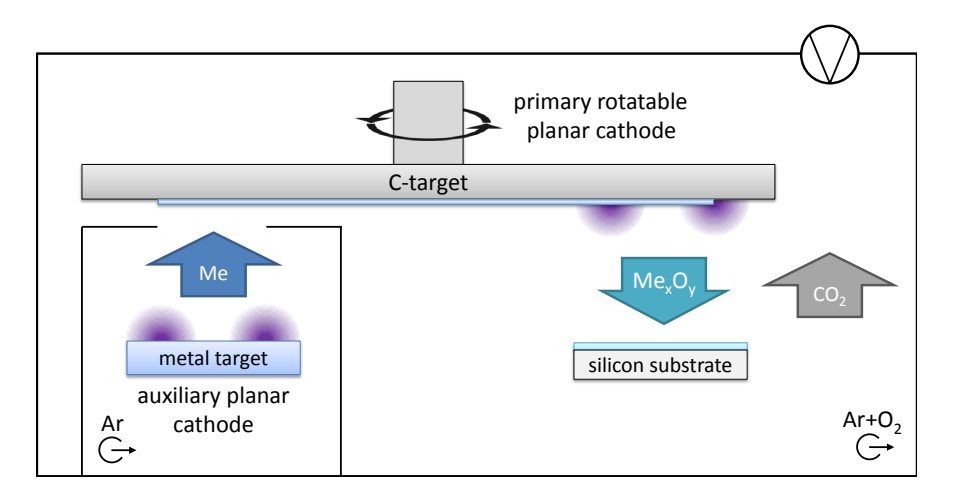


Figure 8.1 | Schematic of sputtering TiO₂ using the print target concept. A metal is sputtered onto the rotating carbon target in pure Ar atmosphere and the metal covered carbon target is simultaneously sputtered in reactive Ar/O_2 atmosphere in the primary volume. The sputtered atoms react with oxygen and Me_xO_y as well as CO_2 is formed. Some CO_2 molecules will be incorporated into the growing film, but the majority will be pumped out due to their gaseous nature, resulting in a weakly C-doped Me_xO_y film.

8.1 Concept

The carbon print target concept uses serial co-sputtering to deposit a metal oxide via a carbon target. The primary carbon target is sputtered in Ar/O_2 atmosphere and is simultaneously coated by an auxiliary cathode with a metal as is illustrated in Fig. 8.1.

If carbon is sputtered in a reactive O_2 atmosphere the deposition rate decreases drastically. The existence of oxygen enables the reaction

$$C + O_2 \longrightarrow CO_2$$
. (8.1)

CO₂ is mainly pumped out of the chamber and by that the sputtered carbon atoms do not add to the deposition rate. If metal atoms are sputtered together with carbon, these atoms react with oxygen as well and non-gaseous metal oxide molecules are formed

$$x \cdot \text{Me} + \text{C} + \left(1 + \frac{y}{2}\right) \text{O}_2 \longrightarrow \text{Me}_x \text{O}_y + \text{CO}_2.$$
 (8.2)

The resulting metal oxide molecules Me_xO_y condense on the substrate. Some CO_2 molecules will be incorporated into the growing film, but the majority will be pumped out due to their gaseous nature, resulting in a weakly C-doped Me_xO_y film.

As long as the erosion rate at the main target is high enough to sputter all metal atoms which are deposited from the auxiliary cathode on the rotating target and the O_2 partial pressure is

Table 8.1 | **Deposition rates of carbon sputtered in Ar/O₂ atmosphere.** The deposition time was $3600 \, \text{s}$ for all samples. For sample number 4 the deposition rate is $100 \, \text{times}$ lower than that of pure carbon $(0.15 \, \text{nm/s})$, indicating that nearly all carbon is oxidized to CO_2 and pumped out of the chamber. The decreasing thickness indicates that there was some residual metal left in the target from prior experiments.

Number	Thickness (nm)	Rate (nm/s)	Density (g/cm ³)
1	9.4	0.0026	4.3
2	7.4	0.0021	3.8
3	6.4	0.0018	3.9
4	5.4	0.0015	3.9

high enough to enable the oxidation of all sputtered carbon and metal atoms, the deposition rate of the metal oxide can be varied in situ by changing the metal deposition rate, being a linear function of the auxiliary target power.

8.2 Sputtering carbon in reactive atmosphere

To prove the functionality of the print target concept, it is necessary to show that sputtering of carbon in a reactive atmosphere leads to a drastically lowered deposition rate. All carbon atoms should be pumped out of the chamber in the form of CO_2 as long as enough oxygen is present for maintaining the complete reaction of all carbon atoms to CO_2 .

After sputtering Nb-doped carbon films, the auxiliary cathode was switched off and four films were sputtered onto silicon substrates in oxygen rich reactive Ar/O_2 atmosphere using 35 sccm O_2 flow. The films were deposited one after each other, for 3600 s each, without any co-deposition. The resulting films were measured by X-ray reflection (see Sect. 4.1.1) and subsequently fitted to determine film thicknesses and densities (see Tab. 8.1).

The deposition rate decreases from $0.0026\,\mathrm{nm/s}$ to $0.0015\,\mathrm{nm/s}$ with increasing sample number. For the last sample, this is already a 100 times lower deposition rate compared to carbon sputtered in Ar atmosphere [SRP+14]. The decreasing deposition rate over time indicates that the deposited films consist of $\mathrm{Nb}_2\mathrm{O}_5$ formed from Nb, which was left in the target from previous experiments. During sputtering some of the Nb atoms get re-implanted into the target surface instead of being removed [BBG+92, KSA+12] and the dopant concentration in the top layer of the target decreases only slowly with time.

The determined density of $4.3 \, \text{g/cm}^3$ for the first film matches the density of DC sputtered Nb₂O₅ thin films [KFRS99]. The remaining films show lower densities of $3.8 \, \text{g/cm}^3$ and

Table 8.2 | Determined thicknesses of TiO₂ sputtered using the carbon print target. The rate is only dependent on the discharge power used at the auxiliary cathode.

Auxiliary Power (W)	Deposition time (s)	Thickness (nm)	Rate (nm/s)
0	3600	5.4	0.002
200	3600	38.8	0.011
300	3600	53.5	0.015
300	10000	160.1	0.016

3.9 g/cm³. This can either be explained by an increasing carbon content in the resulting films or might just be originated in the lower thicknesses, as very thin films often show a decreased density due to their growth behavior in early stage of film formation [Mül86].

The results show that nearly no carbon is deposited upon sputtering a carbon target in reactive atmosphere. The serial co-sputtering concept is therefore suitable for being used to sputter a metal oxide using the carbon target as a print target.

8.3 TiO₂ via carbon print target

As nearly no carbon reaches the substrates upon sputtering of carbon in reactive atmosphere, the functionality of the print target approach can now be tested by adding metal atoms to the process. Ti was chosen to be sputtered onto the rotating carbon target, leading to a deposition of TiO_2 . As all Ti atoms, which are sputtered from the carbon target in the primary process, originate from the deposition onto the rotating target in the auxiliary process, the deposition rate of TiO_2 should be a linear function of the auxiliary power.

Titanium was sputtered onto the rotating carbon cathode using aperture L and auxiliary powers of 200 W and 300 W. Accordingly, Ti and carbon were sputtered in the primary erosion zone transforming to CO_2 and TiO_2 . Deposition times of 3600 s in case of 200 W auxiliary power and 3600 s or 10000 s in case of 300 W auxiliary power were used. Deposition rates were deduced from ellipsometry measurements and are summarized in Tab. 8.2. It can be seen that the deposition rate of TiO_2 changes linearly with the auxiliary power independent of the discharge current of the rotating target, which was kept constant, proving the concept of the print target. The process is considered to be stable since longer deposition times result in thicker films but unchanged deposition rate.

To analyze the amount of carbon, which was incorporated into the films during deposition, XPS measurements (see Sect. 4.3.3) of the thickest film were performed and are shown in Fig. 8.2. The sample was measured as-deposited and after different sputter cleaning times

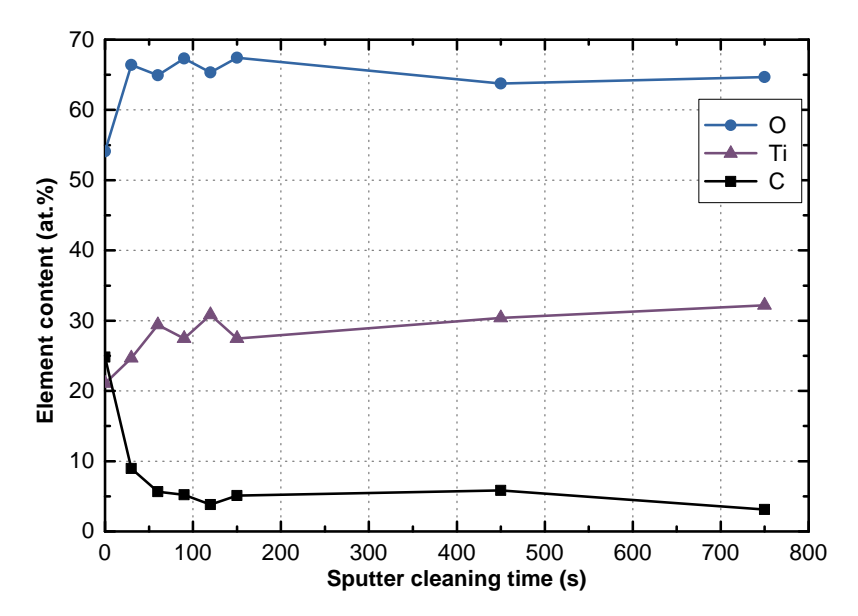


Figure 8.2 | XPS stoichiometry measurements of TiO_2 sputtered via carbon print target. The sample was measured as-deposited and after different sputter cleaning times by use of an Ar gun, to remove residual carbon on the surface and to probe a depth profile and finally the bulk composition. The sputter cleaning time of the Ar gun is a measure for the depth. Elemental Ti and oxygen concentrations match the stoichiometry of TiO_2 .

by use of an Ar gun, to remove residual carbon on the surface and to probe a depth profile and finally the bulk composition. At the surface, the contamination of the film is quite high, showing a carbon concentration of about 25 at.%, but after 750 s of sputtering a bulk composition of only 3.1 at.% is determined. Elemental Ti and oxygen concentrations match the stoichiometry of TiO_2 . During the deposition process only a small amount of carbon is incorporated in the resulting TiO_2 film.

As this is only a first proof of the carbon print target concept, the oxygen partial pressure and the auxiliary power were not optimized for a low carbon content. Increasing the auxiliary power should further decrease the carbon content and thus result in a purer ${\rm TiO_2}$ film. In the future, this method can therefore, by use of several auxiliary cathodes, be used to produce complex multi-component oxides with high stoichiometry precision if a small amount of carbon can be neglected.

Part III Conclusion & Outlook

Conclusion

Serial co-sputtering offers an unrivaled flexibility as well as in situ control of the dopant content and has therefore been utilized in this work to systematically investigate the influence of different dopants on the sputter processes and film properties of carbon and TiO_2 , with respect to deposition rate, refractive index and phase formation.

Deposition rates of carbon can be significantly increased by target doping with Nb and W. At a dopant concentration of 3 at.%, Nb increases the deposition rate of carbon by 130 %, whereas W increases it by 280 %. Due to its higher mass, W is more effective than Nb, even though Nb can significantly increase the deposition rate of carbon, too. TRIDYN simulations have been performed which reproduce the experimental data. These simulations indicate that saturation might occur at higher dopant concentrations, which have not been reached in the experiments. Additionally, the experiments performed find evidence for very long residual times of the dopant in the target as a result of recoil implantation.

Doping with Hf, Ta and W increases the deposition rate of TiO_2 by 115%, 80% and 110% at the transition point, respectively, whereas Pb and Bi, due to their low surface binding energies, are not capable of increasing the deposition rate significantly. The large rate enhancement upon doping of TiO_2 with Hf can not be predicted by surface binding energies or densities. Yet, thermodynamic considerations reveal that the formation of TiO_{2-x} suboxides, resulting in a more metallic target surface, a lower target voltage and consequently a higher sputter yield of Ti, is the origin of this impressive effect. Using HiPIMS, the rate amplification can be further enhanced. Optical emission spectroscopy reveals that in HiPIMS the dopant atoms get ionized and are accelerated towards the target resulting in a deeper implantation depth and by that a more effective sputter yield amplification.

Additionally to the rate enhancement, refractive indexes of TiO₂ upon doping with sputter yield amplifying elements have been analyzed. The refractive index of TiO₂ is slightly lowered upon heavy element doping. Nevertheless, the highest refractive indexes are achieved next to the transition point, which is ideal for industrial applications as rates and sputter

yield amplification are maximal at this point, giving a clear concept for high rate, high index TiO₂ thin films.

The phase transformation of amorphous TiO_2 can be controlled by doping with different elements, even though no dopant has been found to alter the degree of crystallinity of asdeposited TiO_2 samples. The transformation behavior of doped TiO_2 can be linked to the valence and ionic radius of the dopant as well as the incorporation of Ar in the growing film. Thermally stable TiO_2 thin films can be deposited upon doping with Hf, Ta, and W, suppressing any crystallization at 300 °C, whereas doping with Mo can be employed to produce films that crystallize to anatase only. In addition, doping with Mo, Hf, Ta, and W inhibits a transformation to rutile at 700 °C, whereas the use of Cr as a dopant allows the crystallization into pure rutile films, if high refractive indexes are favored.

Finally, the functionality of the carbon print target concept has been proven. Sputtering a doped carbon target in reactive Ar/O_2 atmosphere leads to the deposition of a metal oxide, matching the stoichiometry of the dopants. Only a small amount of carbon is found in the resulting film. Using several auxiliary cathodes in serial co-sputtering, this method can be utilized to produce complex multi-component oxides with high stoichiometry precision.

In this work, the potential of serial magnetron co-sputtering has been used to tailor the process conditions and film properties of carbon and TiO_2 . The results presented add to the understanding of the sputter yield amplification effect and the crystallization and transformation behavior of doped TiO_2 thin films, allowing for a tailoring of their properties with respect to the desired field of application. The results can be readily used for deposition of doped TiO_2 and carbon based thin films in industrial applications.

Outlook

Although the results of this work can be readily used for deposition of doped TiO_2 and carbon based thin films in industrial applications, the findings give rise to various follow-on experiments, investigations, considerations and scientific questions.

Target doping by heavy elements has been shown to increase the deposition rate of carbon and TiO_2 . While the increase in deposition rate of carbon is as predicted and, hence, should be similar for other non-oxides, it was necessary to extend the model to explain the increase in deposition rate of TiO_2 by thermodynamic considerations. A major question is whether this model remains its applicability if transferred to the deposition of other oxides. Consequently, the systematic investigation of sputter yield amplification of other oxides by doping with Hf in comparison to other heavy element doping is proposed here.

Furthermore, the doping with heavy elements leads to an increased bombardment of the growing film by neutral Ar ions. These Ar ions are incorporated and inhibit a phase transformation in case of TiO_2 and lead to a densification upon sputtering of carbon. This effect of densification may alter the mechanical properties of the carbon films, which have not been investigated in the scope of this work. Additional measurements on hardness and wear resistance of the doped carbon films would complete the picture.

Several dopants have been shown to alter the crystallization behavior of TiO_2 . Nevertheless, so far, any information in this work on how these atoms are incorporated as well as their valance state in the lattice has been derived from literature. X-ray absorption fine structure (EXAFS) as well as XPS measurements of doped TiO_2 thin films would give a deeper understanding of the underlying microscopic mechanisms and bondings. These results could then be used to tailor the sputter process and consequently to control the structure formation of the deposited films to an even higher extend.

All TiO₂ films investigated in the frame of structure evolution upon doping in this work exhibit an as-deposited amorphous structure. By use of different discharge parameters, sput-

ter chamber geometries, target sizes and discharges, the energy transferred to the growing film and by that the as-deposited crystal structure can be significantly altered. HiPIMS deposition for example offers the possibility to sputter as-deposited rutile films. Combining the advantages of HiPIMS with the results of this work may increase the degree of crystallinity and by that the optical and mechanical properties of as-deposited TiO₂. Especially the combination of deposition of TiO₂ utilizing HiPIMS and Cr-doping, which has been shown to significantly increase the rutile content upon heating of DC sputtered films, shall be proposed here.

Using several auxiliary cathodes in serial co-sputtering in combination with a carbon target in reactive Ar/O_2 atmosphere, complex multi-component oxides with high stoichiometry precision can be sputtered. In this work, the basic concept has been proven by sputtering TiO_2 , but the sputtering of a multi-component oxide still remains. A good candidate for future experiments would be Mayenite ($Ca_{12}Al_{14}O_{33}$).

In summary, serial co-sputtering, which offers a versatile method for the systematic investigation of dopants, alloys and oxides, will be an important contribution to future material research in terms of tailoring optical, structural as well as mechanical properties of thin films.

Part IV Appendix

Appendix A

List of acronyms and abbreviations

The following acronyms and abbreviations, listed in alphabetically order, have been used in this work. Quantity symbols are not listed.

a/d as-deposited

Al₂O₃ aluminium oxide / alumina

Ar argon

ART anatase to rutile transformation BCA binary collision approximation

Bi bismuth C carbon

COSMOS serial co-sputtering for functional multi component thin films

Co cobalt

Cr chromium

CrO₂ chromium dioxide

Cu copper

CVD chemical vapor deposition

DC direct current
DDG digital direct gate

DOS density of states

EDX energy-dispersive X-ray (spectroscopy)

EPMA electron probe microanalyzer (spectroscopy)
EXAFS extended X-ray absorption fine structure

Appendix A: List of acronyms and abbreviations

Fe iron
Hf hafnium

HfO₂ hafnium dioxide / hafnia

HiPIMS high power impulse magnetron sputtering

H₂O water

HPPMS high-power pulsed magnetron sputtering

ICCD intensified charge-coupled device

Me metal

 Me_xO_y metal oxide Mo molybdenum

MoO₂ molybdenum dioxide

Mn manganese

MnO₂ manganese dioxide

Nb niobium

Nb₂O₅ niobium pentoxide

 O_2 oxygen

OES optical emission spectroscopy

Pb lead

pDC pulsed direct current (magnetron sputtering)

RBS rutherford backscattering spectrometry
RF radio frequency (magnetron sputtering)

Si silicon Ta tantalum

Ta₂O₅ tantalum pentoxide

TCO transparent conductive oxide

Ti titanium

TiO₂ titanium dioxide / titania

 TiO_{2-x} titanium suboxide TP transition point

UV ultraviolet

UV-VIS ultraviolet-visible

V vanadium

VO₂ vanadium dioxide

W tungsten

WO₃ tungsten trioxide

SBE surface binding energy

Sn tin

SnO₂ tin dioxide

SYA sputter yield amplification

XPS X-ray photoelectron spectroscopy

XRD X-ray diffraction XRR X-ray reflectivity

Zr zirconium

ZrO₂ zirconium dioxide / zirconia

Appendix B

Dopant deposition rates

In this work, carbon and TiO_2 thin films have been doped by various elements using serial co-sputtering (see Sect. 3.1.1). The amount of dopant incorporated in the resulting film has been controlled by adjusting the dopant deposition rate R onto the rotating target using different auxiliary powers P_{aux} and apertures.

$$R = r' \cdot P_{\text{aux}} \cdot f_{\text{AP}} = r \cdot P_{\text{aux}} \tag{B.1}$$

where r' is the material specific dopant deposition rate per power and $f_{\rm AP}$ is the geometry factor of the aperture. Both values are included in the material specific dopant deposition rate per power and aperture r.

If auxiliary power and aperture are known, an experiment can be reproduced, resulting in the same dopant deposition rate. However, different apertures can lead to the same dopant deposition rate onto the rotating target if matching auxiliary powers are used. The dopant deposition rate is therefore sufficient to describe the doping process, allowing for a reproduction of the experiments, without knowing the utilized aperture and auxiliary power.

However, sputtering different dopants with the same deposition rate will not necessarily lead to the same number of atoms deposited onto the rotating cathode if the atom densities of the dopants are different. In this case, the densities ρ and the atomic masses M of the dopants need to be known to calculate the atom rate (number of deposited atoms per time, area and aperture) \dot{N} .

$$\dot{N} = R \cdot \frac{\varrho}{M} \tag{B.2}$$

Table B.1 | Density and deposition rates of different dopants onto the rotating target. Density and thickness values have been determined by XRR and the material specific deposition rate per power and aperture as well as the number of deposited atoms per time, area and aperture have been calculated using Eq. B.4 and Eq. B.5.

Material	Aperture	Deposition rate (nm/Wh)	Norm. atom rate (nmol/cm ² Wh)
Cu	L	1.14	1.59
Nb	L	0.48	2.61
Hf	L	0.99	5.55
Ta	L	0.70	4.45
W	L	0.52	3.95
Pb	M	0.88	2.59
Bi	M	0.58	2.74

Unfortunately the density of a sputtered thin film can be significantly different to that of the bulk material and densities need to be measured for each dopant.

In practice, deposition rates are calculated by measuring the thickness d of a deposited layer, since used auxiliary power P_{aux} and deposition time t are known:

$$R = \frac{d}{t} \tag{B.3}$$

$$R = \frac{d}{t}$$

$$r = \frac{R}{P_{\text{aux}}} = \frac{d}{t \cdot P_{\text{aux}}},$$
(B.3)

If the density ρ of the deposited film is known the atom rate \dot{N} can then be calculated using Eq. B.2. For reproduction purposes it is useful to normalize the atom rate to the auxiliary power P_{aux} used during the experiment:

$$\dot{n} = \frac{\dot{N}}{P_{\text{aux}}} = \frac{d \cdot \varrho}{t \cdot M \cdot P_{\text{aux}}} \tag{B.5}$$

The deposition rates of different dopants were determined by exchanging the primary target with a substrate holder in order to sputter on glass substrates instead of the rotatory target. The resulting samples were analyzed by XRR (see Sect. 4.1.1) and the material specific deposition rates per power and aperture r as well as the normalized atom rate \dot{n} were calculated. Summarized values can be found in Tab. B.1.

Appendix C

Optical emission lines

Spectral emission lines assigned within this work are summarized in Tab. C.1. The orbital transitions are given using the Russell-Saunders term symbol [RS25] of multi-electron atoms.

Table C.1 | Spectral emission lines assigned within this work. Wavelenth, species, oribital transition and reference are provided. Data taken from [KRRN13].

Wavelength	Species, Transition	Referenz
239.710729	WII, $5d^5 {}^6S_{5/2} \longrightarrow 5d^4({}^5D)6p {}^6F_{7/2}^{\circ}$	[EKM00]
244.016470	Ti II, $3d^3 b^2 D2_{3/2} \longrightarrow 3d(^2D)4s4p(^3P^\circ) w^2 D_{3/2}^\circ$	[RVC75]
245.043470	Ti II, $3d^3 b^2 D2_{5/2} \longrightarrow 3d(^2D)4s4p(^3P^\circ) w^2 D_{5/2}^\circ$	[RVC75]
246.652281	W II, $5d^4(^5D)6s {}^6D_{3/2} \longrightarrow 5d^4(^5D)6p {}^6F_{5/2}^{\circ}$	[EKM00]
247.779535	W II, $5d^4(^5D)6s ^6D_{9/2} \longrightarrow 5d^3(^4F)6s(^5F)6p ^6G_{9/2}^{\circ}$	[EKM00]
248.923	W II, $5d^4(^5D)6s {}^6D_{7/2} \longrightarrow 5d^4(^5D)6p {}^6F_{7/2}^{\circ}$	[EKM00]
249.747880	W II, $5d^4(^5D)6s ^6D_{9/2} \longrightarrow 3s^23p^4(^3P)5p^{\circ}_{7/2}$	[EKM00]
249.968342	W II, $5d^5 {}^6S_{5/2} \longrightarrow 3s^23p^4({}^1D)4d {}^2F_{5/2}$	[EKM00]
251.55932	Ar II, $3s^23p^4(^3P)4p^2P_{1/2}^{\circ} \longrightarrow 3s^23p^4(^1D)4d^2P_{1/2}$	[WAC ⁺ 95]
251.743134	Ti II, $3d^3 b^4 F_{7/2} \longrightarrow 3d^2 (^3P) 4p y^4 D_{7/2}^{\circ}$	[PTP01]
253.6521	Hg I, $5d^{10}6s^2 {}^{1}S_0 \longrightarrow 5d^{10}6s6p {}^{3}P_1^{\circ}$	[SSR96]
368.51921	Ti II, $3d^2(^3F)4s a^2F_{5/2} \longrightarrow 3d^2(^3F)4p z^2D_{3/2}^{\circ}$	[Int28]
	Ti II, $3d^2(^3F)4s a^2F_{7/2} \longrightarrow 3d^2(^3F)4p z^2D_{5/2}^{\circ}$	
375.92915	Ti II, $3d^2(^3F)4s a^2F_{7/2} \longrightarrow 3d^2(^3F)4p z^2F_{7/2}^{6/2}$	[DK80]
811.5311	Ar I, $3s^23p^5(^2P_{3/2}^{\circ})4s^2[3/2]_2^{\circ} \longrightarrow 3s^23p^5(^2P_{3/2}^{\circ})4p^2[5/2]_3$	[Nor73]

Bibliography

- [Ahn03] Y. Ahn. Variation of structural and optical properties of sol-gel TiO2 thin films with catalyst concentration and calcination temperature. *Materials Letters*, 57(30):4660–4666, 2003. Cited on page 12.
- [Aja99] P. M. Ajayan. Nanotubes from Carbon. *Chemical Reviews*, 99(7):1787–1800, 1999. Cited on page 8.
- [AKW10] A. Amin, D. Köhl, and M. Wuttig. The role of energetic ion bombardment during growth of TiO 2 thin films by reactive sputtering. *Journal of Physics D: Applied Physics*, 43(40):405303, 2010. Cited on pages 12, 30, 76, 77, and 78.
- [AKZ⁺11] M. Austgen, D. Koehl, P. Zalden, T. Kubart, T. Nyberg, A. Pflug, M. Siemers, S. Berg, and M. Wuttig. Sputter yield amplification by tungsten doping of Al2O3. *Journal of Physics D: Applied Physics*, 44(34):345501, 2011. Cited on pages 4, 20, 25, 47, and 51.
 - [And11] A. Anders. Discharge physics of high power impulse magnetron sputtering. *Surface and Coatings Technology*, 205:S1–S9, 2011. Cited on page 68.
 - [Ant95] J. W. Anthony. *Handbook of mineralogy*. Mineral Data Publ, Tucson, Ariz, 2. print edition, 1995. Cited on pages 8, 10, and 11.
- [APM⁺05] J. Alami, Persson, P. O. Ã..., D. Music, J. T. Gudmundsson, J. Bohlmark, and U. Helmersson. Ion-assisted physical vapor deposition for enhanced film properties on nonflat surfaces. *Journal of Vacuum Science & Technology A: Vacuum, Surfaces, and Films*, 23(2):278, 2005. Cited on page 26.
- [ASL⁺12] A. Aijaz, K. Sarakinos, D. Lundin, N. Brenning, and U. Helmersson. A strategy for increased carbon ionization in magnetron sputtering discharges. *Diamond and Related Materials*, 23:1–4, 2012. Cited on page 9.

- [ASMW06] J. Alami, K. Sarakinos, G. Mark, and M. Wuttig. On the deposition rate in a high power pulsed magnetron sputtering discharge. *Applied Physics Letters*, 89(15):154104, 2006. Cited on pages 12, 26, 38, 53, and 66.
 - [ATK10] M. J. Allen, V. C. Tung, and R. B. Kaner. Honeycomb Carbon: A Review of Graphene. *Chemical Reviews*, 110(1):132–145, 2010. Cited on page 8.
 - [Aus11] M. Austgen. Serielles Co-Sputtern: Entwicklung einer flexiblen Beschichtungstechnologie und deren Charakterisierung am Beispiel der Ratenerhöhung von Metalloxiden durch Co-Dotierung. PhD thesis, RWTH Aachen, 2011. Cited on pages 20, 53, 57, 58, 59, 60, and 70.
 - [AYR⁺12] A. Ali, E. Yassitepe, I. Ruzybayev, S. Ismat Shah, and A. S. Bhatti. Improvement of (004) texturing by slow growth of Nd doped TiO2 films. *Journal of Applied Physics*, 112(11):113505, 2012. Cited on page 77.
 - [BBB96] G. Bergerhoff, M. Berndt, and K. Brandenburg. Evaluation of Crystallographic Data with the Program DIAMOND. *Journal of Research of the National Institute of Standards and Technology*, 101:221–225, 1996. Cited on page 10.
- [BBG⁺92] S. Berg, A. M. Barklund, B. Gelin, C. Nender, and I. Katardjiev. Atom assisted sputtering yield amplification. *Journal of Vacuum Science & Technology A: Vacuum, Surfaces, and Films*, 10(4):1592, 1992. Cited on pages 9, 12, 25, 47, 53, 58, 60, 84, and 101.
- [BBN⁺92] S. Berg, A. M. Barklund, C. Nender, I. V. Katardjiev, and H. Barankova. Sputter erosion amplification. *Surface and Coatings Technology*, 54-55:131–135, 1992. Cited on pages 25 and 60.
- [BBW⁺96] F. P. Bundy, W. A. Bassett, M. S. Weathers, R. J. Hemley, H. U. Mao, and A. F. Goncharov. The pressure-temperature phase and transformation diagram for carbon; updated through 1994. *Carbon*, 34(2):141–153, 1996. Cited on page 8.
 - [BE07] R. Behrisch and W. Eckstein, editors. *Sputtering by particle bombardment: Experiments and computer calculations from threshold to MeV energies*, volume 110 of *Topics in Applied Physics*. Springer, Berlin and New York, 2007. Cited on pages 4, 9, and 45.
 - [Bec67] E. Becquerel. *La lumière, ses causes et ses effets*. F. Didot Frères, 1867. Cited on page 36.

- [Beh81] R. Behrisch. Sputtering by Particle Bombardment I: Physical Sputtering of Single-Element Solids, volume 47 of Topics in Applied Physics. Springer, Berlin and Heidelberg, 1981. Cited on pages 24 and 49.
- [Bel93] A. Belkind. Cosputtering and serial cosputtering using cylindrical rotatable magnetrons. *Journal of Vacuum Science & Technology A: Vacuum, Surfaces, and Films*, 11(4):1501, 1993. Cited on pages 4 and 18.
- [Ber87] S. Berg. Modeling of reactive sputtering of compound materials. *Journal of Vacuum Science & Technology A: Vacuum, Surfaces, and Films*, 5(2):202, 1987. Cited on page 20.
- [BGPM94] G. A. Battiston, R. Gerbasi, M. Porchia, and A. Marigo. Influence of substrate on structural properties of TiO2 thin films obtained via MOCVD. *Thin Solid Films*, 239(2):186–191, 1994. Cited on page 11.
- [BHM⁺87] J. K. Burdett, T. Hughbanks, G. J. Miller, J. W. Richardson, and J. V. Smith. Structural-electronic relationships in inorganic solids: powder neutron diffraction studies of the rutile and anatase polymorphs of titanium dioxide at 15 and 295 K. *Journal of the American Chemical Society*, 109(12):3639–3646, 1987. Cited on pages 11 and 96.
 - [BK99] S. Berg and I. V. Katardjiev. Preferential sputtering effects in thin film processing. *Journal of Vacuum Science & Technology A: Vacuum, Surfaces, and Films*, 17(4):1916, 1999. Cited on pages 25, 58, and 60.
- [BMD06] M. Batzill, E. Morales, and U. Diebold. Influence of Nitrogen Doping on the Defect Formation and Surface Properties of TiO2 Rutile and Anatase. *Physical Review Letters*, 96(2), 2006. Cited on page 13.
- [BMPF99] A. Billard, D. Mercs, F. Perry, and C. Frantz. Influence of the target temperature on a reactive sputtering process. *Surface and Coatings Technology*, 116-119:721–726, 1999. Cited on page 24.
- [BMT92] B. Baretzky, W. Möller, and E. Taglauer. Collision dominated preferential sputtering of tantalum oxide. *Vacuum*, 43(12):1207–1216, 1992. Cited on page 60.
 - [BN05] S. Berg and T. Nyberg. Fundamental understanding and modeling of reactive sputtering processes. *Thin Solid Films*, 476(2):215–230, 2005. Cited on pages 21 and 54.
 - [Bre24] J. Brentano. Focussing method of crystal powder analysis by X-rays. *Proceedings of the Physical Society of London*, 37(1):184–193, 1924. Cited on page 28.

- [BSN14] S. Berg, E. Särhammar, and T. Nyberg. Upgrading the "Berg-model" for reactive sputtering processes. *Thin Solid Films*, 2014. Cited on pages 21 and 23.
- [BSVB10] G. Bräuer, B. Szyszka, M. Vergöhl, and R. Bandorf. Magnetron sputtering Milestones of 30 years. *Vacuum*, 84(12):1354–1359, 2010. Cited on pages 3, 7, 9, and 12.
 - [CB00] C. Christou and Z. H. Barber. Ionization of sputtered material in a planar magnetron discharge. *Journal of Vacuum Science & Technology A: Vacuum, Surfaces, and Films*, 18(6):2897, 2000. Cited on pages 26 and 72.
- [CBBK93] P. Carlsson, S. Berg, A. Belkind, and I. Katardjiev. Serial cosputtering of metals: modelling of sputtering from a periodically codeposited surface. *Surface and Coatings Technology*, 61(1-3):287–292, 1993. Cited on pages 4 and 18.
- [CFH⁺07] T. L. Chen, Y. Furubayashi, Y. Hirose, T. Hitosugi, T. Shimada, and T. Hasegawa. Anatase phase stability and doping concentration dependent refractivity in codoped transparent conducting TiO2 films. *Journal of Physics D: Applied Physics*, 40(19):5961–5964, 2007. Cited on page 93.
 - [Cha98] J. Chase, M.W. NIST-JANAF Themochemical Tables, Fourth Edition. *J. Phys. Chem. Ref. Data*, Monograph 9:1–1951, 1998. Cited on page 11.
- [CHA+06] E. Cho, S. Han, H.-S. Ahn, K.-R. Lee, S. Kim, and C. Hwang. First-principles study of point defects in rutile TiO2–x. *Physical Review B*, 73(19), 2006. Cited on page 11.
 - [CHR04] O. Carp, C. Huisman, and A. Reller. Photoinduced reactivity of titanium dioxide. *Progress in Solid State Chemistry*, 32(1-2):33–177, 2004. Cited on page 12.
 - [Chr05] D. J. Christie. Target material pathways model for high power pulsed magnetron sputtering. *Journal of Vacuum Science & Technology A: Vacuum, Surfaces, and Films*, 23(2):330, 2005. Cited on pages 26, 53, and 66.
- [CHWL96] R. Y. Chau, W.-S. Ho, J. C. Wolfe, and D. L. Licon. Effect of target temperature on the reactive d.c.-sputtering of silicon and niobium oxides. *Thin Solid Films*, 287(1-2):57–64, 1996. Cited on page 24.
 - [CMN78] W.-K. Chu, J. W. Mayer, and M.-A. Nicolet. *Backscattering spectrometry*. Academic Press, New York, 1978. Cited on page 35.
 - [Cro95] K. Croswell. *The alchemy of the heavens: Searching for meaning in the Milky Way.* Anchor Books, New York, 1st edition, 1995. Cited on page 7.

- [CTP+07] J. O. Carneiro, V. Teixeira, A. Portinha, A. Magalhães, P. Coutinho, C. J. Tavares, and R. Newton. Iron-doped photocatalytic TiO2 sputtered coatings on plastics for self-cleaning applications. *Materials Science and Engineering: B*, 138(2):144–150, 2007. Cited on page 9.
 - [Cul78] B. D. Cullity. *Elements of x-ray diffraction*. Addison-Wesley series in metallurgy and materials. Addison-Wesley Pub. Co., Reading, Mass, 2nd edition, 1978. Cited on page 27.
 - [Cuo78] J. J. Cuomo. Significance of negative ion formation in sputtering and SIMS analysis. *Journal of Vacuum Science and Technology*, 15(2):281, 1978. Cited on page 78.
- [CWM84] J. D. Cox, D. D. Wagman, and V. A. Medvedev. CODATA Key Values for Thermodynamics. Hemisphere publishing corp., New York, 1st edition, 1984. Cited on page 11.
- [CWW47] W. F. Cole, A. D. Wadsley, and A. Walkley. An X-Ray Diffraction Study of Manganese Dioxide. *Transactions of The Electrochemical Society*, 92(1):133, 1947. Cited on page 96.
- [DCE⁺02] D. Depla, A. Colpaert, K. Eufinger, A. Segers, J. Haemers, and R. d. Gryse. Target voltage behaviour during DC sputtering of silicon in an argon/nitrogen mixture. *Vacuum*, 66(1):9–17, 2002. Cited on page 21.
- [DDA⁺01] N. Dubrovinskaia, L. Dubrovinsky, R. Ahuja, V. Prokopenko, V. Dmitriev, H.-P. Weber, J. Osorio-Guillen, and B. Johansson. Experimental and Theoretical Identification of a New High-Pressure TiO2 Polymorph. *Physical Review Letters*, 87(27), 2001. Cited on page 9.
 - [DDE96] M. S. Dresselhaus, G. Dresselhaus, and P. C. Eklund. *Science of fullerenes and carbon nanotubes: their properties and applications.* Academic Press, 1996. Cited on page 8.
 - [DG04] D. Depla and R. d. Gryse. Target poisoning during reactive magnetron sputtering: Part II: the influence of chemisorption and gettering. Surface and Coatings Technology, 183(2-3):190–195, 2004. Cited on page 60.
 - [DHG02] D. Depla, J. Haemers, and R. d. Gryse. Target surface condition during reactive glow discharge sputtering of copper. *Plasma Sources Science and Technology*, 11(1):91–96, 2002. Cited on page 21.

- [DHM⁺07] D. Depla, S. Heirwegh, S. Mahieu, J. Haemers, and R. d. Gryse. Understanding the discharge voltage behavior during reactive sputtering of oxides. *Journal of Applied Physics*, 101(1):013301, 2007. Cited on page 68.
 - [DK80] K. Danzmann and M. Kock. Oscillator strengths of Ti II from combined hook and emission measurements. *Journal of Physics B: Atomic and Molecular Physics*, 13(10):2051–2059, 1980. Cited on pages 38 and IX.
- [DKY⁺09] K. J. Dawson, K. L. Kearns, L. Yu, W. Steffen, and M. D. Ediger. Liquids and Structural Glasses Special Feature: Physical vapor deposition as a route to hidden amorphous states. *Proceedings of the National Academy of Sciences*, 106(36):15165–15170, 2009. Cited on page 75.
 - [DM08] D. Depla and S. Mahieu. *Reactive sputter deposition*. Springer, 2008. Cited on page 17.
 - [Don98] C. Donnet. Recent progress on the tribology of doped diamond-like and carbon alloy coatings: a review. *Surface and Coatings Technology*, 100-101:180–186, 1998. Cited on pages 3 and 9.
 - [Doo85] L. R. Doolittle. Algorithms for the rapid simulation of Rutherford backscattering spectra. *Nuclear Instruments and Methods in Physics Research Section B: Beam Interactions with Materials and Atoms*, 9(3):344–351, 1985. Cited on page 35.
 - [Dul84] E. Dullni. Velocity distributions of the metal atoms sputtered from oxygen and nitrogen covered Ti- and Al-surfaces. *Nuclear Instruments and Methods in Physics Research Section B: Beam Interactions with Materials and Atoms*, 2(1-3):610–613, 1984. Cited on page 24.
- [EASL11] S. El Mrabet, M. Abad, and J. Sánchez-López. Identification of the wear mechanism on WC/C nanostructured coatings. *Surface and Coatings Technology*, 206(7):1913–1920, 2011. Cited on page 8.
 - [ED06] A. Erdemir and C. Donnet. Tribology of diamond-like carbon films: recent progress and future prospects. *Journal of Physics D: Applied Physics*, 39(18):R311–R327, 2006. Cited on page 9.
- [EGK⁺98] J. Ensling, P. Gütlich, R. Klinger, W. Meisel, H. Jachow, and E. Schwab. Magnetic pigments for recording media. *Hyperfine Interactions*, 111(1/4):143–150, 1998. Cited on page 96.

- [Ein05] A. Einstein. Über einen die Erzeugung und Verwandlung des Lichtes betreffenden heuristischen Gesichtspunkt. Annalen der Physik, 322(6):132–148, 1905. Cited on page 36.
- [EKM00] J. O. Ekberg, R. Kling, and W. Mende. The Spectrum of Singly Ionized Tungsten, W II. *Physica Scripta*, 61(2):146–163, 2000. Cited on pages 72 and IX.
- [ENM⁺02] A. P. Ehiasarian, R. New, W.-D. Münz, L. Hultman, U. Helmersson, and V. Kouznetsov. Influence of high power densities on the composition of pulsed magnetron plasmas. *Vacuum*, 65(2):147–154, 2002. Cited on page 26.
 - [FE00] J. Fisher and T. A. Egerton. Titanium Compounds, Inorganic. In *Kirk-Othmer Encyclopedia of Chemical Technology*. John Wiley & Sons, Inc, Hoboken, NJ, USA, 2000. Cited on pages 9 and 11.
- [FFL⁺07] L. Fleming, C. C. Fulton, G. Lucovsky, J. E. Rowe, M. D. Ulrich, and J. Lüning. Local bonding analysis of the valence and conduction band features of TiO2. *Journal of Applied Physics*, 102(3):033707, 2007. Cited on page 10.
 - [FH72] A. Fujishima and K. Honda. Photolysis-decomposition of water at the surface of an irradiated semiconductor. *Nature*, 238(5385):37–38, 1972. Cited on page 9.
- [FHY⁺05] Y. Furubayashi, T. Hitosugi, Y. Yamamoto, K. Inaba, G. Kinoda, Y. Hirose, T. Shimada, and T. Hasegawa. A transparent metal: Nb-doped anatase TiO2. *Applied Physics Letters*, 86(25):252101, 2005. Cited on pages 3 and 12.
- [FKW⁺11] N. Farahani, P. Kelly, G. West, M. Ratova, C. Hill, and V. Vishnyakov. Photocatalytic activity of reactively sputtered and directly sputtered titania coatings. *Thin Solid Films*, 520(5):1464–1469, 2011. Cited on page 12.
 - [Fri72] E. Frieden. The Chemical Elements of Life. *Scientific American*, 227(1):52–60, 1972. Cited on page 7.
 - [GAH01] J. T. Gudmundsson, J. Alami, and U. Helmersson. Evolution of the electron energy distribution and plasma parameters in a pulsed magnetron discharge. *Applied Physics Letters*, 78(22):3427, 2001. Cited on pages 26 and 66.
 - [Gil11] G. Gilmore. *Practical gamma-ray spectroscopy*. John Wiley & Sons and Wiley, Hoboken, N.J, 2011. Cited on page 37.
 - [GK74] E. Giani and R. Kelly. A Study of SnO2 Thin Films Formed by Sputtering and by Anodizing. *Journal of The Electrochemical Society*, 121(3):394, 1974. Cited on page 96.

- [GM01] P. I. Gouma and M. J. Mills. Anatase-to-Rutile Transformation in Titania Powders. *Journal of the American Ceramic Society*, 84(3):619–622, 2001. Cited on pages 4, 12, and 13.
- [GP98] F. C. Gennari and D. M. Pasquevich. Kinetics of the anatase-rutile transformation in TiO2 in the presence of Fe2O3. *Journal of Materials Science*, 33(6):1571–1578, 1998. Cited on page 14.
- [Gra93] C. G. Granqvist. Transparent conductive electrodes for electrochromic devices: A review. *Applied Physics A Solids and Surfaces*, 57(1):19–24, 1993. Cited on pages 3 and 68.
- [GRCVV11] R. Gago, A. Redondo-Cubero, M. Vinnichenko, and L. Vázquez. Annealing of heterogeneous phase TiO2 films: An X-ray absorption and morphological study, 2011. Cited on page 77.
 - [GSC00] N. Golego, S. Studenikin, and M. Cocivera. Effect of oxygen on transient photoconductivity in thin-film $Nb_xTi_{1-x}O_2$. *Physical Review B*, 61(12):8262–8269, 2000. Cited on page 10.
- [GvD⁺07] M. A. Gillispie, M. F. van Hest, M. S. Dabney, J. D. Perkins, and D. S. Ginley. Sputtered Nb- and Ta-doped TiO2 transparent conducting oxide films on glass. *Journal of Materials Research*, 22(10):2832–2837, 2007. Cited on pages 12 and 68.
- [HDZ76] V. Henrich, G. Dresselhaus, and H. Zeiger. Observation of Two-Dimensional Phases Associated with Defect States on the Surface of TiO2. *Physical Review Letters*, 36(22):1335–1339, 1976. Cited on page 11.
- [HFU⁺05] T. Hitosugi, Y. Furubayashi, A. Ueda, K. Itabashi, K. Inaba, Y. Hirose, G. Kinoda, Y. Yamamoto, T. Shimada, and T. Hasegawa. Ta-doped Anatase TiO2 Epitaxial Film as Transparent Conducting Oxide. *Japanese Journal of Applied Physics*, 44(No. 34):L1063–L1065, 2005. Cited on page 12.
- [HLB⁺06] U. Helmersson, M. Lattemann, J. Bohlmark, A. P. Ehiasarian, and J. T. Gudmundsson. Ionized physical vapor deposition (IPVD): A review of technology and applications. *Thin Solid Films*, 513(1-2):1–24, 2006. Cited on pages 26, 53, and 66.
- [HMCB95] M. R. Hoffmann, S. T. Martin, W. Choi, and D. W. Bahnemann. Environmental Applications of Semiconductor Photocatalysis. *Chemical Reviews*, 95(1):69–96, 1995. Cited on page 11.

- [HNO⁺03] M. Hirano, C. Nakahara, K. Ota, O. Tanaike, and M. Inagaki. Photoactivity and phase stability of ZrO2-doped anatase-type TiO2 directly formed as nanometer-sized particles by hydrolysis under hydrothermal conditions. *Journal of Solid State Chemistry*, 170(1):39–47, 2003. Cited on pages 12, 76, and 83.
- [HOO⁺02] H. Hosono, H. Ohta, M. Orita, K. Ueda, and M. Hirano. Frontier of transparent conductive oxide thin films. *Vacuum*, 66(3-4):419–425, 2002. Cited on page 68.
 - [Hov88] P. E. Hovsepian. Influence of the parameters of the metal ion etching on the structure and the adhesion of TiN coatings deposited by the cathodic arc evaporation in vacuum. *Archives of Metallurgy and Materials*, 33(4):577–582, 1988. Cited on page 26.
 - [HRC88] W. Hume-Rothery and B. R. Coles. *Atomic theory for students of metallurgy,* volume 3 of *IOM facsimile reprints*. Institute of Metals and Institute of Metals North American Publications Center, London and Brookfield, VT, USA, 1988. Cited on page 13.
 - [HS11] D. A. H. Hanaor and C. C. Sorrell. Review of the anatase to rutile phase transformation. *Journal of Materials Science*, 46(4):855–874, 2011. Cited on pages 4, 9, 11, 13, 14, 15, 75, 76, 81, 83, 84, 85, 88, 92, 93, 96, and 97.
- [HUF⁺07] T. Hitosugi, A. Ueda, Y. Furubayashi, Y. Hirose, S. Konuma, T. Shimada, and T. Hasegawa. Fabrication of TiO2-based transparent conducting oxide films on glass by pulsed laser deposition. *Japanese Journal of Applied Physics*, 46(1-3):L86–L88, 2007. Cited on page 77.
 - [HW72] E. F. Heald and C. W. Weiss. Kinetics and mechanism of the anatase/rutile transformation, as catalyzed by ferric oxide and reducing conditions. *American Mineralogist*, 57(1-2):10–23, 1972. Cited on page 14.
- [HYH+08] N. L. H. Hoang, N. Yamada, T. Hitosugi, J. Kasai, S. Nakao, T. Shimada, and T. Hasegawa. Low-temperature Fabrication of Transparent Conducting Anatase Nb-doped TiO2 Films by Sputtering. Applied Physics Express, 1:115001, 2008. Cited on pages 12 and 77.
 - [IL09] H. Ibach and H. Lüth. *Festkörperphysik: Einführung in die Grundlagen*. Springer-Lehrbuch. Springer-Verlag, Berlin, 7th edition, 2009. Cited on pages 7, 8, and 30.
 - [Int28] Interferometer measurements of wave lengths in the vacuum arc spectra of titanium and other elements. Kiess, C. C. *Journal of Research of the National*

- *Institute of Standards and Technology*, 1(RP4):57–90, 1928. Cited on pages 38 and IX.
- [JLR⁺11] U. Jansson, E. Lewin, M. Råsander, O. Eriksson, B. André, and U. Wiklund. Design of carbide-based nanocomposite thin films by selective alloying. *Surface and Coatings Technology*, 206(4):583–590, 2011. Cited on page 9.
 - [JT37] H. A. Jahn and E. Teller. Stability of Polyatomic Molecules in Degenerate Electronic States. I. Orbital Degeneracy. *Proceedings of the Royal Society A: Mathematical, Physical and Engineering Sciences*, 161(905):220–235, 1937. Cited on page 10.
 - [KA00] P. Kelly and R. Arnell. Magnetron sputtering: a review of recent developments and applications. *Vacuum*, 56(3):159–172, 2000. Cited on pages 3, 7, 9, 12, and 17.
 - [Kar03] S. Karvinen. The effects of trace elements on the crystal properties of TiO2. *Solid State Sciences*, 5(5):811–819, 2003. Cited on pages 76 and 89.
- [KDH06] S. Konstantinidis, J. P. Dauchot, and M. Hecq. Titanium oxide thin films deposited by high-power impulse magnetron sputtering. *Thin Solid Films*, 515(3):1182–1186, 2006. Cited on pages 26 and 66.
- [KDM⁺08] T. Kubart, D. Depla, D. M. Martin, T. Nyberg, and S. Berg. High rate reactive magnetron sputter deposition of titanium oxide. *Applied Physics Letters*, 92(22):221501, 2008. Cited on pages 18, 45, and 64.
- [KFN⁺07] K.-N. P. Kumar, D. J. Fray, J. Nair, F. Mizukami, and T. Okubo. Enhanced anatase-to-rutile phase transformation without exaggerated particle growth in nanostructured titania–tin oxide composites. *Scripta Materialia*, 57(8):771–774, 2007. Cited on pages 76 and 89.
- [KFRS99] H. Kupfer, T. Flügel, F. Richter, and P. Schlott. Intrinsic stress in dielectric thin films for micromechanical components. *Surface and Coatings Technology*, 116–119(0):116–120, 1999. Cited on page 101.
- [KMS⁺99] V. Kouznetsov, K. Macák, J. M. Schneider, U. Helmersson, and I. Petrov. A novel pulsed magnetron sputter technique utilizing very high target power densities. Surface and Coatings Technology, 122(2-3):290–293, 1999. Cited on page 26.
 - [KN79] D. Kucharczyk and T. Niklewski. Accurate X-ray determination of the lattice parameters and the thermal expansion coefficients of VO2 near the transition

- temperature. *Journal of Applied Crystallography*, 12(4):370–373, 1979. Cited on page 96.
- [KNP+10] T. Kubart, T. Nyberg, A. Pflug, M. Siemers, M. Austgen, D. Koehl, M. Wuttig, and S. Berg. Modelling of sputtering yield amplification effect in reactive deposition of oxides. *Surface and Coatings Technology*, 204(23):3882–3886, 2010. Cited on page 49.
 - [Koc94] R. Koch. The intrinsic stress of polycrystalline and epitaxial thin metal films. *Journal of Physics: Condensed Matter*, 6(45):9519–9550, 1994. Cited on page 26.
- [KRRN13] A. Kramida, Y. Ralchenko, J. Reader, and NIST ASD Team. NIST Atomic Spectra Database (ver. 5.1, online): http://physics.nist.gov/asd, 2013. Cited on page IX.
- [KSA⁺12] T. Kubart, R. M. Schmidt, M. Austgen, T. Nyberg, A. Pflug, M. Siemers, M. Wuttig, and S. Berg. Modelling of sputtering yield amplification in serial reactive magnetron co-sputtering. *Surface and Coatings Technology*, 206(24):5055–5059, 2012. Cited on pages 4, 25, 47, 51, 53, and 101.
- [KVGA05] Y. Kudriavtsev, A. Villegas, A. Godines, and R. Asomoza. Calculation of the surface binding energy for ion sputtered particles. *Applied Surface Science*, 239(3-4):273–278, 2005. Cited on page 58.
- [LHM94] P. Löbl, M. Huppertz, and D. Mergel. Nucleation and growth in TiO2 films prepared by sputtering and evaporation. *Thin Solid Films*, 251(1):72–79, 1994. Cited on page 12.
 - [Lid97] D. R. Lide. *CRC handbook of chemistry and physics: A ready-reference book of chemical and physical data.* CRC Press, Boca Raton, Fla., 78. ed., 1997 1998 edition, 1997. Cited on pages 10, 11, 58, 63, 68, and 96.
- [LKR89] Y. Lifshitz, S. Kasi, and J. Rabalais. Subplantation model for film growth from hyperthermal species: Application to diamond. *Physical Review Letters*, 62(11):1290–1293, 1989. Cited on page 26.
 - [LL05] M. A. Lieberman and A. J. Lichtenberg. *Principles of plasma discharges and materials processing.* John Wiley & Sons, 2005. Cited on page 68.
- [LLBGW05] G. Li, L. Li, J. Boerio-Goates, and B. F. Woodfield. High Purity Anatase TiO2 Nanocrystals: Near Room-Temperature Synthesis, Grain Growth Kinetics, and Surface Hydration Chemistry. *Journal of the American Chemical Society*, 127(24):8659–8666, 2005. Cited on page 12.

- [LLY95] A. L. Linsebigler, G. Lu, and J. T. Yates. Photocatalysis on TiO2 Surfaces: Principles, Mechanisms, and Selected Results. *Chemical Reviews*, 95(3):735–758, 1995. Cited on pages 9, 10, and 11.
- [LRS12] M. Landmann, E. Rauls, and W. G. Schmidt. The electronic structure and optical response of rutile, anatase and brookite TiO2. *Journal of Physics: Condensed Matter*, 24(19):195503, 2012. Cited on page 9.
- [LZF⁺05] J. Lopez, W. Zhu, A. Freilich, A. Belkind, and K. Becker. Time-resolved optical emission spectroscopy of pulsed DC magnetron sputtering plasmas. *Journal of Physics D: Applied Physics*, 38(11):1769–1780, 2005. Cited on page 38.
- [LZZ⁺00] C. Li, Z. Zheng, F. Zhang, S. Yang, H. Wang, L. Chen, F. Zhang, X. Wang, and X. Liu. TiO2–x films prepared by ion beam assisted deposition. *Nuclear Instruments and Methods in Physics Research Section B: Beam Interactions with Materials and Atoms*, 169(1-4):21–25, 2000. Cited on page 12.
- [Mac75] K. J. Mackenzie. The Calcination of Titania: IV. The Effect of Additives on the Anatase-Rutile Transformation. *Transactions and Journal of the British Ceramic Society*, 74(2):29–34, 1975. Cited on pages 4, 13, 75, 76, 77, and 89.
- [Mat87] R. W. Matthews. Photooxidation of organic impurities in water using thin films of titanium dioxide. *The Journal of Physical Chemistry*, 91(12):3328–3333, 1987. Cited on page 9.
- [MBE+00] D. Mergel, D. Buschendorf, S. Eggert, R. Grammes, and B. Samset. Density and refractive index of TiO2 films prepared by reactive evaporation. *Thin Solid Films*, 371(1-2):218–224, 2000. Cited on page 11.
 - [MC95] S.-D. Mo and W. Ching. Electronic and optical properties of three phases of titanium dioxide: Rutile, anatase, and brookite. *Physical Review B*, 51(19):13023–13032, 1995. Cited on pages 9 and 11.
 - [MD01] D. S. Muggli and L. Ding. Photocatalytic performance of sulfated TiO2 and Degussa P-25 TiO2 during oxidation of organics. *Applied Catalysis B: Environmental*, 32(3):181–194, 2001. Cited on page 9.
 - [MEB88] W. Möller, W. Eckstein, and J. P. Biersack. Tridyn-binary collision simulation of atomic collisions and dynamic composition changes in solids. *Computer Physics Communications*, 51(3):355–368, 1988. Cited on page 49.

- [MG07] W. Möller and D. Güttler. Modeling of plasma-target interaction during reactive magnetron sputtering of TiN. *Journal of Applied Physics*, 102(9):094501, 2007. Cited on page 49.
- [MHL05] A. Mills, S. Hodgen, and S. K. Lee. Self-cleaning titania films: an overview of direct, lateral and remote photo-oxidation processes. *Research on Chemical Intermediates*, 31(4-6):295–308, 2005. Cited on page 9.
- [MHS86] J. B. Malherbe, S. Hofmann, and J. M. Sanz. Preferential sputtering of oxides: A comparison of model predictions with experimental data. *Applied Surface Science*, 27(3):355–365, 1986. Cited on page 63.
- [MHŠ06] J. Musil, D. Heřman, and J. Šícha. Low-temperature sputtering of crystalline TiO2 films. *Journal of Vacuum Science & Technology A: Vacuum, Surfaces, and Films*, 24(3):521, 2006. Cited on page 12.
- [MLP⁺99] D. Mercs, F. Lapostolle, F. Perry, A. Billard, and C. Frantz. Enhanced deposition rate of high quality stoichiometric ceramic compounds reactively sputter deposited at low pressure by modulating the discharge current at low frequency. *Surface and Coatings Technology*, 116-119:916–921, 1999. Cited on page 24.
- [MNK⁺00] M. Mikami, S. Nakamura, O. Kitao, H. Arakawa, and X. Gonze. First-Principles Study of Titanium Dioxide: Rutile and Anatase. *Japanese Journal of Applied Physics*, 39(Part 2, No. 8B):L847–L850, 2000. Cited on page 10.
 - [Mos13] H. G. Moseley. High-frequency spectra of the elements. *Philosophical Magazine*, 26:1024–1034, 1913. Cited on page 36.
 - [MPB06] D. Mercs, F. Perry, and A. Billard. Hot target sputtering: A new way for high-rate deposition of stoichiometric ceramic films. Surface and Coatings Technology, 201(6):2276–2281, 2006. Cited on page 24.
 - [MR99] N. Martin and C. Rousselot. Modelling of reactive sputtering processes involving two separated metallic targets. *Surface and Coatings Technology*, 114(2-3):235–249, 1999. Cited on pages 18 and 99.
 - [MRS04] S. Mahanty, S. Roy, and S. Sen. Effect of Sn doping on the structural and optical properties of sol–gel TiO2 thin films. *Journal of Crystal Growth*, 261(1):77–81, 2004. Cited on pages 77, 89, and 93.
 - [MS11] S. Mraz and J. M. Schneider. Structure evolution of magnetron sputtered TiO2 thin films. *Journal of Applied Physics*, 109(2):023512, 2011. Cited on pages 77 and 83.

- [MSH02] J. Muscat, V. Swamy, and N. Harrison. First-principles calculations of the phase stability of TiO2. *Physical Review B*, 65(22), 2002. Cited on page 9.
- [MTDR00] D. Mardare, M. Tasca, M. Delibas, and G. Rusu. On the structural properties and optical transmittance of TiO2 r.f. sputtered thin films. *Applied Surface Science*, 156(1-4):200–206, 2000. Cited on page 77.
 - [Mül86] K.-H. Müller. Model for ion-assisted thin-film densification. *Journal of Applied Physics*, 59(8):2803, 1986. Cited on pages 50 and 102.
- [MWC06] A. Mills, J. Wang, and M. Crow. Photocatalytic oxidation of soot by P25 TiO2 films. *Chemosphere*, 64(6):1032–1035, 2006. Cited on page 9.
 - [MY06] H. Miyazaki and I. Yasui. Substrate bias effect on the fabrication of thermochromic VO2 films by reactive RF sputtering. *Journal of Physics D: Applied Physics*, 39(10):2220–2223, 2006. Cited on page 96.
- [NKMW04] J. M. Ngaruiya, O. Kappertz, S. H. Mohamed, and M. Wuttig. Structure formation upon reactive direct current magnetron sputtering of transition metal oxide films. *Applied Physics Letters*, 85(5):748, 2004. Cited on pages 60 and 78.
- [NMD+12] C. Nouvellon, M. Michiels, J. P. Dauchot, C. Archambeau, F. Laffineur, E. Silberberg, S. Delvaux, R. Cloots, S. Konstantinidis, and R. Snyders. Deposition of titanium oxide films by reactive High Power Impulse Magnetron Sputtering (HiPIMS): Influence of the peak current value on the transition from metallic to poisoned regimes. *Surface and Coatings Technology*, 206(16):3542–3549, 2012. Cited on page 68.
 - [Nor73] G. Norlén. Wavelengths and Energy Levels of Ar I and Ar II based on New Interferometric Measurements in the Region 3 400-9 800 Å. *Physica Scripta*, 8(6):249–268, 1973. Cited on pages 38 and IX.
 - [Nov04] K. S. Novoselov. Electric Field Effect in Atomically Thin Carbon Films. *Science*, 306(5696):666–669, 2004. Cited on page 7.
- [NPSK⁺06] S. Na-Phattalung, M. Smith, K. Kim, M.-H. Du, S.-H. Wei, S. Zhang, and S. Limpijumnong. First-principles study of native defects in anatase TiO2. *Physical Review B*, 73(12), 2006. Cited on page 11.
 - [NTL⁺11] N. Nedfors, O. Tengstrand, E. Lewin, A. Furlan, P. Eklund, L. Hultman, and U. Jansson. Structural, mechanical and electrical-contact properties of

- nanocrystalline-NbC/amorphous-C coatings deposited by magnetron sputtering. *Surface and Coatings Technology*, 206(2-3):354–359, 2011. Cited on page 9.
- [OJL97] S. K. O'Leary, S. R. Johnson, and P. K. Lim. The relationship between the distribution of electronic states and the optical absorption spectrum of an amorphous semiconductor: An empirical analysis. *Journal of Applied Physics*, 82(7):3334, 1997. Cited on page 32.
- [Oka10] H. Okamoto. Bi-Ti (Bismuth-Titanium). *Journal of Phase Equilibria and Diffusion*, 31(3):314–315, 2010. Cited on page 18.
- [OTM⁺01] H. Ohsaki, Y. Tachibana, A. Mitsui, T. Kamiyama, and Y. Hayashi. High rate deposition of TiO2 by DC sputtering of the TiO2–X target. *Thin Solid Films*, 392(2):169–173, 2001. Cited on page 18.
 - [Our03] K. Oura. *Surface science: An introduction*. Advanced texts in physics. Springer, Berlin and New York, 2003. Cited on page 34.
 - [Pau01] Y. Pauleau. Generation and evolution of residual stresses in physical vapour-deposited thin films. *Vacuum*, 61(2-4):175–181, 2001. Cited on page 26.
 - [PBC97] R. L. Pozzo, M. A. Baltanás, and A. E. Cassano. Supported titanium oxide as photocatalyst in water decontamination: State of the art. *Catalysis Today*, 39(3):219–231, 1997. Cited on page 9.
- [PBHG03] I. Petrov, P. B. Barna, L. Hultman, and J. E. Greene. Microstructural evolution during film growth. *Journal of Vacuum Science & Technology A: Vacuum, Surfaces, and Films*, 21(5):S117, 2003. Cited on page 26.
- [PCKK99] S. D. Park, Y. H. Cho, W. W. Kim, and S.-J. Kim. Understanding of Homogeneous Spontaneous Precipitation for Monodispersed TiO2 Ultrafine Powders with Rutile Phase around Room Temperature. *Journal of Solid State Chemistry*, 146(1):230–238, 1999. Cited on page 12.
 - [PH97] Y. Paz and A. Heller. Photo-oxidatively self-cleaning transparent titanium dioxide films on soda lime glass: The deleterious effect of sodium contamination and its prevention. *Journal of Materials Research*, 12(10):2759–2766, 1997. Cited on pages 3 and 9.
 - [Pis76] C. W. Pistorius. Phase relations and structures of solids at high pressures. *Progress in Solid State Chemistry*, 11:1–151, 1976. Cited on page 9.

- [PTP01] J. C. Pickering, A. P. Thorne, and R. Perez. Oscillator Strengths of Transitions in Ti II in the Visible and Ultraviolet regions. *The Astrophysical Journal Supplement Series*, 132(2):403–409, 2001. Cited on pages 71 and IX.
- [Ren00] R. Ren. Polymorphic transformation and powder characteristics of TiO2 during high energy milling. *Journal of Materials Science*, 35(23):6015–6026, 2000. Cited on page 9.
- [Ric04] B. S. Richards. Comparison of TiO2 and other dielectric coatings for buried-contact solar cells: a review. *Progress in Photovoltaics: Research and Applications*, 12(4):253–281, 2004. Cited on page 30.
- [RKBM05] D. Rosén, I. Katardjiev, S. Berg, and W. Möller. TRIDYN simulation of target poisoning in reactive sputtering. *Nuclear Instruments and Methods in Physics Research Section B: Beam Interactions with Materials and Atoms*, 228(1-4):193–197, 2005. Cited on page 21.
 - [RKD07] S. Riyas, G. Krishnan, and Das, P. N. Mohan. Anatase–rutile transformation in doped titania under argon and hydrogen atmospheres. *Advances in Applied Ceramics*, 106(5):255–264, 2007. Cited on page 13.
- [RLS⁺03] A. Rothschild, A. Levakov, Y. Shapira, N. Ashkenasy, and Y. Komem. Surface photovoltage spectroscopy study of reduced and oxidized nanocrystalline TiO2 films. *Surface Science*, 532-535:456–460, 2003. Cited on page 12.
- [Rob91] J. Robertson. Hard amorphous (diamond-like) carbons. *Progress in Solid State Chemistry*, 21(4):199–333, 1991. Cited on page 8.
 - [RS25] H. N. Russell and F. A. Saunders. New Regularities in the Spectra of the Alkaline Earths. *The Astrophysical Journal*, 61:38, 1925. Cited on page IX.
- [RSSG69] D. B. Rogers, R. D. Shannon, A. W. Sleight, and J. L. Gillson. Crystal chemistry of metal dioxides with rutile-related structures. *Inorganic Chemistry*, 8(4):841–849, 1969. Cited on page 96.
 - [Rut11] E. Rutherford. The scattering of α and β particles by matter and the structure of the atom. *The London, Edinburgh, and Dublin Philosophical Magazine and Journal of Science*, 21(125):669–688, 1911. Cited on page 34.
 - [Rut12] E. Rutherford. The scattering of α and β particles by matter and the structure of the atom. *Philosophical Magazine*, 92(4):379–398, 2012. Cited on page 34.

- [RVC75] J. R. Roberts, P. A. Voigt, and A. Czernichowski. Experimentally Determined Absolute Oscillator Strengths of Ti I, Ti II, and Ti III. *The Astrophysical Journal*, 197:791, 1975. Cited on pages 71 and IX.
- [Saf00] I. Safi. Recent aspects concerning DC reactive magnetron sputtering of thin films: a review. *Surface and Coatings Technology*, 127(2–3):203–218, 2000. Cited on page 17.
- [SAK10] K. Sarakinos, J. Alami, and S. Konstantinidis. High power pulsed magnetron sputtering: A review on scientific and engineering state of the art. *Surface and Coatings Technology*, 204(11):1661–1684, 2010. Cited on pages 26 and 70.
- [SBZ⁺12] K. Sarakinos, A. Braun, C. Zilkens, S. Mráz, J. Schneider, H. Zoubos, and P. Patsalas. Exploring the potential of high power impulse magnetron sputtering for growth of diamond-like carbon films. *Surface and Coatings Technology*, 206(10):2706–2710, 2012. Cited on page 9.
- [SCGG05] M. P. Seah, C. A. Clifford, F. M. Green, and I. S. Gilmore. An accurate semiempirical equation for sputtering yields I: for argon ions. *Surface and Interface Analysis*, 37(5):444–458, 2005. Cited on page 76.
 - [Sch12] A. P. Schulz. *Interface Dipole Formation in Organic Surface Functionalizations: Tailoring Metal Contacts for Organic Optoelectronic Devices.* PhD thesis, RWTH
 Aachen University, 21.05.2012. Cited on page 37.
- [SDG+12] B. Szyszka, W. Dewald, S. K. Gurram, A. Pflug, C. Schulz, M. Siemers, V. Sittinger, and S. Ulrich. Recent developments in the field of transparent conductive oxide films for spectral selective coatings, electronics and photovoltaics. *Current Applied Physics*, 12:S2–S11, 2012. Cited on pages 26 and 68.
 - [Ser06] N. Serpone. Is the Band Gap of Pristine TiO2 Narrowed by Anion- and Cation-Doping of Titanium Dioxide in Second-Generation Photocatalysts? *The Journal of Physical Chemistry B*, 110(48):24287–24293, 2006. Cited on page 13.
 - [Sha76] R. D. Shannon. Revised effective ionic radii and systematic studies of interatomic distances in halides and chalcogenides. *Acta Crystallographica Section A*, 32(5):751–767, 1976. Cited on pages 14, 84, and 92.
- [SKK⁺06] D. Severin, O. Kappertz, T. Kubart, T. Nyberg, S. Berg, A. Pflug, M. Siemers, and M. Wuttig. Process stabilization and increase of the deposition rate in reactive sputtering of metal oxides and oxynitrides. *Applied Physics Letters*, 88(16):161504, 2006. Cited on page 24.

- [SL13] H. A. Schaeffer and R. Langfeld. Werkstoff Glas: Alter Werkstoff mit großer Zukunft. Technik im Fokus. Springer Vieweg, first edition, 2013. Cited on pages 4, 13, and 41.
- [Son52] E. H. Sondheimer. The mean free path of electrons in metals. *Advances in Physics*, 1(1):1–42, 1952. Cited on page 37.
- [SP65] R. D. Shannon and J. A. Pask. Kinetics of the Anatase-Rutile Transformation. *Journal of the American Ceramic Society*, 48(8):391–398, 1965. Cited on pages 4, 10, 12, 13, 75, 76, 89, and 92.
- [Spi08] L. Spieß. *Moderne Röntgenbeugung: Röntgendiffraktometrie für Materialwissenschaftler, Physiker und Chemiker*. Studium. Teubner, Wiesbaden, 2nd edition, 2008. Cited on page 30.
- [SPSU10] B. Szyszka, A. Pflug, V. Sittinger, and S. Ulrich. Sputteryield-Amplification. *Vakuum in Forschung und Praxis*, 22(3):15–17, 2010. Cited on pages 4, 18, and 53.
- [SQW⁺08] V. Straňák, M. Quaas, H. Wulff, Z. Hubička, S. Wrehde, M. Tichý, and R. Hippler. Formation of TiOx films produced by high-power pulsed magnetron sputtering. *Journal of Physics D: Applied Physics*, 41(5):055202, 2008. Cited on page 12.
- [SREF09] G. P. Singh, S. Ram, J. Eckert, and H.-J. Fecht. Synthesis and morphological stability in CrO2 single crystals of a half-metallic ferromagnetic compound. *Journal of Physics: Conference Series*, 144:012110, 2009. Cited on page 96.
- [SRP+14] R. M. Schmidt, P. Ries, A. Pflug, M. Wuttig, and T. Kubart. Increasing the carbon deposition rate using sputter yield amplification upon serial magnetron co-sputtering. *Surface and Coatings Technology*, 252:74–78, 2014. Cited on pages 9, 45, and 101.
- [SRW⁺08] V. Sittinger, F. Ruske, W. Werner, C. Jacobs, B. Szyszka, and D. J. Christie. High power pulsed magnetron sputtering of transparent conducting oxides. *Thin Solid Films*, 516(17):5847–5859, 2008. Cited on pages 26 and 68.
 - [SS99] K. N. Stoev and K. Sakurai. Review on grazing incidence X-ray spectrometry and reflectometry. Spectrochimica Acta Part B: Atomic Spectroscopy, 54(1):41– 82, 1999. Cited on page 27.
 - [SSR96] C. J. Sansonetti, M. L. Salit, and J. Reader. Wavelengths of spectral lines in mercury pencil lamps. *Applied optics*, 35(1):74–77, 1996. Cited on pages 39 and IX.

- [TFM⁺07] A. Thomas, W. Flavell, A. Mallick, A. Kumarasinghe, D. Tsoutsou, N. Khan, C. Chatwin, S. Rayner, G. Smith, R. Stockbauer, S. Warren, T. Johal, S. Patel, D. Holland, A. Taleb, and F. Wiame. Comparison of the electronic structure of anatase and rutile TiO2 single-crystal surfaces using resonant photoemission and x-ray absorption spectroscopy. *Physical Review B*, 75(3), 2007. Cited on page 11.
 - [The12] W. Theiss. *CODE Technical Manual*. W.Theiss Hard- and Software for Optical Spectroscopy, 2012. Cited on page 31.
 - [TI05] H. Tompkins and E. A. Irene. *Handbook of ellipsometry*. William Andrew, 2005. Cited on page 30.
 - [TM99] H. G. Tompkins and W. A. McGahan. *Spectroscopic ellipsometry and reflectom-etry: A user's guide.* Wiley, New York, 1999. Cited on page 30.
- [TPD+02] H. Tomaszewski, H. Poelman, D. Depla, D. Poelman, R. d. Gryse, L. Fiermans, M.-F. Reyniers, G. Heynderickx, and G. B. Marin. TiO2 films prepared by DC magnetron sputtering from ceramic targets. *Vacuum*, 68(1):31–38, 2002. Cited on page 77.
 - [TPP88] S. Tanuma, C. J. Powell, and D. R. Penn. Calculations of electron inelastic mean free paths for 31 materials. *Surface and Interface Analysis*, 11(11):577–589, 1988. Cited on page 37.
- [TPS⁺94] H. Tang, K. Prasad, R. Sanjinès, P. E. Schmid, and F. Lévy. Electrical and optical properties of TiO2 anatase thin films. *Journal of Applied Physics*, 75(4):2042, 1994. Cited on pages 3 and 11.
- [VVv⁺99] T. Vandevelde, K. Vandierendonck, M. van Stappen, W. Du Mong, and P. Perremans. Cutting applications of DLC, hard carbon and diamond films. *Surface and Coatings Technology*, 113(1-2):80–85, 1999. Cited on pages 3 and 9.
- [WAC⁺95] W. Whaling, W. Anderson, M. T. Carle, J. W. Brault, and H. A. Zarem. Argon ion linelist and level energies in the hollow-cathode discharge. *Journal of Quantitative Spectroscopy and Radiative Transfer*, 53(1):1–22, 1995. Cited on pages 71 and IX.
 - [Wag11] D. Wagner. *unpublished data*. RWTH Aachen University, 2011. Cited on page 71.
 - [Wei02] H. Weis. *Untersuchung gasochrom schaltender Wolframoxide*. PhD thesis, RWTH Aachen University, Aachen, 2002. Cited on pages 27, 28, and 32.

- [Wik06] Wikimedia Commons, User:Sven. Sp3-Orbital.svg & Sp2-Orbital.svg: CC BY-SA 3.0 (http://creativecommons.org/licenses/by-sa/3.0), 2006. Cited on page 8.
- [WL06] H. Wang and J. P. Lewis. Second-generation photocatalytic materials: anion-doped TiO2. *Journal of Physics: Condensed Matter*, 18(2):421–434, 2006. Cited on page 11.
- [Wol93] A. Wold. Photocatalytic properties of titanium dioxide (TiO2). *Chemistry of Materials*, 5(3):280–283, 1993. Cited on pages 9 and 11.
- [WYMZ97] Z. L. Wang, J. S. Yin, W. D. Mo, and Z. J. Zhang. In-Situ Analysis of Valence Conversion in Transition Metal Oxides Using Electron Energy-Loss Spectroscopy. *The Journal of Physical Chemistry B*, 101(35):6793–6798, 1997. Cited on pages 14 and 93.
 - [Yat11] A. K. Yatim. *Electronic Properties of Titanium Dioxide under UV Illumination*. PhD thesis, RWTH Aachen University, 2011. Cited on page 11.
- [YHK⁺09] N. Yamada, T. Hitosugi, J. Kasai, N. L. H. Hoang, S. Nakao, Y. Hirose, T. Shimada, and T. Hasegawa. Direct growth of transparent conducting Nb-doped anatase TiO2 polycrystalline films on glass. *Journal of Applied Physics*, 105(12):–, 2009. Cited on pages 12 and 68.
 - [ZB98] H. Zhang and J. F. Banfield. Thermodynamic analysis of phase stability of nanocrystalline titania. *Journal of Materials Chemistry*, 8(9):2073–2076, 1998. Cited on pages 11 and 12.
- [ZMS⁺04] O. Zywitzki, T. Modes, H. Sahm, P. Frach, K. Goedicke, and D. Glöß. Structure and properties of crystalline titanium oxide layers deposited by reactive pulse magnetron sputtering. *Surface and Coatings Technology*, 180-181:538–543, 2004. Cited on page 11.
 - [ZR02] Y.-H. Zhang and A. Reller. Phase transformation and grain growth of doped nanosized titania. *Materials Science and Engineering: C*, 19(1-2):323–326, 2002. Cited on pages 76 and 89.
 - [ZT02] P. Zeman and S. Takabayashi. Self-cleaning and antifogging effects of TiO2 films prepared by radio frequency magnetron sputtering. *Journal of Vacuum Science* & *Technology A: Vacuum, Surfaces, and Films*, 20(2):388, 2002. Cited on page 12.

List of Figures

2.1	Schematic sketch of the sp^3 - and sp^2 -hybridization of carbon	8
2.2	Crystal structure of rutile and anatase $\text{Ti}O_2$	10
2.3	Dopants of TiO_2 plotted as a function of valence and ionic radius $\ldots \ldots$	14
2.4	Summary of the influence of dopants on the TiO_2 phase transformation $\ \ .\ \ .\ \ .$	15
3.1	Phase diagram of Bi-Ti	18
3.2	Schematic of the principle of serial co-sputtering	19
3.3	Mechanisms and fluxes considered altering surface and bulk composition $\ \ldots$	23
4.1	Schematic of beam path and corresponding angles in an X-ray setup	28
4.2	Example of measured and simulated optical data of an undoped $\text{TiO}_2 \ \text{film} \ \ . \ \ .$	33
4.3	RBS spectrum of a TiO $_2$:Ta film on a silicon substrate \ldots	35
4.4	Optical emission spectra of DC and HiPIMS sputtered TiO_2 in Ar	38
4.5	Timings in accumulated digital direct gate (DDG) mode	39
5.1	Total deposition rate of carbon as a function of the auxiliary power	46
5.2	Dopant content of the sputtered films as a function of the auxiliary power $\ \ . \ \ .$	48
5.3	Density of doped carbon films as a function of dopant concentration	50
5.4	Rate enhancement factor and sputter yield amplification factor of carbon	52
6.1	O_2 partial pressure hysteresis shift upon doping of TiO_2 with Ta	54
6.2	Deposition rate, dopant content and rate enhancement of $\text{TiO}_2\text{:W}\ldots\ldots$	56
6.3	Rate enhancement as a function of dopant content	57
6.4	Rate enhancement of TiO_2 as a function of O_2 flow and dopant concentration .	59
6.5	O_2 partial pressure and voltage hysteresis of $\text{Ti}O_2$ for different dopants $\ \ldots \ \ldots$	61
6.6	Target voltage hysteresis evolution of TiO_2 upon Zr doping $\ldots \ldots \ldots$	62
6.7	Refractive index evolution of ${\rm TiO_2}$ upon doping with heavy elements $\ \ \ldots \ \ \ldots$	65
6.8	O ₂ partial pressure and voltage hysteresis of HiPIMS sputtered TiO ₂	67

List of Figures

6.9	Deposition rates of HiPIMS sputtered TiO_2 as a function of O_2 flow	69
6.10	Comparison of sputter yield amplification factors in DC and HiPIMS $$	70
6.11	Voltage evolution upon sputter cleaning after using HiPIMS and DC	71
6.12	Evolution of optical emission spectra of HiPIMS and DC sputtered Ti:W	73
7.1	Dopant concentrations of serial co-sputtered TiO_2 thin films $\ldots \ldots \ldots$	77
7.2	GI-XRD measurements of as-deposited ${\rm TiO_2}$ with ART-inhibiting dopants $$	79
7.3	GI-XRD measurements of as-deposited TiO_2 with ART-promoting dopants	80
7.4	GI-XRD measurements of TiO $_2$ ann. at 300 $^{\circ}\text{C}$ with ART-inhibiting dopants $$. $$.	82
7.5	Peak heights of TiO_2 annealed at 300 °C with ART-inhibiting dopants $\ldots \ldots$	83
7.6	RBS measurements of TiO_2 with different dopants $\ \ \ldots \ \ \ldots \ \ \ldots \ \ \ldots$	86
7.7	GI-XRD measurements of TiO_2 ann. at 700 °C with ART-inhibiting dopants	87
7.8	Peak heights of TiO $_2$ annealed at 700 °C with ART-inhibiting dopants $\ \ \ldots \ \ \ldots$	88
7.9	GI-XRD measurements of TiO $_2$ ann. at 300 $^{\circ}\text{C}$ with ART-promoting dopants $$	90
7.10	Peak heights of TiO_2 annealed at 300 °C with ART-promoting dopants	91
7.11	GI-XRD measurements of TiO $_2$ ann. at 700 $^{\circ}\text{C}$ with ART-promoting dopants $$	94
7.12	Peak heights of TiO_2 annealed at 700 °C with ART-promoting dopants $\ \ldots \ \ldots$	95
8.1	Schematic of sputtering TiO ₂ using the print target concept	100
8.2	XPS stoichiometry measurements of TiO ₂ sputtered via carbon print target	103

List of Tables

2.1	Overview of the main properties of anatase and rutile TiO_2
4.1	Settings used for optical emission spectroscopy of TiO_2 40
5.1	Material constants used in TRIDYN model
6.1	Comparison of atomic mass, density and SBE of Hf, Ta, W, Pb and Bi 58
6.2	Properties of metal oxides formed upon doping of TiO_2
7.1	Comparison of ionic radii in sixfold coordination of ART-inhibiting dopants 84
7.2	$Comparison\ of\ ionic\ radii\ in\ sixfold\ coordination\ of\ ART-promoting\ dopants\ .\ .\ 92$
7.3	Comparison of rutile structures of different materials
8.1	Deposition rates of carbon sputtered in Ar/O ₂ atmosphere 101
8.2	Determined thicknesses of TiO_2 sputtered using the carbon print target 102
B.1	Density and deposition rates of different dopants onto the rotating target VII
C.1	Spectral emission lines assigned within this work

Acknowledgements

An ambitious work like this would not be possible without the aid of many others. I would like to thank everyone who contributed to this work, either scientifically or in any other way, but some people especially:

First, I would like to thank my thesis adviser Matthias Wuttig for the opportunity to work in the sputter group of the I. Institute of Physics at RWTH Aachen University. I enjoyed the work in his group, particularly the versatile challenges, tasks and projects. I am really grateful for his guidance and support, the rights and freedom I was granted during my time at the institute as well as the trust he placed in me.

My thank goes also to Peter Kelly, the second adviser of this work, who I first met at the RSD conference in Linköping. A short time later, I was given the opportunity to work with his group in Manchester, where I had a warm welcome and an instructive as well as entertaining stay. Additionally, I enjoyed fruitful discussions with him about science and life on several occasions.

During my time at the institute I supervised several bachelor and master students. Among them Sebastian Mäder stands out, who worked with me as a bachelor student, research assistant and lately in terms of writing his master's thesis. During his time in our group he always offered a helping hand and supported me by performing measurements and depositions. I am very grateful for the time in which I worked with him and wish him the best for his ongoing time as a PhD student at the institute. Additionally, I am grateful to Anton Neumann, who supported me with several measurements during the last weeks, which was a great help in this busy time.

I would like to thank Stephan Hermes and Sebastian Mohrhenn for a fast and efficient support regarding vacuum and lab equipment as well as Sarah Schlenter and Ralf Detemple for a simple management of several equipment orders. Additionally, I would like to thank them for many informative and cheerful discussions.

The refurbishment of our sputter lab would not have been successful without the knowledge and skills of Axel Gross, Sebastian Arendt and Franz Josef Neus regarding any kind of electronics. With their help the development of a state-of-the art lab equipment was possible as well as a fulfilling task. I would also like to thank Michael Wlochal, Karl-Heinz Dreger and Gert Kirchoff, representative for all members of the mechanical workshop, for their help with any kind of construction tasks.

Besides the people from the I. Institute of Physics at the RWTH Aachen University, I am very grateful to several people from other research facilities as well, especially Tomas Kubart from Uppsala University, who performed the computer simulations, and Andreas Pflug from the Fraunhofer IST for their help and support within and also after the COSMOS project. My thank also goes to Bernhard Holländer from the Forschungszentrum Jülich, who assisted me with the RBS measurements and analysis. I enjoyed the fruitful cooperation and valuable discussions in our joint work.

I enjoyed working with all the people at the I. Institute of Physics at the RWTH Aachen and I am thankful for the time I spent with them, and I would like to thank particularly Matthias Kaes, Felix Lange, Dominik Meyer, Daniel Mokros, Patrick Ries and Martin Wimmer for any kind of help, patience, fruitful discussions, advice as well as their friendship.

I would also like to thank my family and my friends for their help and support, especially Achim Gottwald for proofreading of this thesis.

My biggest thanks go to Stefanie Karpinski for her patience, love and support, who believed in me all the time.

Curriculum Vitae

Personal data

Name	Rüdiger Matti Schmidt
Date of Birth	February 27 th , 1986
Place of Birth	Münster
Nationality	German

Education

2011 – 2014	PhD Student, I. Institute of Physics, RWTH Aachen University
2005 - 2010	Study of Physics, RWTH Aachen University
	With emphasis on Condensed Matter
	Diplom (very good)
1996 - 2005	Kardinal von Galen Gymnasium, Münster-Hiltrup
	Abitur (general qualification for university entrance, 1.7)
1992 - 1996	Kardinal von Galen Grundschule, Drensteinfurt

Reviewed papers

- ♦ R.M. Schmidt, P. Ries, A. Pflug, M. Wuttig, T. Kubart, *Increasing the carbon deposition rate using sputter yield amplification upon serial magnetron co-sputtering*, Surf. Coat. Technol. 252, 74 (2014)
- ♦ T. Leichtweiss, R.A. Henning, J. Koettgen, **R.M. Schmidt**, B. Hollaender, M. Martin, M. Wuttig, J. Janek, J. *Amorphous and Highly Nonstoichiometric Titania (TiOx) Thin Films close to Metal-like Conductivity*, J. Mater. Chem. A 2, 6631 (2014)
- J. Luckas, A. Piarristeguy, G. Bruns, P. Jost, S. Grothe, R.M. Schmidt, C. Longeaud, M. Wuttig, Stoichiometry dependence of resistance drift phenomena in amorphous GeSnTe phase-change alloys, J. Appl. Phys. 113, 23704 (2013)

- ♦ T. Kubart, R.M. Schmidt, M. Austgen, T. Nyberg, A. Pflug, M. Siemers, M. Wuttig, S. Berg, Modelling of sputtering yield amplification in serial reactive magnetron co-sputtering, Surface and Coatings Technology 206, 5055 (2012)
- D. Krebs, R.M. Schmidt, J. Klomfaß, J. Luckas, G. Bruns, C. Schlockermann, M. Salinga, R. Carius, M. Wuttig, *Impact of DoS changes on resistance drift and threshold switching in amorphous phase change materials*, Journal of Non-Crystalline Solids 358, 2412 (2012)

Conference presentations

- ♦ **R.M. Schmidt**, T. Kubart, A. Pflug, M. Wuttig, *Sputter yield amplification upon reactive serial co-sputtering of doped TiO*₂, DPG Frühjahrstagung (Dresden, Germany, 2014)
- P. Ries, R.M. Schmidt, A. Pflug, T. Kubart, M. Wuttig, Sputter yield amplification of carbon by serial magnetron co-sputtering, DPG Frühjahrstagung (Dresden, Germany, 2014)
- ♦ R. Sittner, **R.M. Schmidt**, M. Wuttig, *Al-doped zinc stannate thin films as amorphous transparent conductive oxides prepared by reactive DC magnetron sputtering*, DPG Frühjahrstagung (Dresden, Germany, 2014)
- S. Urbahn, R.M. Schmidt, A. Yatim, M. Wuttig, Work function measurements of sputtered TiO₂ in UHV ambience, DPG Frühjahrstagung (Dresden, Germany, 2014)
- ♦ R.M. Schmidt, M. Austgen, A. Pflug, T. Nyberg, S. Berg, M. Wuttig, Sputter yield amplification upon reactive serial co-sputtering of doped TiO₂, IVC-19 19th International Vacuum Congress (Paris, France, 2013)
- ♦ R.M. Schmidt, O. Lenck, T. Kubart, D. Wagner, A. Pflug, T. Nyberg, S. Berg, M. Wuttig, Prozess characteristics and film properties upon doping of TiO₂ by reactive serial cosputtering utilizing high power impuls magnetron sputtering, DPG Frühjahrstagung (Regensburg, Germany, 2013)
- C. Jacobi, D. Gebauer, R.M. Schmidt, C.M.M. Guntermann, C. Jodocy, C. Effertz, M. Wuttig, Interface Analysis of Thermally Evaporated Thin Noble Metal Films on PTCDI-C13, DPG Frühjahrstagung (Regensburg, Germany, 2013)
- ♦ R.M. Schmidt, T. Kubart, M. Austgen, D. Wagner, T. Nyberg, A. Pflug, S. Berg, M. Wuttig, Sputter Yield Amplification upon reactive sputtering of TiO₂, DPG Frühjahrstagung (Berlin, Germany, 2012)

- ♦ S. Urbahn, **R.M. Schmidt**, A. Yatim, M. Wuttig, *Work function measurements of sput-tered TiO*₂ *in UHV ambience*, DPG Frühjahrstagung (Berlin, Germany, 2012)
- ♦ C. Dellen, M. Wimmer, **R.M. Schmidt**, M. Salinga, M. Wuttig, *Resistance drift in amorphous phase change thin films*, DPG Frühjahrstagung (Berlin, Germany, 2012)
- ♦ R.M. Schmidt, M. Austgen, D. Wagner, T. Kubart, A. Pflug, T. Nyberg, S. Berg, M. Wuttig, Sputter Yield Amplification of reactively sputtered TiO₂, RSD – Reactive Sputter Deposition (Linköping, Sweden, 2011)
- R.M. Schmidt, G. Bruns, D. Krebs, J. Luckas, C. Schlockermann, M. Salinga, M. Wuttig, *Drift in amorphous phase change materials*, DPG Frühjahrstagung (Dresden, Germany, 2011)
- D. Krebs, R.M. Schmidt, J. Klomfaß, J. Luckas, G. Bruns, C. Schlockermann, M. Salinga, R. Carius, M. Wuttig, *Impact of DOS changes on resistance drift and threshold switching in amorphous phase change materials*, E/PCOS – European Symposium on Phase Change and Ovonic Science (Zürich, Switzerland, 2011)
- D. Krebs, R.M. Schmidt, J. Klomfaß, J. Luckas, G. Bruns, C. Schlockermann, M. Salinga, R. Carius, M. Wuttig, *Impact of DOS changes on resistance drift and threshold switching in amorphous phase change materials*, ICANS – 24th International Conference on Amorphous and Nanocrystalline Semiconductors (Nara, Japan, 2011)
- ♦ J. Luckas, A. Piarris- teguy, G. Bruns, P. Jost, S.Grothe, R.M. Schmidt, C. Longeaud, M. Wuttig, New functionalities of Ge-Sn-Te phase change alloys, ICANS 24 24th International Conference on Amorphous and Nanocrystalline Semiconductors (Nara, Japan, 2011)

Erklärung

Hiermit versichere ich, dass ich die vorliegende Arbeit selbständig verfasst und nur die angegebenen Quellen und Hilfsmittel benutzt habe.

Eine Anmeldung der Promotionsabsicht habe ich an keiner anderen Fakultät oder Hochschule beantragt.

Bremen, 22. März 2015